COO-2490-6

# A STUDY OF THE HIGHER EXCITATION STATES OF $^{12}$B VIA THE $^{11}$B(n,n)$^{11}$B REACTION

R. M. White

June 1977

*Study of Structure of Light Nuclei with Neutrons*

*Ohio University*
*Athens, Ohio*

# DISCLAIMER

# ABSTRACT

Differential cross sections for neutrons elastically scattered from an isotopically enriched sample of $^{11}B$ have been measured for nine laboratory angles from 20° to 160° at 17.5° increments for sixty incident neutron energies from 4.0 MeV to 8.0 MeV. The data have been corrected for incident neutron beam attenuation in the sample, air scattering of neutrons, and finite geometry and multiple scattering effects using a Monte Carlo code which included the energy-dependence of differential cross sections of multiple events necessary for light nuclei.

Comparison of the present data is made with data previously measured in this energy region and all known differential neutron data on $^{11}B$ have been integrated and compared with recent high resolution total cross section measurements to gain information on the neutron inelastic scattering cross section.

All the neutron elastic differential cross section measurements on $^{11}B$ have been analyzed with a new R-matrix analysis program utilizing j-j coupling with most previous assignments of $J^{\pi}$ in the compound nucleus $^{12}B$ confirmed, and new $J^{\pi}$ assignments made in the region of the present measurements. Finally, based on the results of the present measurements and analysis, recommendations for further neutron cross section measurements on $^{11}B$ are made.

# A STUDY OF THE HIGHER EXCITATION STATES OF $^{12}B$ VIA THE $^{11}B(n,n)^{11}B$ REACTION

A Dissertation Presented to
The Faculty of the Graduate College of
Ohio University

In Partial Fulfillment
of the Requirements for the Degree
Doctor of Philosophy

by
Roger M. White
June, 1977

This dissertation has been approved
for the Department of Physics
and the Graduate College by

Raymond O. Lane

Distinguished Professor of Physics

Norman S Cohen

Dean of the Graduate College

# ACKNOWLEDGEMENTS

The financial support of the United States Energy Research and Development Administration was essential for the initiation and completion of this research and is greatly appreciated. My thanks go to Mr. Don Carter and Mr. Dave Sturbois for their significant efforts in assisting with the completion of data acquisition and for their valuable expertise and that of the Physics Shop in keeping the Laboratory operational. I would like to thank Dr. Jerry Adams for his help with the general scattering theory and R-matrix analysis and Drs. Alan Smith and James Monahan of the Argonne National Laboratory for their advice on the multiple scattering and the angular momentum coupling theory. My thanks go to Dr. George Auchampaugh of the Los Alamos Scientific Laboratory for use of his total cross section measurements.

I would like to thank Dr. Harold Knox for his many hours of assistance on this project and for his patience. A very special thank you goes to Dr. John Cox for his efforts toward my education in experimental nuclear physics.

To my advisor, Dr. Ray Lane, I express my sincere appreciation for the guidance, encouragement and unending support provided to me throughout this project.

To my mother and to my wife, Linda, whose endurance and support of this long project were continuous, I give my thanks and love. Finally, in memory of my father, whose interest in this effort was surpassed by none, I dedicate this work.

# Table of Contents

# LIST OF FIGURES

# LIST OF TABLES

# CHAPTER 1

# INTRODUCTION TO THE PROBLEM

The nucleus $^{12}B$ is of interest to those who study nuclear structure strictly for the interest in fundamental physics as well as to those who are interested in nuclear measurements for applied purposes. Previous measurements (La 70, Ne 73) of neutron differential cross sections for neutrons scattered from $^{11}B$ with energies of 0.1 MeV to 4.4 MeV, corresponding to excitation energies of 3.5 MeV to 7.4 MeV in $^{12}B$, have shown more pronounced resonance structure in those cross sections than for any of the other nuclei lighter than carbon and heavier than the isotopes of helium. From such measurements important properties of states in the compound nucleus $^{12}B$ can be determined. Neutron total cross section measurements on $^{11}B$ (Fo 61, Ca 71) have indicated complex resonance structure to exist well beyond the energy region of previously measured differential cross sections. Therefore, the first objective of this experiment was to extend the neutron elastic differential cross section measurements from those previously made up to 4 MeV to the limit (with the neutron source discussed below) of our experimental capability of approximately 8 MeV (10.7 MeV excitation in $^{12}B$).

These measurements were accomplished by utilizing the Ohio University Tandem Van de Graaff Accelerator to accelerate a beam of monoenergetic protons to the energies necessary to generate 4 MeV to 8 MeV neutrons via the tritium (p,n) nuclear reaction. The neutrons so obtained were then scattered from a cylindrical sample of $^{11}B$ using a neutron detector to count the number of neutrons scattered at various angles. The pattern of scattered neutrons was then analyzed as a function of the incident neutron energy. It is from these scattering patterns that nuclear structure information can be derived.

The second objective of this experiment was to develop a practical computer program utilizing the R-matrix theory of nuclear reactions in an attempt to make definitive assignments of angular momentum and parity (as well as widths, level energies, etc.) of the various resonances expected to be observed. In the process, it was also planned to use this program to reanalyze the previously measured differential cross sections to verify both the validity of the program as well as to verify previously assigned states in the compound nucleus $^{12}B$.

While the study of nuclear structure for its own sake is interesting and rewarding, importance should be given to practical application of such work for the benefit of society who support it in the first place. The interaction of neutrons with $^{11}B$ has been given highest priority for study (Tw 76) along with several other light nuclei in terms of the national fusion energy program. Light nuclei are under study as blanket materials for reflecting and shielding neutrons around the plasma generated in a fusion reactor. With the ever-increasing shortage of the various forms of fuel necessary for energy production in this nation, the potential for fusion energy, with its fuel abundance and minimal harmful by-products, cannot and must not be ignored. The kind of measurement and the type of study considered in this experiment are vital to laying the foundation for a workable fusion reactor in the future.

Since the numbers generated from these measurements are to be used both in an engineering sense, and in accurate determination of basic nuclear parameters, it is necessary to obtain the experimental data as precisely as possible. A neutron detector-spectrometer system with associated computer support was developed for this experiment to provide neutron differential cross section measurements to an uncertainty of less than 5%. The computer support involved extensive programming to analyze the data as it was taken and provided immediate results so that an investigator could continually monitor and keep track of the complex measurements as the experiment progressed.

The following chapters will discuss in detail each aspect of the experiment, from equipment and procedures utilized to the formulation and programming of the theoretical analysis. The final objective of this paper is to present a technique of neutron physics and a method of nuclear data analysis in a clear and easily readable manner both for the experimentalist with interest in the methods of this experiment and, very importantly, for the beginning student who wishes to gain an understanding of some of the difficulties involved in experimental neutron physics.

# CHAPTER 2

# DATA ACQUISITION AND REDUCTION

## 2.1 Experimental Techniques

The philosophy of design of a neutron time-of-flight (T.O.F.) spectrometer system is governed largely by the physical space available and the financial resources of the experimenter. The nature of neutron measurements requires significant shielding of the neutron detector and a sizable amount of electronic and computing apparatus to support the system. These factors, coupled with the large amount of data to be taken on $^{11}B$ and later on, several of the other light nuclei, governed the decision to go with a single, well-shielded detector system, the calibration of which could be tightly controlled and the data so obtained easily reduced by computer techniques.

Peculiar to these light nuclei is the problem of energy loss of the elastically scattered neutrons due to the kinematics of scattering off very light nuclei. For example, a 4.00 MeV neutron incident on $^{11}B$ will have only 2.80 MeV of energy after elastically scattering 160 degrees. Therefore, a larger range of elastically scattered energies is encountered at various spectrometer angles even for a small range of incident neutron energies. If the neutron detector system is to be biased such that the lowest energy neutrons are detected with good efficiency, a well shielded detector is necessary. Further, if data are to be acquired at a reasonably rapid rate, a high current accelerator coupled to a prolific source of monoenergetic neutrons, a neutron detector of large solid angle, and a large size scattering sample are desirable. However, the large sample size then requires that accurate computer codes be written to correct for finite sample size effects. It is to these ends that the neutron T.O.F. spectrometer and data reduction system were developed for this experiment. This chapter contains a description of the entire neutron-producing and -detecting system as well as the various support facilities and results obtained.

### 2.1.1 The Ohio University Tandem Van de Graaff Accelerator

The Ohio University Tandem Van de Graaff was designed and constructed by High Voltage Engineering Corporation (HVEC). This T-11 accelerator employs the high-gradient techniques developed by HVEC for the large tandem accelerators such as the Emperors. The accelerator proper is contained in a unique T-shaped pressure vessel. The horizontal accelerator tube passes through a central terminal that is charged by a belt in a vertical column. The terminal is continuously chargeable to voltages up to approximately 4.5 million volts. Thus, the T-11 accelerator is capable of producing beams of up to 9 MeV protons and in a very short distance. These beams may also be unusually intense at high voltage gradients since the instabilities resulting from belts in conventional tandem accelerators have been minimized by moving the charging belt away from the accelerator tubes to the vertical column. The T-11 accelerator is diagrammed in Figure 2.1. In this experiment, the diode source, which will produce protons up to 80 kev of energy, was used to inject protons via an inflection magnet into the low energy end of the T-11. The proton beam was pulsed by means of a beam-chopping and klystron-bunching system at the pre-acceleration end of the accelerator. For this experiment, the accelerator routinely produced protons pulsed and bunched with a pulse width of better than 1 nsec FWHM at a repetition rate of 5 MHz and at an average current in excess of 4 μamps.

### 2.1.2 Neutron Source

One of the obvious difficulties of using high energy neutrons as a probe in nuclear structure studies is that since they do not carry a charge, they cannot be accelerated and, therefore, must be produced through a nuclear reaction. For the energy range of interest in this experiment (4 MeV to 8 MeV) the most ideal reaction is the $T(p,n)^3He$ reaction, as can be seen from Figure 2.2. This reaction provides a prolific, monoenergetic source of neutrons to well beyond 8 MeV with a gas cell pressure of 18 psi of tritium. This pressure introduces an energy spread of ±20 to ±30 keV in the neutron pulse. As the Q value for this reaction is approximately -0.764 MeV, a 5-MeV to 9-MeV proton beam from the tandem Van de Graaff accelerator incident on a cell

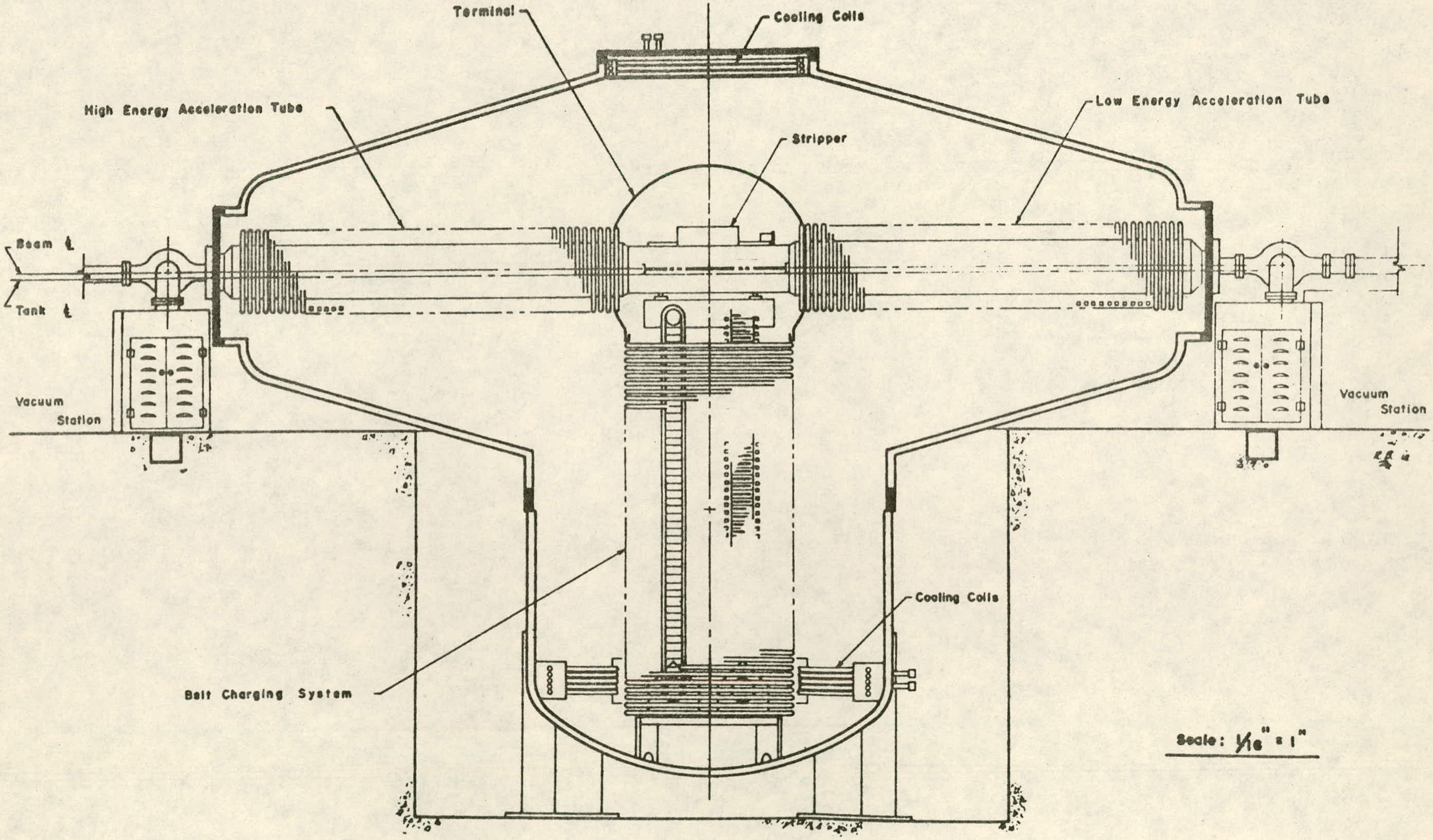

Figure 2.1 Ohio University Tandem Van de Graaff Accelerator

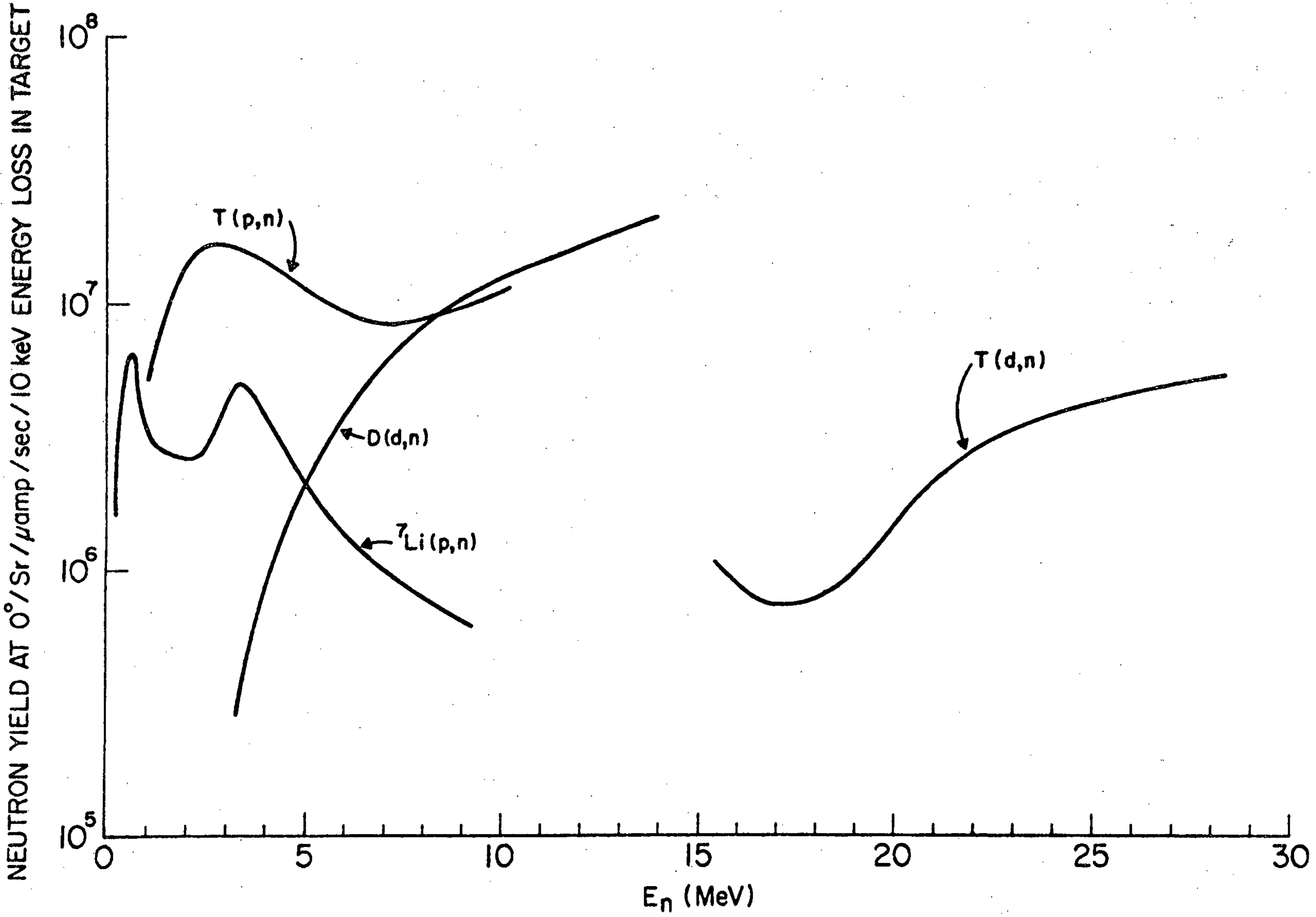

Figure 2.2 Comparison of zero-degree neutron yields for various source reactions.

filled with tritium gas will yield approximately 4-MeV to 8-MeV neutrons in the laboratory frame. Further, this neutron yield is peaked in the forward direction with the energy of neutrons in other directions decreasing rapidly with increasing angle. The tritium gas-handling system and gas cell, as shown in Figures 2.3 and 2.4 respectively, have been described elsewhere (Ca 73). The gas cell is based on a design used at Los Alamos Scientific Laboratory and perfected for these uses by J. D. Carlson (Ca 73a). The system incorporates a uranium furnace in which the tritium is stored in the form of a hydride and therefore is fully recoverable. The gas cell entrance window used was a 5 μm molybdenum foil with a 10 mil gold foil serving as a beam stop. Pressure in the cell was monitored by a Wallace and Tiernan differential pressure gauge with a sensitivity of 0.06 psi. The problems of beam heating effect, density of gas molecules, and cooling are described in Section 2.2 and Appendix 3.

### 2.1.3 Scattering Sample

The scattering sample used in this experiment was 41.213 grams of boron isotopically enriched to 97.15 (atomic) percent boron-11. Total boron content of the sample was 98.2% with the balance made up of carbon (1.23%) and oxygen (0.10%). The enriched boron-11 powder was obtained from Oak Ridge National Laboratory (ORNL) Nuclear Division and Table 2.1 gives the isotopic and spectrographic

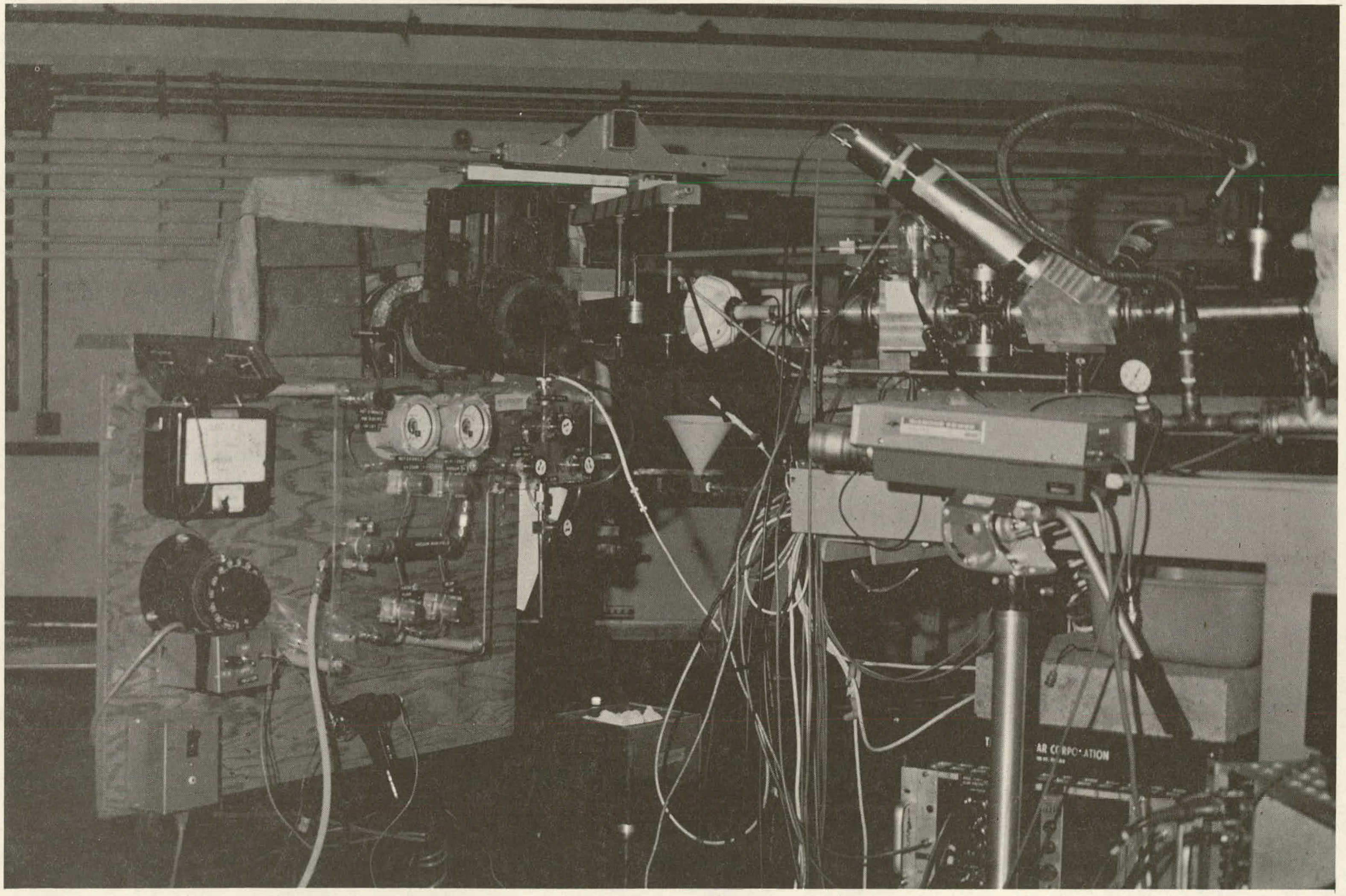

Figure 2.3 General experimental configuration including tritium gas-handling system.

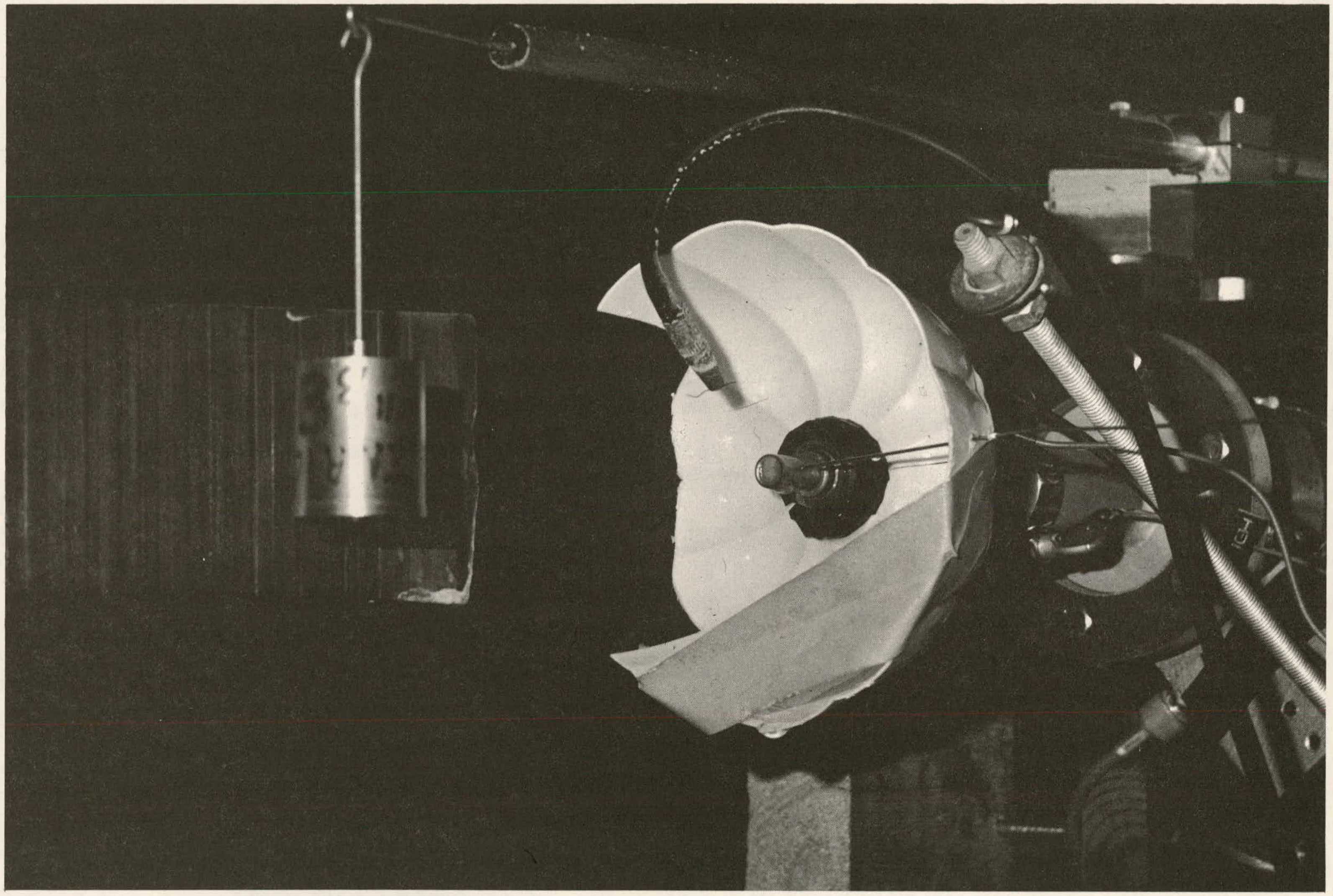

Figure 2.4 Tritium gas cell with cooling spray, scattering sample, and shadow bar.

Table 2.1

Analysis of Boron-11 Scattering Sample

Oak Ridge National Laboratory
Nuclear Division

Sample Number 4700704

Isotopic Analysis

| Isotope | Atomic Percent |
|---|---|
| 10 | 2.85 |
| 11 | 97.15 |
| Total Boron | 98.2 % |
| Carbon | 1.23% |
| Oxygen | 0.10% |
| $H_2O$ | 243 ppm |

Spectrographic Analysis

| Element | ppm | Element | ppm |
|---|---|---|---|
| Ag | < 1 | Mg | 12 |
| Al | <10 | Mn | < 1 |
| Ba | < 1 | Mo | < 1 |
| Be | < 1 | Pb | 4 |
| Ca | 50 | Si | 5000 |
| Cd | < 1 | Sn | < 1 |
| Co | <20 | Ti | 10 |
| Cr | 2 | V | < 1 |
| Cu | <10 | W | <10 |
| Fe | 20 | Zr | < 2 |

analysis made by ORNL on the sample.

The boron-11 powder was contained in a thin-walled aluminum can 4.0 cm in height by 3.3 cm in diameter which was machined to a thickness of 0.01 inch. An identical empty can served for sample-out background measurements (see Section 2.2). Both cans were sealed air tight with epoxy glue. The mass of each can empty was 7.33 grams. The scattering sample was positioned accurately by hanging it with a small diameter rod from a hook, the gas-cell-to-sample distance being approximately 20 cm on a direct line with the incident proton beam. As the cross sections of $^{10}B$ and $^{12}C$ are both similar in magnitude to that of $^{11}B$, the isotopic correction for these two elements would be a small fraction of the already small percent impurity in the enriched $^{11}B$ sample. This effect was estimated to be significantly less than 1% and, therefore, no isotopic correction was made to the experimental data.

### 2.1.4 Neutron Detector and Shield

The neutron detector used in this experiment was NE-224 liquid scintillator housed in a 5 cm thick x 18 cm diameter lucite container optically coupled to an RCA 4522 photomultiplier tube (see reference Li 75). Figure 2.5 shows a cross-sectional view of the neutron detector. As the ratio of neutrons arriving from the source (gas cell) at the detector compared to those scattered from the sample and arriving at the detector is approximately 1000 to 1, and

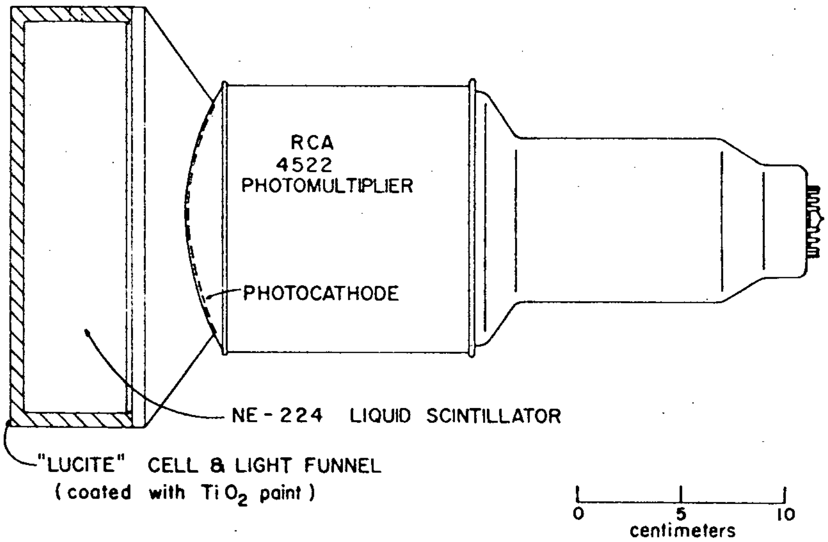

Figure 2.5

Cross sectional view of the main neutron detector (from reference Li 75).

since it is the neutrons scattered from the sample we wish to detect, it is obvious that the detector must be very well shielded in order to block out the source neutrons. The detector shield, shown in Figure 2.6, consisted of an 8-inch inner diameter by 1-inch thick steel pipe around which was a 3-inch thick lead annulus 30 inches long in the region of the scintillator and a 2-inch thick lead annulus 24 inches long extending forward along the pipe. This represents over 1000 pounds of steel and 2000 pounds of lead shielding. Placed around the lead was 1750 pounds of steel shot and outside of that 1000 pounds of paraffin (above 5 MeV the inelastic scattering of neutrons by iron allows it to compare well with hydrogen as neutron shielding material). The total weight of the system neglecting the massive copper shadow bar and support was over 7000 pounds. Use of an air pad system allowed movement of the shield by one person. The massive copper shadow bar could be repositioned accurately for different scattering angles. Nine angles (laboratory system) were measured from 20 degrees to 160 degrees at 17.5 degree increments. A typical neutron flight path from sample to detector was 3.6 meters. A monitor, which consisted of an NE-102 plastic scintillator 1/2-inch thick by 1-inch in diameter coupled to an RCA 8575 photomultiplier tube, was employed to monitor the source neutron flux (see Sections 2.2 and 2.3). No shielding (other than magnetic) was employed on the monitor because the direct neutron count was so high compared to the gamma

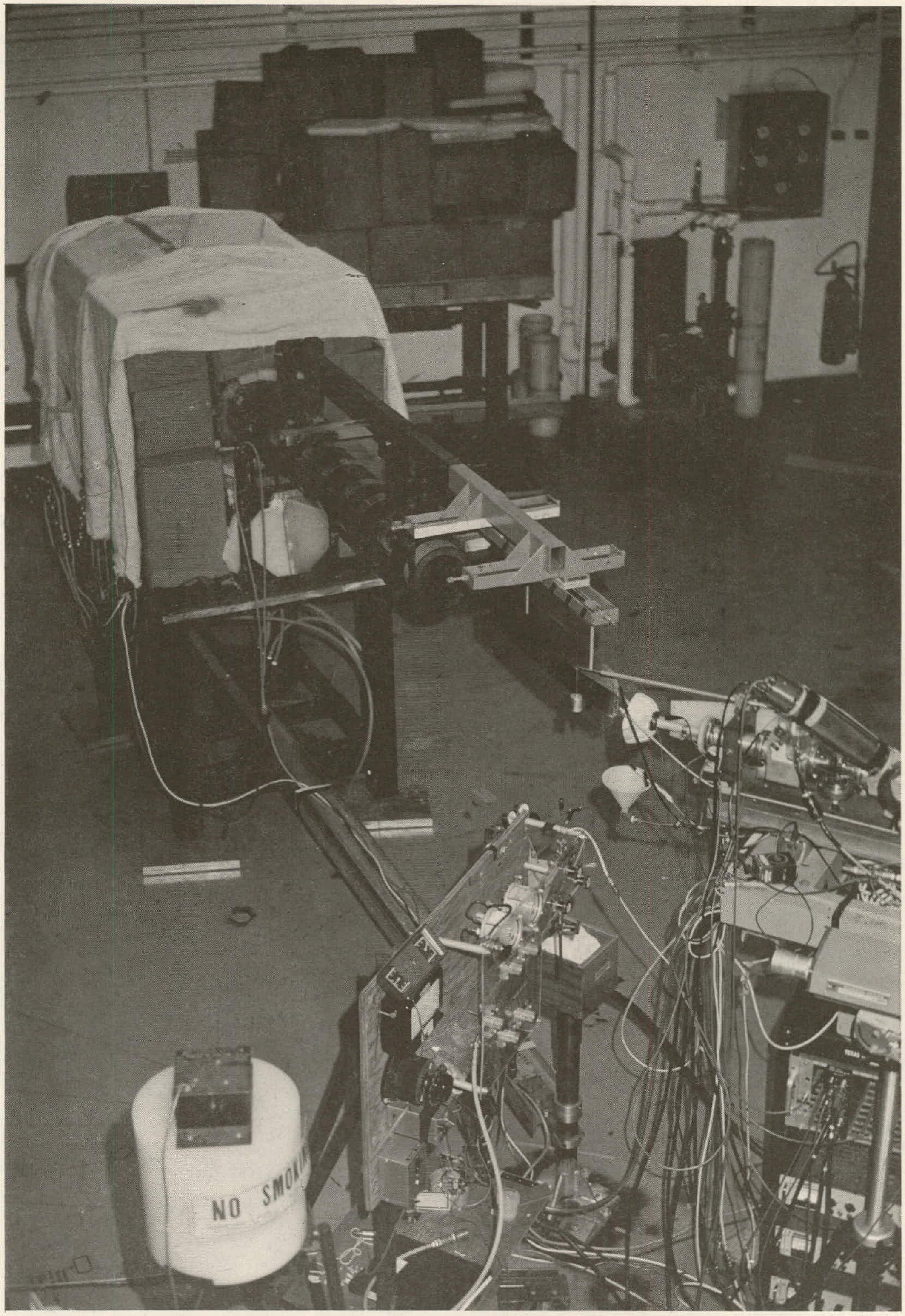

Figure 2.6 General experimental configuration including main neutron detector shield and shadow bar.

rays and general neutron background.

## 2.2 Scheme for Data Reduction

The standard use of a liquid scintillator-photomultiplier tube combination to detect neutrons has various difficulties associated with it. Two of the most important are: 1) the combination does not, except in the very crudest sense, discriminate with respect to the energy of the neutrons--it simply counts them, and 2) the efficiency with which it counts them is energy dependent. Time-of-flight techniques, with associated electronic circuitry described in Section 2.3, help to solve the first problem. The problem of efficiency variation with energy, the associated problem of absolute calibration of the neutron detection system, and the technique of transforming neutron counts to differential cross section are the subject of this section.

The final question in almost any nuclear data measurement is how accurately the data taken represents the real system one has set out to measure, and perhaps, this question is the most difficult of all to answer. It becomes a question of how accurately the neutron detector can be calibrated and thereby how accurately one can transform measured neutron counts to absolute mb/sr, the units of differential cross section. The answer to this for the present experiment lies in the fundamental definition of differential cross section, i.e., the ratio of neutrons scattered from a sample in units of neutrons/sr to the neutrons incident upon the sample in neutrons/mb. Ideally, one would count the neutrons scattered at a certain angle and then place the detector at zero degrees with the sample out and count the neutrons for the same length of time and take the ratio of the two counts. In this experiment, a problem with this procedure is that in scattering neutrons off a light nucleus the resultant neutron energy at a large angle of scattering is several MeV less than the incident neutron energy and the efficiency with which the detector detects neutrons is certainly energy dependent.

Therefore, a slightly different approach is taken. A monitor is placed at an appropriate angle (discussed later) with respect to the zero-degree neutron flux and, with the main neutron detector at zero degrees, measurements are taken with no scattering sample over the entire energy range of neutrons to be detected for a given incident neutron energy range. This establishes the energy dependence between the detector and monitor so that during the data acquisition when the detector has been moved to a particular scattering angle one effectively knows, through the monitor, what the detector would measure at zero degrees.

The neutron yield from the tritium (p,n) source reaction, as Figure 2.2 shows, is energy dependent. However, since the monitor angle is not changed during the course of the experiment, it will be shown in the mathematical analysis to follow that one need only be concerned with the change in the zero-degree yield of the neutron source reaction and furthermore, that only the <u>relative shape</u> of the energy dependence of the zero-degree yield need be considered. Appendix 4 will establish how accurately the shape of the zero-degree yield of the tritium (p,n) reaction is known.

For the actual measurement of angular distributions, we consider the experimental geometry as shown in Figure 2.7 where:

RSS = source to sample distance
RDS = sample to detector distance
RMD = source to monitor distance
EP = average proton energy at gas cell center
EN0 = zero degree neutron energy
ENS = scattered neutron energy (at detector)
ENM = neutron energy at monitor

We consider first the neutron flux scattered by a single scattering nucleus upon which is incident a plane wave of neutrons of intensity I(EN0).

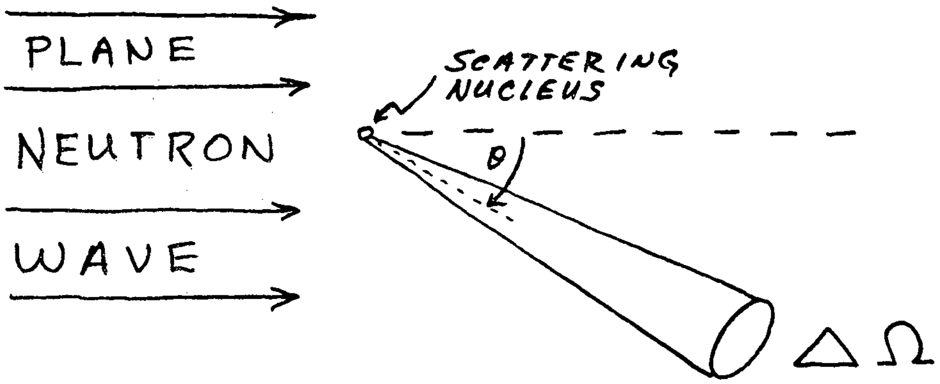

The neutron flux scattered from the single nucleus is given by:

$$\phi_{SCATT}(\theta, ENS) = I(ENO) \times \sigma(\theta, ENO) \qquad (2\text{-}1)$$

# EXPERIMENTAL GEOMETRY FOR DATA ACQUISITION

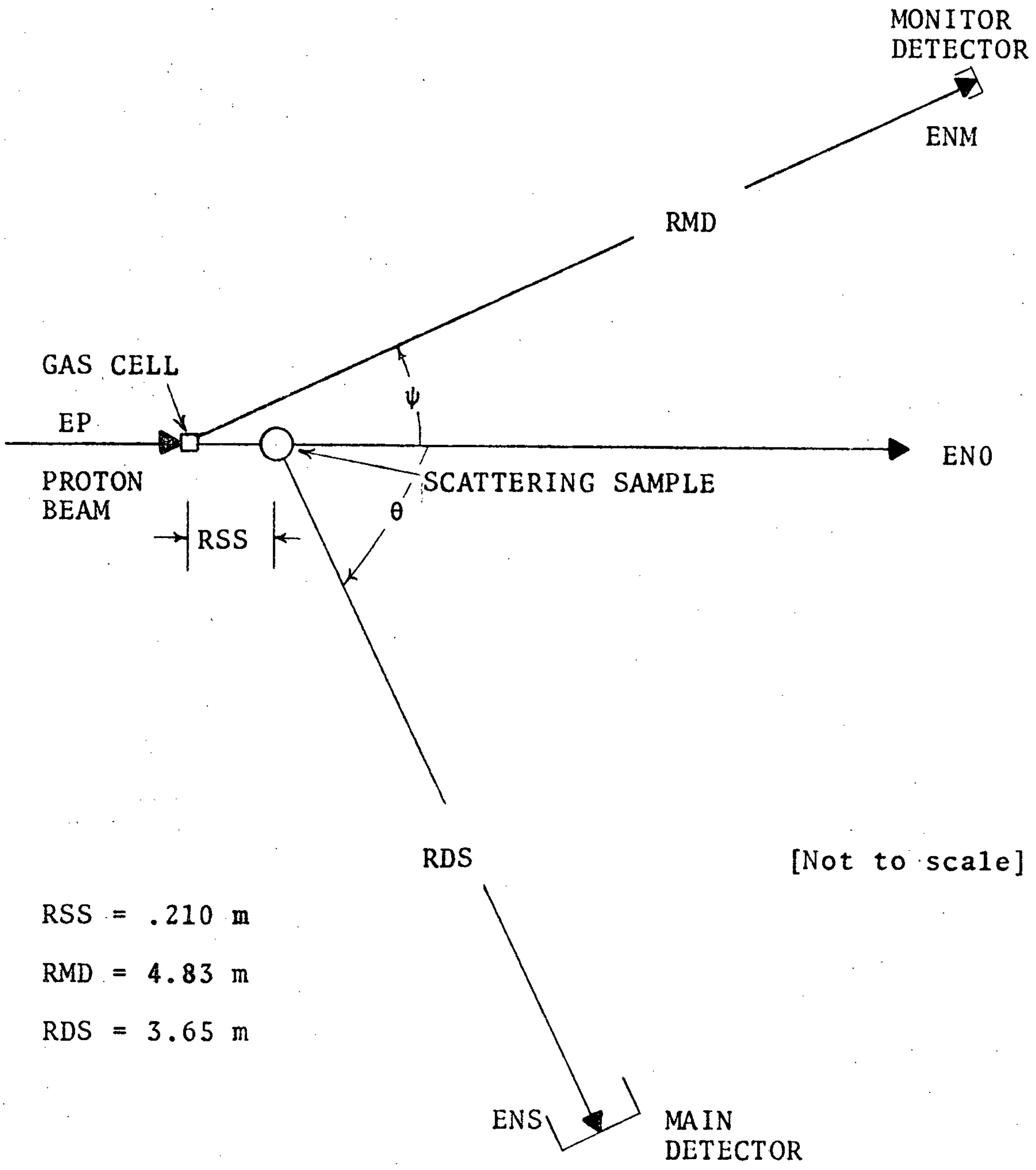

[Not to scale]

RSS = .210 m

RMD = 4.83 m

RDS = 3.65 m

Figure 2.7

where: $\varphi_{SCATT}(\theta, ENS)$ = neutrons/sr/nucleus (/sec)

$I(ENO)$ = neutrons/cm$^2$ (/sec)

$\sigma(\theta, ENO)$ = cm$^2$/sr/nucleus

The flux scattered by N nuclei is then given by:

$$\Phi_{SCATT}(\theta, ENS) = N \times \varphi_{SCATT}(\theta, ENS)$$
$$= N \times I(ENO) \times \sigma(\theta, ENO) \quad (2\text{-}2)$$

At this point, a number of finite geometry effects due to the finite size of the scattering sample containing the N nuclei and for which corrections must be made (or shown to be insignificant) are considered in Section 2.4 and in Appendix 1.

The incident intensity, I(ENO), can be written as:

$$I(ENO) = N(ENO) / A_{SAM}$$

where:

$N(ENO)$ = neutrons (/sec) incident upon the sample

$A_{SAM}$ = area of the sample

Then we can write from Eq. (2-2):

$$\sigma(\theta, ENO) = \frac{\Phi_{SCATT}(\theta, ENS) \times A_{SAM}}{N \times N(ENO)} \quad (2\text{-}3)$$

If we now consider the number of neutrons counted at the detector we can write the following:

$$N^{CTO}_{DET}(\theta, ENS) = \Phi_{SCATT}(\theta, ENS) \times \underset{DATA}{\Delta\Omega_{DET}} \times \underset{DET}{Eff}(ENS)$$

(2-4)

where $\Delta\Omega_{\substack{\text{DET} \\ \text{DATA}}}$ = solid angle subtended by the detector with respect to the sample (during data taking) and $\underset{\text{DET}}{\mathcal{E}ff}(\text{ENS})$ = efficiency of the detector at the neutron energy ENS. If we solve Eq. (2-4) for $\Phi_{\text{SCATT}}(\theta,\text{ENS})$ and substitute that value into Eq. (2-3) we obtain:

$$\sigma(\theta,\text{ENO}) = \frac{N_{\text{DET}}^{\text{CTD}}(\theta,\text{ENS}) \times A_{\text{SAM}}}{N \times N(\text{ENO}) \times \Delta\Omega_{\substack{\text{DET} \\ \text{DATA}}} \times \underset{\text{DET}}{\mathcal{E}ff}(\text{ENS})} \qquad (2\text{-}5)$$

The problem now is to determine the number of neutrons incident upon the sample, i.e., N(ENO). This is given by the expression:

$$N(\text{ENO}) = \phi_n(0^\circ,\text{ENO}) \times \Delta\Omega_{\text{SAM}} \qquad (2\text{-}6)$$

where $\phi_n(0^\circ,\text{ENO})$ = neutrons/sr at zero degrees from the $T(p,n)^3He$ reaction and $\Delta\Omega_{\text{SAM}}$ = solid angle subtended by the sample at the source. From the definition of the differential cross section we know that the following ratio holds:

$$\frac{\phi_n(0^\circ,\text{ENO})}{\phi_n(\psi,\text{ENM})} = \frac{\sigma_{T(p,n)}(0^\circ,\text{EP})}{\sigma_{T(p,n)}(\psi,\text{EP})} \qquad \underline{\text{OR}}$$

$$\phi_n(0^\circ,\text{ENO}) = \phi_n(\psi,\text{ENM}) \frac{\sigma_{T(p,n)}(0^\circ,\text{EP})}{\sigma_{T(p,n)}(\psi,\text{EP})} \qquad (2\text{-}7)$$

$\phi_n(0^\circ,\text{ENO})$ is the zero degree flux from the neutron source, $\sigma_{T(p,n)}(0^\circ, EP)$ is the zero degree $T(p,n)^3He$ reaction cross section, and $\phi_n(\psi, ENM)$ and $\sigma_{T(p,n)}(\psi, EP)$ are similarly defined for the monitor at angle $\psi$. The number of neutrons counted by the monitor is:

$$N^{CTD}_{MON}(\psi, ENM) = \phi_n(\psi, ENM) \times \underset{DATA}{\Delta\Omega}_{MON} \times \underset{MON}{Eff}(ENM) \qquad (2-8)$$

Solving for $\phi_n(\psi, ENM)$ in Eq. (2-8) and substituting this value in Eq. (2-7) yields:

$$\phi_n(0^\circ, ENO) = \frac{N^{CTD}_{MON}(\psi, ENM)}{\underset{DATA}{\Delta\Omega}_{MON} \times \underset{MON}{Eff}(ENM)} \times \frac{\sigma_{T(p,n)}(0^\circ, EP)}{\sigma_{T(p,n)}(\psi, EP)} \qquad (2-9)$$

Substitution of Eq. (2-9) into the expression for N(ENO), Eq. (2-6), gives:

$$N(ENO) = \frac{N^{CTD}_{MON}(\psi, ENM) \times \sigma_{T(p,n)}(0^\circ, EP) \times \Delta\Omega_{SAM}}{\underset{DATA}{\Delta\Omega}_{MON} \times \underset{MON}{Eff}(ENM) \times \sigma_{T(p,n)}(\psi, EP)} \qquad (2-10)$$

We utilize this expression for N(ENO) in the expression for $\sigma(\theta, ENO)$, Eq. (2-5), to give:

$$\sigma(\theta, ENO) = \qquad (2-11)$$

$$\frac{A_{SAM}\, \underset{DATA}{\Delta\Omega}_{MON}}{N\, \underset{DATA}{\Delta\Omega}_{DET}\, \Delta\Omega_{SAM}} \times \frac{N^{CTD}_{DET}(\theta, ENS)}{N^{CTD}_{MON}(\psi, ENM)} \times \frac{\sigma_{T(p,n)}(\psi, EP)}{\sigma_{T(p,n)}(0^\circ, EP)} \times \frac{\underset{MON}{Eff}(ENM)}{\underset{DET}{Eff}(ENS)}$$

Eq. (2-11) represents an expression for the cross section in terms of various solid angles, actual detector and monitor counts, the tritium (p,n) cross sections, and the efficiencies of the detector and monitor.

We now proceed to determine the ratio of efficiencies, i.e., $\underset{MON}{Eff}(ENM)/\underset{DET}{Eff}(ENS)$. Let us consider the experimental geometry for the efficiency measurements as shown in Figure 2.8 where:

RMR = source to monitor distance
RDZ = source to detector distance
ENM = energy of neutrons at monitor
EN0 = energy of neutrons at detector.

In this orientation, the number of neutrons counted at the detector is:

$$Y^{CTD}_{DET}(EN0) = Y(n\,pos)\; n_S\; \sigma_{T(p,n)}(0^\circ, EP)\; \underset{Eff}{\Delta\Omega}_{DET}\; \underset{DET}{Eff}(EN0) \tag{2-12}$$

Similarly, the number of neutrons counted at the monitor is given by:

$$Y^{CTD}_{MON}(ENM) = Y(n\,pos)\; n_S\; \sigma_{T(p,n)}(\Psi, EP)\; \underset{Eff}{\Delta\Omega}_{MON}\; \underset{MON}{Eff}(ENM) \tag{2-13}$$

where:

$Y(n\,pos)$ = number of protons on source

$n_S$ = number of tritium nuclei/cm$^2$, along the beam direction

$\underset{Eff}{\Delta\Omega}_{DET}$ = solid angle subtended by the detector at source

## EXPERIMENTAL GEOMETRY FOR RELATIVE EFFICIENCY MEASUREMENT

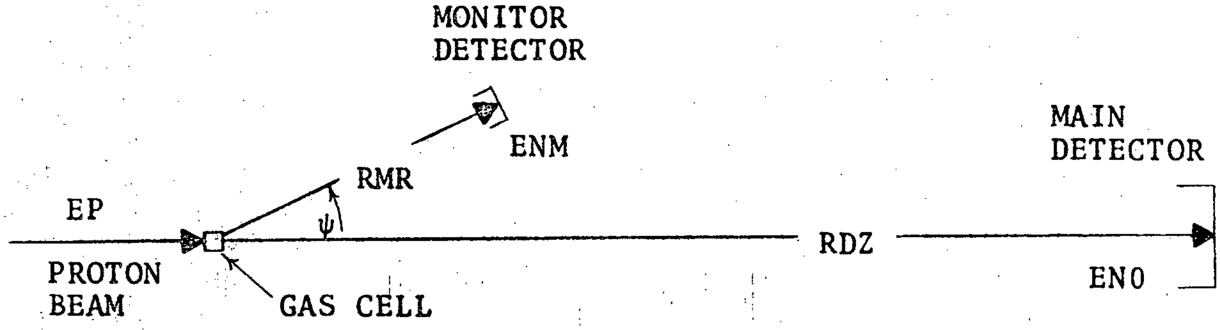

RMR = 1.61 m

RDZ = 7.66 m

[Not to scale]

Figure 2.8

$\underset{Eff}{\Delta\Omega}_{MON}$ = solid angle subtended by monitor at source.
However, for the ratio of efficiencies in Eq. (2-11) we need $Y^{CTD}_{DeT}(ENS)$, i.e.,

$$Y^{CTD}_{DeT}(ENS) = Y(np'os)\, n'_s\, \sigma_{T(p,n)}(0^\circ, EP')\, \underset{Eff}{\Delta\Omega}_{DeT}\, \underset{DeT}{Eff}(ENS) \qquad (2\text{-}12a)$$

where:

$Y(np'os)$ = number of protons on source at energy EP'

$n'_s$ = number of tritium nuclei/cm$^2$ at proton energy EP'.

Using Eq. (2-12a) and (2-13) to get the ratio $\underset{MON}{Eff}(ENM)/\underset{DeT}{Eff}(ENS)$ we obtain:

$$\underset{MON}{Eff}(ENM)/\underset{DeT}{Eff}(ENS) =$$

$$\frac{Y^{CTD}_{MON}(ENM)\, Y(np'os)\, n'_s\, \sigma_{T(p,n)}(0^\circ, EP')\, \underset{Eff}{\Delta\Omega}_{DeT}}{Y^{CTD}_{DeT}(ENS)\, Y(npos)\, n_s\, \sigma_{T(p,n)}(\psi, EP)\, \underset{Eff}{\Delta\Omega}_{MON}} \qquad (2\text{-}14)$$

To get ENS at zero degrees requires a different EP (proton energy) than to get ENS at angle θ due to the pronounced kinematic shift in energy of the scattered neutron (due to the scattering of neutrons from a 'light' nucleus). If, during the efficiency run, we can do accurate charge normalization, then Y(npos) = Y(np'os) and these two quantities divide out in Eq. (2-14). Further, it has been shown (see Appendix 3) that if the pressure of the gas cell can be held constant during beam-in conditions, the number of tritium nuclei will remain constant in the gas cell and $\eta_s = \eta_s'$. Then these quantities also divide out and Eq. (2-14) can be written:

$$\frac{\underset{MON}{\mathcal{E}ff}(ENM)}{\underset{DET}{\mathcal{E}ff}(ENS)} = \frac{Y^{CTD}_{MON}(ENM)}{Y^{CTD}_{DET}(ENS)} \times \frac{\sigma_{T(p,n)}(0^\circ, EP')}{\sigma_{T(p,n)}(\psi, EP)} \times \frac{\underset{Eff}{\Delta\Omega}_{DET}}{\underset{Eff}{\Delta\Omega}_{MON}} \tag{2-15}$$

It is shown in Appendices 2 and 3 that these two conditions are in fact well satisfied. Now, if we substitute this expression for the ratio of efficiencies into Eq. (2-11), the expression for the differential cross section becomes:

$$\sigma(\theta, END) = \frac{A_{SAM}\,\underset{DATA}{\Delta\Omega}_{MON}\,\underset{Eff}{\Delta\Omega}_{DET}}{N\,\underset{DATA}{\Delta\Omega}_{DET}\,\underset{Eff}{\Delta\Omega}_{MON}\,\Delta\Omega_{SAM}} \times \frac{N^{CTD}_{DET}(\theta, ENS)}{N^{CTD}_{MON}(\psi, ENM)}$$

$$\times \frac{\sigma_{T(p,n)}(\psi, EP)}{\sigma_{T(p,n)}(0^\circ, EP)} \times \frac{Y^{CTD}_{MON}(ENM)}{Y^{CTD}_{DET}(ENS)} \times \frac{\sigma_{T(p,n)}(0^\circ EP')}{\sigma_{T(p,n)}(\psi, EP)} . \tag{2-16}$$

We see that $\sigma_{T(p,n)}(\psi, EP)$ divides out of Eq. (2-16) because the monitor was not moved from angle $\psi$ during either the efficiency or the data run. Further, since the solid angle is by definition the area (of the face of a detector or monitor) divided by the square of the distance, i.e., $\Delta\Omega = \frac{AREA}{r^2}$ and the ratio $\underset{DATA}{\Delta\Omega}_{MON} / \underset{Eff}{\Delta\Omega}_{MON}$ becomes:

$$\underset{DATA}{\Delta\Omega}_{MON} / \underset{Eff}{\Delta\Omega}_{MON} = RMR^2 / RMD^2$$

and

$$\Delta\Omega_{\substack{DET\\ Eff}} / \Delta\Omega_{\substack{DET\\ DATA}} = RDS^2/RDZ^2$$

Also:

$$A_{SAM}/\Delta\Omega_{SAM} = RSS^2$$

Making these substitutions into Eq. (2-16) yields:

$$\sigma(\theta, ENO) = \frac{RSS^2 \cdot RMR^2 \cdot RDS^2}{N \cdot RMD^2 \cdot RDZ^2} \times \frac{N_{DET}^{CTD}(\theta, ENS)}{N_{MON}^{CTD}(\psi, ENM)}$$

$$\times \frac{Y_{MON}^{CTD}(ENM)}{Y_{DET}^{CTD}(ENS)} \times \frac{\sigma_{T(p,n)}(0^\circ, EP')}{\sigma_{T(p,n)}(0^\circ, EP)} \qquad (2\text{-}17)$$

where EP' is the proton energy necessary to give neutron energy ENS at zero degrees when EP is the proton energy which gives neutron energy ENS at scattering angle θ.

Because there exists considerable background in a neutron scattering experiment, it becomes advantageous to run for a set period of time with the sample in and for an equal period of time with the sample out. Then a subtraction of the two spectra obtained (sample-in minus sample-out) should yield results which involve just the neutrons actually scattered from the boron sample. To make sure that the sample-in run is equivalent to the sample-out run a normalization to monitor counts is effected. Then the true counts measured at the detector are given by:

$$N^{CTD}_{\substack{Det\\ TRUE}}(\theta,ENS) = \underset{S.I.}{N^{CTD}_{Det}(\theta,ENS)} - \frac{N^{CTD}_{MON}(\psi,ENM)}{N^{CTD}_{MON}(S.O.)}\, N^{CTD}_{Det}(S.O.) \tag{2-18}$$

where S.I. = sample-in run and S.O. = sample-out run. Replacing $N^{CTD}_{Det}(\theta,ENS)$ in Eq. (2-15) by the $N^{CTD}_{\substack{Det\\ TRUE}}(\theta,ENS)$ of Eq. (2-18) yields:

$$\sigma(\theta,ENO) = \frac{RSS^2 \cdot RMR^2 \cdot RDS^2}{N \cdot RMD^2 \cdot RDZ^2} \times \left\{ \frac{N^{CTD}_{Det}(\theta,ENS)}{N^{CTD}_{MON}(\psi,ENM)} - \frac{N^{CTD}_{Det}(S.O.)}{N^{CTD}_{MON}(S.O.)} \right\} \times \frac{Y^{CTD}_{MON}(ENM)}{Y^{CTD}_{Det}(ENS)} \times \frac{\sigma_{T(p,n)}(0^\circ,EP')}{\sigma_{T(p,n)}(0^\circ,EP)} \tag{2-19}$$

Eq. (2-19) represents the final expression for the absolute differential cross section in terms of: (a) the various distances of monitor and detector, (b) counts measured in monitor and detector for sample in and sample out, (c) the yields of the monitor and detector taken during the efficiency run and finally, (d) the ratio of the zero degree cross section for the tritium (p,n) neutron source reaction.

In the interest of clarity, it is well to point out here, particularly for the casual reader, the salient points of the here-to-fore described technique. (1) This method of reduction of neutron counts to absolute differential cross section is derived, basically, from the definition of differential cross section and thereby yields an absolute result without normalization to hydrogen (n,p) scattering or any other calculated or measured result. (2) This method does not depend upon normalization to the $T(p,n)^3He$ cross section. It does depend, because of the energy dependence of the tritium (p,n) zero-degree yield upon the shape of that yield which is quite another matter and is discussed fully in Appendix 4. (3) This technique demands accurate charge normalization only during the relative efficiency measurement (see Appendix 2). (4) This technique requires that the gas cell pressure remain constant only during the relative efficiency measurement (see Appendix 3). An estimation of the errors in this system of reduction of counts to absolute differential cross section is given in Section 2.5 and the determined accuracy of this method is given in Section 2.6.

### 2.3 Electronic and Computer Systems

The Ohio University Accelerator Laboratory is well supplied with state-of-the-art electronics to satisfy almost any nuclear data measurement need. In addition to standard commercial- and laboratory-built modules, a very accurate beam-current integrator has been designed and constructed by the Laboratory's electronic technicians and, as discussed in Section 2.2, was employed to obtain very accurate charge normalization (Appendix 2) during relative efficiency measurements.

An in-house IBM 1800 computer with two tape drives, two CRT's, two disk drives, three typewriters, one card reader, one high-speed line printer, and one Calcomp plotter is interfaced with a Nuclear Data 3300 multichannel analyzer for storage and analysis of data. On a time-sharing basis, the 1800 is further available for background processing and was used extensively in reducing the data of the present experiment.

### 2.3.1 Time-of-Flight Electronics

Standard time-of-flight (T.O.F.) techniques were employed in this experiment with pulse shape discrimination utilized on the main detector signal to differentiate between neutrons and gamma rays. Figure 2.9 shows in block diagram form the essential features of the system used.

The neutron detector (DET) was coupled to an Ortec 269 photomultiplier tube base (PRE) which provided a mechanical assembly and resistive voltage divider network, with appropriate capacity decoupling, for operation of the RCA 4522 photomultiplier tube. The 269 provides two outputs; the negative anode signal for timing applications and the linear signal from the ninth dynode. The anode pulse was clipped (CLIP) and sent to an EG&G T140/N zero-crossing discriminator (Z-X). The fast logic output of the T140/N was then routed to the start-pulse input of an Ortec 437A time-to-amplitude converter (TAC).

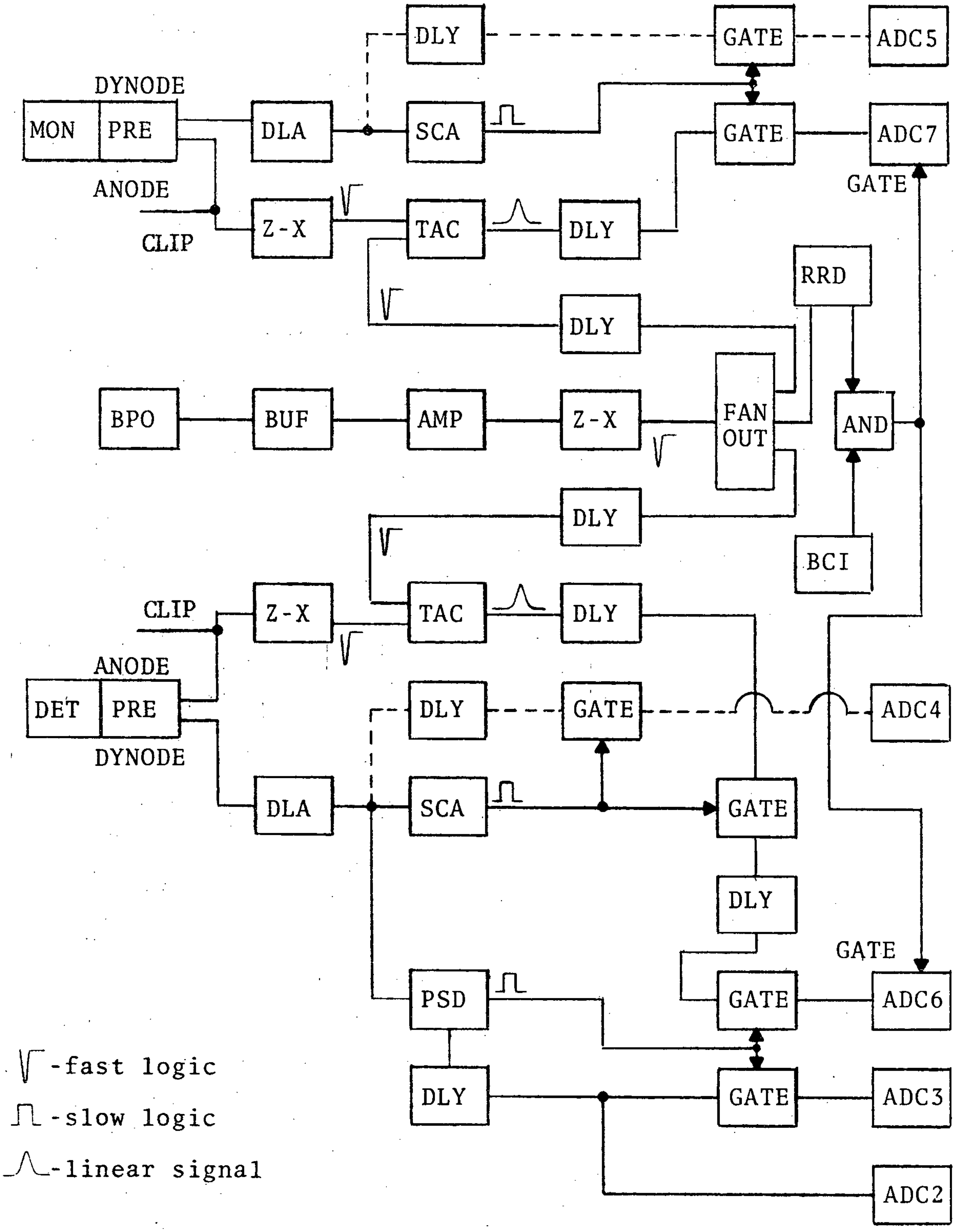

Time-of-Flight Electronics

Figure 2.9

System stop pulses were generated via a capacitive beam pick-off (BPO) suspended in the proton beam. The output lead of the BPO was coupled directly to a buffer (BUF) which reduced feed-line capacitance and served as a cable driver to an Ortec 454 fast timing amplifier (AMP). These amplified pulses were then routed to the T140/N discriminator (Z-X) and the fast logic output sent to a fast coincident unit (LRS-162) which regenerated the pulses and supplied multiple outputs (FANOUT) to be used for system stop pulses. These stop pulses were suitably delayed in RG 213 cable and routed to the stop-pulse input of the detector TAC. This procedure results in time being stored in inverted mode but since the neutron counting rate is much less than the beam pulse repetition rate this procedure greatly aids in reducing TAC dead time. For the present experiment the detector and monitor TAC dead times were monitored and always maintained at less than one percent. The detector TAC pulses (T.O.F. signal) were then subjected to several gating requirements as described below.

The detector dynode signal from the Ortec 269 photomultiplier tube base (PRE) was sent to an Ortec 460 delay line amplifier (DLA) where the signal was shaped in an appropriate manner and routed to both an Ortec 420 single channel analyzer (SCA) and an Ortec 458 pulse shape analyzer /discriminator (PSD). The detector bias was set with the Ortec 420 (see Section 2.6) in integral mode such that a logic pulse was generated only for dynode pulses that exceeded a certain voltage level and the TAC (T.O.F.) signals were first gated by these logic pulses. The second gating requirement came from the Ortec 458 (PSD) "window" output which was set on the neutron peak of the neutron-gamma spectrum of the PSD. Therefore, the requirements for the detector T.O.F. signals to be routed to an analog-to-digital-converter (ADC6) were (1) that the signals be greater than a minimum threshold (bias) setting and (2) that the pulses be identified as neutrons by the PSD.

The monitor time-of-flight system, as seen in Figure 2.9, was similar to that of the detector except that since the monitor observed the source neutrons directly and the count rate of direct neutrons was so high relative to the gamma rays, no pulse shape discrimination was employed on the monitor system. Final routing of monitor T.O.F. signals was to ADC 7.

As a further check on the neutron-gamma discrimination by the Ortec 458, the neutron-gamma spectrum from the 458 was continuously displayed in ADC 2 and the neutron gated spectrum was similarly displayed in ADC 3. This allowed continuous monitoring of the neutron-gamma discrimination, particularly for any drift of the 458 "window" set on the neutron peak. As can be noted in Figure 2.9, the actual time-of-flight spectra from the detector and monitor had to meet two further requirements before being accepted by ADC's 6 and 7. A repetition-rate-discriminator (RRD) monitored the proton beam's 5 MHz repetition rate (to within 0.10%)

and a beam-current-integrator (BCI) run in differential mode set limitations on beam current fluctuation. These requirements were set simply to allow data acquisition only when the accelerator was operating in a stable, finely-tuned condition. If both these requirements were met, a final logic signal was supplied to ADC's 6 and 7 and detector and monitor T.O.F. signals were supplied to a Nuclear Data 3300 multichannel analyzer. The signals routed via the dashed lines in Figure 2.9 are explained in Section 2.6.

### 2.3.2 Computer On-line/Off-line Analysis

The use of a reasonably simple method for reduction of counts to absolute cross section lends itself nicely to a fully computerized data reduction system. The on-line analysis program created for this experiment provided the investigator with final absolute differential cross sections in units of mb/sr (with the one exception of multiple scattering corrections discussed in Section 2.4) immediately upon completion of a sample-out background run at a given energy and scattering angle.

As discussed in Section 2.3, the neutron T.O.F. spectra for both detector and monitor were accumulated in a multichannel analyzer and then transferred to disk on the Laboratory's IBM 1800 computer. A panel of switches in the accelerator control room allowed input to the computer the following experimental parameters: the accelerator NMR frequency used to determine accurately the energy of the proton beam, the tritium gas cell pressure as measured by the Wallace and Tiernan differential pressure gauge and monitored in the control room by television, the sample-in sample-out run length in millicoulombs of charge as integrated by the beam current integrator, the scattering angle, and the scattering sample being analyzed. The on-line data reduction program then calculates from the NMR frequency the energy of the proton beam, the energy loss in the 5 μm molybdenum foil entrance window of the tritum gas cell, the average proton energy at the center of the gas cell, and the average energy of the outgoing zero degree and 25 degree neutrons from the tritium (p,n) neutron source reaction. The monitor, discussed in Sections 2.2 and 2.3, was placed at 25 degrees with respect to the incident proton beam because the T(p,n)$^3$He differential cross section does not vary rapidly at this angle for the energies of interest in this experiment and further, because there existed no interference of neutrons scattered off the shadow bar of the main neutron detector at this angle. From the kinematics of scattering off the boron-11 sample the computer also calculates the neutron energy at the detector. Recalling Eq. (2-19):

$$\sigma(\theta,\mathrm{END}) = \mathrm{CON} \times \left\{ \frac{N^{CTD}_{DET}(\theta,\mathrm{ENS})}{N^{CTD}_{MON}(\psi,\mathrm{ENM})} - \frac{N^{CTD}_{DET}(S.O.)}{N^{CTD}_{MON}(S.O.)} \right\} \times \frac{Y^{CTD}_{MON}(\mathrm{ENM})}{Y^{CTD}_{DET}(\mathrm{ENS})} \times \frac{\sigma_{T(p,n)}(0^\circ,\mathrm{EP}')}{\sigma_{T(p,n)}(0^\circ,\mathrm{EP})}$$

WHERE:

$$\mathrm{CON} = \frac{\mathrm{RSS}^2 \cdot \mathrm{RMR}^2 \cdot \mathrm{RDS}^2}{N \cdot \mathrm{RMD}^2 \cdot \mathrm{RDZ}^2}$$

we see that all the quantities in CON are easily measured to good accuracy as they are simply the distances illustrated in Figures 2.7 and 2.8, where N is the number of nuclei in the scattering sample. These numbers are fed into the data reduction program initially. The problem of evaluating the counts inside the parenthesis of Eq. (2-19) is a bit more subtle. Basically each of the four T.O.F. spectra (from which the integrated counts in the parenthesis of Eq. (2-19) are obtained) are corrected for ADC dead-time and the indicated subtraction of the spectra is performed. The computer then integrates the subtracted spectrum by fitting each side of the peak from the 40 percent point (for 20 channels or less) until a minimum is obtained. An average background around that minimum is obtained and a least-squares fit performed to the function exp(ax + b). This function is used to find three percent of the total peak height and the cursor for integration limit is set to the channel closest to this point. This procedure is carried out for both sides of the peak and then an integration between the cursors is performed to give the total counts in the T.O.F. peak. This procedure is superior to a Gaussian fit of the total peak, particularly if for some reason the T.O.F. peak is slightly asymmetric, and it further gives a highly consistent way of setting integration limits. Just how consistent is this procedure is one of the subjects of Section 2.6.

The ratio of detector and monitor efficiencies which reduces to the ratio of yields as explained in Section 2.2, is obtained from an energy-count mesh for both monitor and detector already stored in the on-line program. This mesh was obtained prior to the actual data taking by using the geometry shown in Figure 2.8. With the monitor at 25 degrees with respect to the incident proton beam and the detector-shield at zero degrees, short runs are made at approximately 50 to 100 keV intervals over the entire energy range of neutrons to be measured by both monitor and detector. These runs are usually shorter than two minutes and are repeated several (3-5) times for each energy. The results of these measurements are stored for use by the on-line data reduction program. Further explanation of this procedure is found in Appendix 2.

Finally, the ratios of the zero degree cross sections for the $T(p,n)^3He$ neutron source reaction are obtained from a fine energy-cross section mesh like that of the efficiencies. The sources for this data and other details are discussed in Appendix 4. The on-line program then outputs the laboratory and center of mass angles and cross sections as well as other log information on the control room typewriter. Furthermore, a CRT displays all spectrum analysis that the computer performs on a given energy-angle measurement for visual inspection by the investigator. All information obtained by the on-line analysis program is transferred to magnetic tape should further off-line analysis be desired. A very similar version of the on-line program was written so that the original data (T.O.F.

spectra) could be reanalyzed at any time.

## 2.4 Data Corrections

The differential cross section is defined as

$$\sigma(\theta, ENO) = \frac{\varphi_{SCATT}(\theta, ENS)}{I(ENO)}$$

where the various quantities are as explained in Section 2.2, Eq. (2-1). The cross section is defined per nucleus but when the scattering experiment is performed, it must be performed with a sample containing many nuclei and, of course, the N nuclei will be of finite size relative to the laboratory scale. This finite size requires the implementation of several corrections when attempting to determine a microscopic quantity (the differential cross section per nucleus) by scattering neutrons off a macroscopic sample containing a very large number (N) of nuclei. Corrections for these effects together with those of air scattering of neutrons are the subjects of this section. Other effects for which the data were not corrected are considered in Appendix 1. Each of these effects was less than one percent.

### 2.4.1 Attenuation Correction

One of the difficulties of scattering from a relatively large size sample is that the incident neutron flux will be attenuated (as neutrons are scattered by the sample) and the nuclei in the scattering sample farthest from the source will see less incident neutron flux than those closest to the source. Refer to Figure 2.10.

To correct for this situation, we replace N(ENO), the neutrons (/sec) incident upon the sample (neutron source side), with N(ENO)ave, the average number of neutrons incident on all the nuclei in the scattering sample. We relate N(ENO)ave to N(ENO) as follows:

$$N(ENO)_{AVE} = \frac{N(ENO)}{\pi a^2} \iint_{-a}^{+a} e^{-n\sigma_T (x + \sqrt{a^2 - y^2})} \, dx\, dy$$

or

$$N(ENO)_{AVE} = f \cdot N(ENO)$$

where:

$n$ = number of nuclei/cm$^3$ and

$\sigma_T$ = total cross section.

This integration can be solved in closed form (Co 67) to give:

$$f = \frac{1}{n\sigma_T a} \left\{ I_1(2n\sigma_T a) - L_1(2n\sigma_T a) \right\}$$

where:

$$I_1 = \frac{x}{2} \sum_{k=0}^{\infty} \frac{(x/2)^{2k}}{k!\,\Gamma(k+2)}$$

- modified Bessel function of the first kind and

$$L_1 = \left(\frac{x}{2}\right)^2 \sum_{k=0}^{\infty} \frac{(x/2)^{2k}}{\Gamma(k+\frac{3}{2})\,\Gamma(k+\frac{5}{2})}$$

- modified Struve function of the first kind.

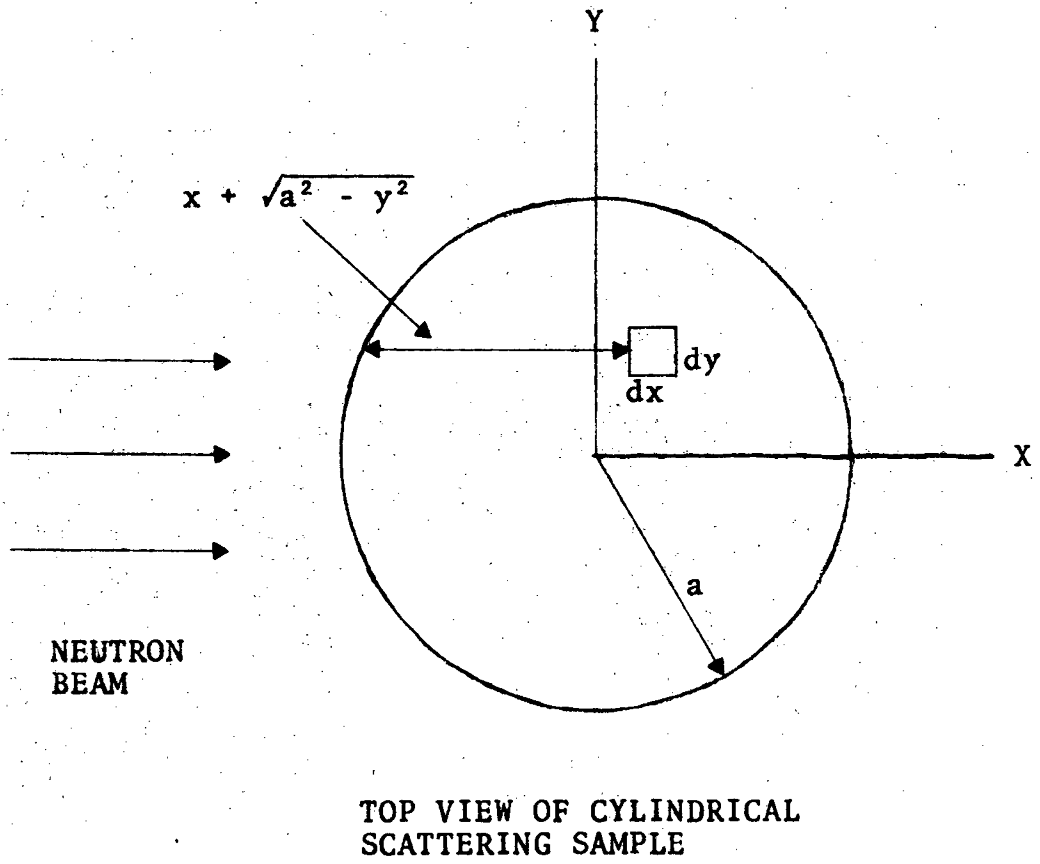

Figure 2.10

If radius a is such that the transmission is less than approximately one, then nuclei in the right side of the scattering sample will see an average neutron intensity which is less than the left side due to the left side scattering neutrons out of the incident beam.

The correction factor, f, was calculated by the function ATTEN, a subroutine of the on-line data analysis program. It is clear that f is energy dependent as it is a function of the total cross section. An energy-total cross section mesh, similar to those discussed in Section 2.3, was employed by ATTEN so that the proper energy dependence of the total cross section could be considered. For incident neutron energies between 4 MeV and 8 MeV, the average value of ATTEN, i.e., 1/f, was 1.15.

### 2.4.2 Air Scattering Correction

Inherent in the present experimental measurement is the error incurred due to the attenuation or scattering of neutrons by the air between the scattering sample and the detector. This problem exists because the neutron flight path is rather long and is changed during the experiment. Consider the experimental geometry in Figure 2.11 which is a superposition of Figures 2.7 and 2.8. For the relative efficiency measurement where $Y_{DET}^{CTD}(END)$ and $Y_{MON}^{CTD}(ENM)$ are determined, the tritium gas cell pressure is reduced from 18 psi to 2 psi. This reduction in gas cell pressure reduces the large zero-degree neutron flux and, with the main detector at zero degrees and at a distance of 7.5 m, the count rate in the detector is such that there exists no electronic dead time problem as would be the case with neutron flux from a cell containing 18 psi. In order to maintain a count rate similar to that of the detector in the

## DIAGRAM FOR AIR SCATTERING CORRECTION

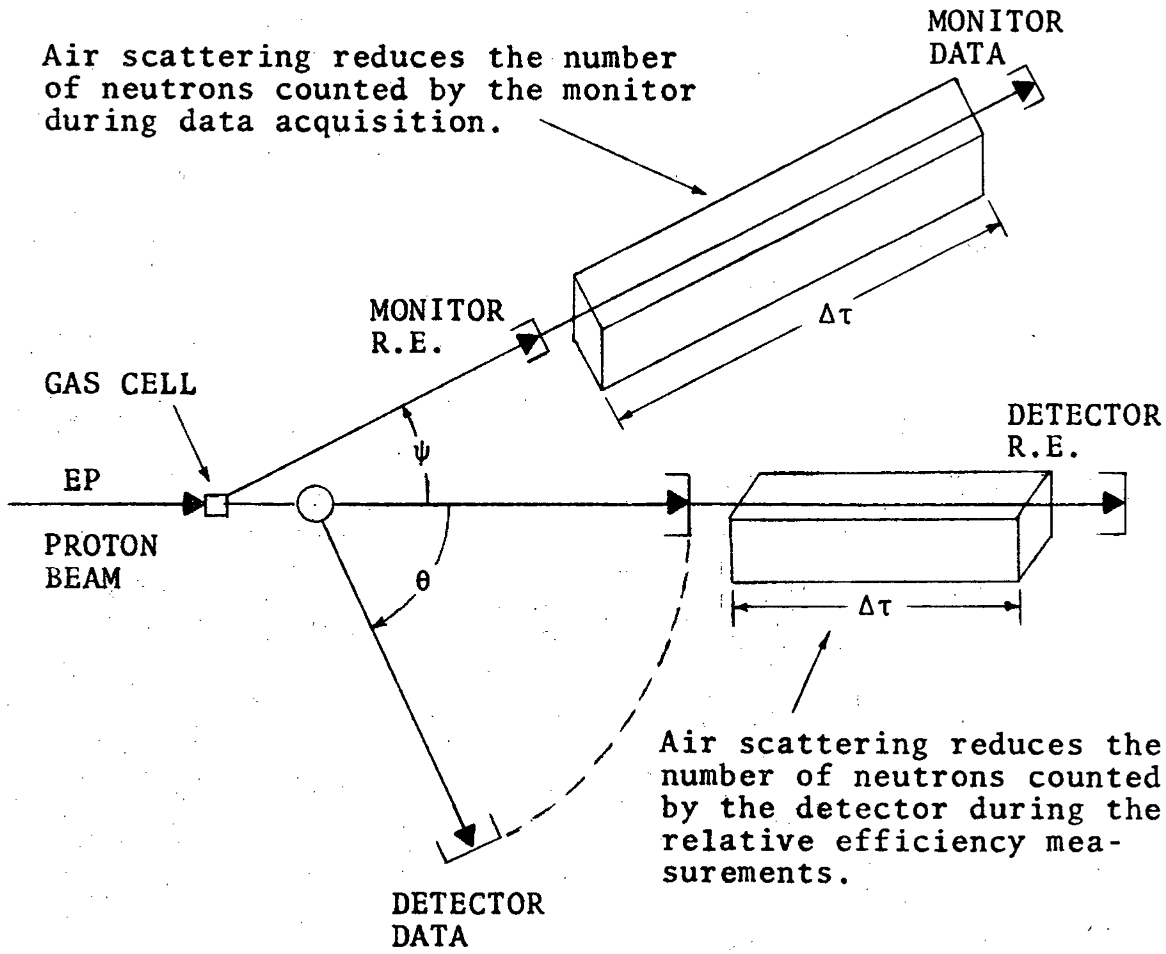

Air scattering reduces the number of neutrons counted by the monitor during data acquisition.

Air scattering reduces the number of neutrons counted by the detector during the relative efficiency measurements.

θ-typical scattering angle of differential cross section measurement.

ψ-permanent angle of neutron source monitor with respect to the zero degree line.

R.E.-signifies position during relative efficiency measurements.

DATA-signifies position during actual data acquisition.

Figure 2.11

much smaller monitor, the monitor is moved toward the gas cell (while carefully maintaining angle $\psi$). Both these changes of position (of monitor and detector) for the relative efficiency measurement introduce error into Eq. (2-19) as can be seen in Figure 2.11.

The air contained in the hypothetical box between MONITOR-R.E. and MONITOR-DATA attenuates the neutron flux such that the number counted at the MONITOR-DATA position is actually less than it should be. Similarly, the number counted by the detector at position DETECTOR-R.E. is less than it should be. Recalling Eq. (2-19):

$$\sigma(\theta ENO) = CON \times \left\{ \frac{N^{CTD}_{DET}(\theta,ENS)}{N^{CTD}_{MON}(\psi,ENM)} - \frac{N^{CTD}_{DET}(S.O.)}{N^{CTD}_{MON}(S.O.)} \right\} \times \frac{Y^{CTD}_{MON}(ENM)}{Y^{CTD}_{DET}(ENS)} \times \frac{\sigma_{T(P,N)}(0^\circ,EP')}{\sigma_{T(P,N)}(0^\circ,EP)}$$

we see that $N^{CTD}_{MON}(\psi,ENM)$, $N^{CTD}_{MON}(S.O.)$, and $Y^{CTD}_{DET}(ENS)$ are all reduced. Therefore, $\sigma_{Meas}(\theta,ENO)$ is greater than $\sigma_{TRUE}(\theta,ENO)$ and a correction must be applied to $\sigma_{MEAS}(\theta,ENO)$. We consider the following:

$$T = e^{-n\sigma}$$

where:

$T$ = transmission

$n$ = number of nuclei/barn

$\sigma$ = cross section in barns

Utilizing the expansion for $e^{-n\sigma}$ yields:

$$T = e^{-n\sigma} = 1 - n\sigma + n^2\sigma^2/2! + \cdots\cdots$$

Then

$$R = 1 - T = n\sigma - n^2\sigma^2/2! + \cdots\cdots \qquad (2\text{-}20)$$

where R is the removal. For air we may write:

$$n\sigma = n_{N_2}\sigma_{N_2} + n_{O_2}\sigma_{O_2}$$

where $N_2$ and $O_2$ represent the corresponding factors for nitrogen and oxygen respectively. If we consider the volume of a colunm of air as shown below:

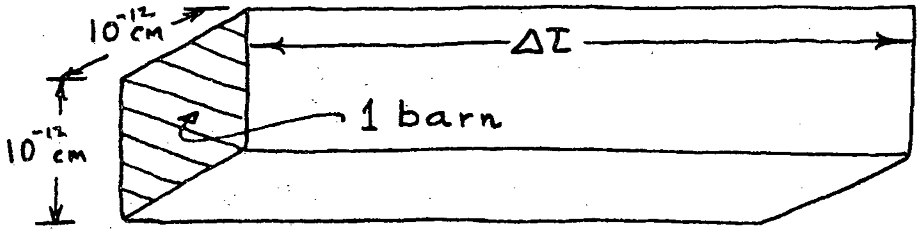

where $\Delta\tau$ represents the change in distance from R.E. measurement to DATA measurement for either monitor or detector, we can calculate the removal, R, for both monitor and detector, i.e., ignoring higher order terms in Eq. (2-20) because nσ is small in this case, we can write:

$$R_{DET} = n\sigma_{DET} = (n_{N_2}\sigma_{N_2} + n_{O_2}\sigma_{O_2})_{DET}$$

$$R_{MON} = n\sigma_{MON} = (n_{N_2}\sigma_{N_2} + n_{O_2}\sigma_{O_2})_{MON}$$

Therefore:

$$Y^{CTD}_{DET\,TRUE}(ENS) = \left(\frac{1}{1 - R_{DET}}\right) Y^{CTD}_{DET}(ENS)_{MEAS}$$

$$N^{CTD}_{MON\,TRUE}(\psi, ENM) = \left(\frac{1}{1 - R_{MON}}\right) N^{CTD}_{MON}(\psi, ENM)_{MEAS}$$

On the average

$$\left(\frac{1}{1 - R_{DET}}\right) \approx \left(\frac{1}{1 - R_{MON}}\right) \approx 1.025$$

and

$$\sigma_{TRUE}(\theta, ENO) \approx 0.95\, \sigma_{MEAS}(\theta, ENO)$$

Throughout the range of neutron energies measured in this experiment, the correction due to air scattering was approximately five percent. The corrections were applied automatically to the data by the on-line data analysis program utilizing function AIRSC. AIRSC contained an energy-cross section mesh for both nitrogen and oxygen and, therefore, considered the energy-dependence of the total neutron cross sections of both those elements.

### 2.4.3 Multiple Scattering Corrections

The multitude of problems normally existing with proper and accurate multiple scattering corrections are further complicated on the very light nuclei because the energy of scattered neutrons is considerably less due to the kinematic shift and because significant resonance structure exists in the neutron cross section to be corrected. Also, the energy resolution of the T.O.F. system changes from forward to backward angles for a fixed flight path and fixed incident energy. Multiple scattering corrections are, of course, sensitive to this energy resolution. An excellent reference on multiple scattering utilizing the Monte-Carlo method is Cashwell and Everett (Ca 59).

For multiple scattering corrections to the present data, A.B. Smith's Monte-Sample Multiple Scattering Code (Sm 75) from the Argonne National Laboratory (ANL) was employed. It was the only program known to exist that was practical, reliable, and usable on our IBM 360 computer and fully applicable to this problem. This code was extensively rewritten to speed up the long Monte-Carlo process and was checked through more than 45 hours of IBM 360/44 computer time. During this process, at each angle, plots of correction factors vs. the number of histories were made from 500k to 3M histories to assure convergence of the corrections. Many test cases were run on this revised code. The code, as it has been rewritten at Ohio University, executes approximately five times faster than the original ANL version. While running times vary significantly with sample size, transmission, etc., the code will execute for a sample of 80 percent transmission approximately one million histories in 45 minutes on an IBM 360/44.

The Monte-Sample Code will handle elastic and inelastic scattering and reactions, and takes as input information a total cross section library as well as an angular distribution library, and therefore includes energy-dependence of differential cross sections of multiple events necessary for light nuclei. The code further employs an energy resolution quantity determined by the T.O.F. system as input information. Figure 2.12 is a plot of the angular distribution of neutrons scattered from $^{11}B$ at an incident neutron energy of 6.25 MeV. Figure 2.13 is a plot of the correction factors (KI) vs. angle for this same angular distribution taken on $^{11}B$. From this plot average multiple scattering corrections for most of the data can be ascertained. The data in this experiment were corrected assuming a maximum of three possible collisions for a single incident neutron. The overflow, i.e., the number of neutrons scattered more than three times in two million histories, was approximately 1000 or 0.05 percent of the total number of neutrons incident on the sample. The multiple scattering code was executed for two million histories for each angular distribution corrected. From the statistics of neutrons scattered per angle (bin count) and from convergence of correction factors vs. histories, the uncertainty in the corrections was determined to be approximately 1.5 percent. The correction factors vs. angle were obtained from the Monte-Sample Code and a program written for the Laboratory's IBM 1800 computer then applied automatically the corrections to the data and finalized cards were then punched for printing tables.

## 2.5 Error Analysis

As stated previously, the final question in almost any nuclear data measurement is how accurately the data taken represent the real system one has set out to measure. It is the opinion of the author that the final error bars assigned

# ANGULAR DISTRIBUTION CORRESPONDING TO MULTIPLE SCATTERING CORRECTIONS OF FIGURE 2.13

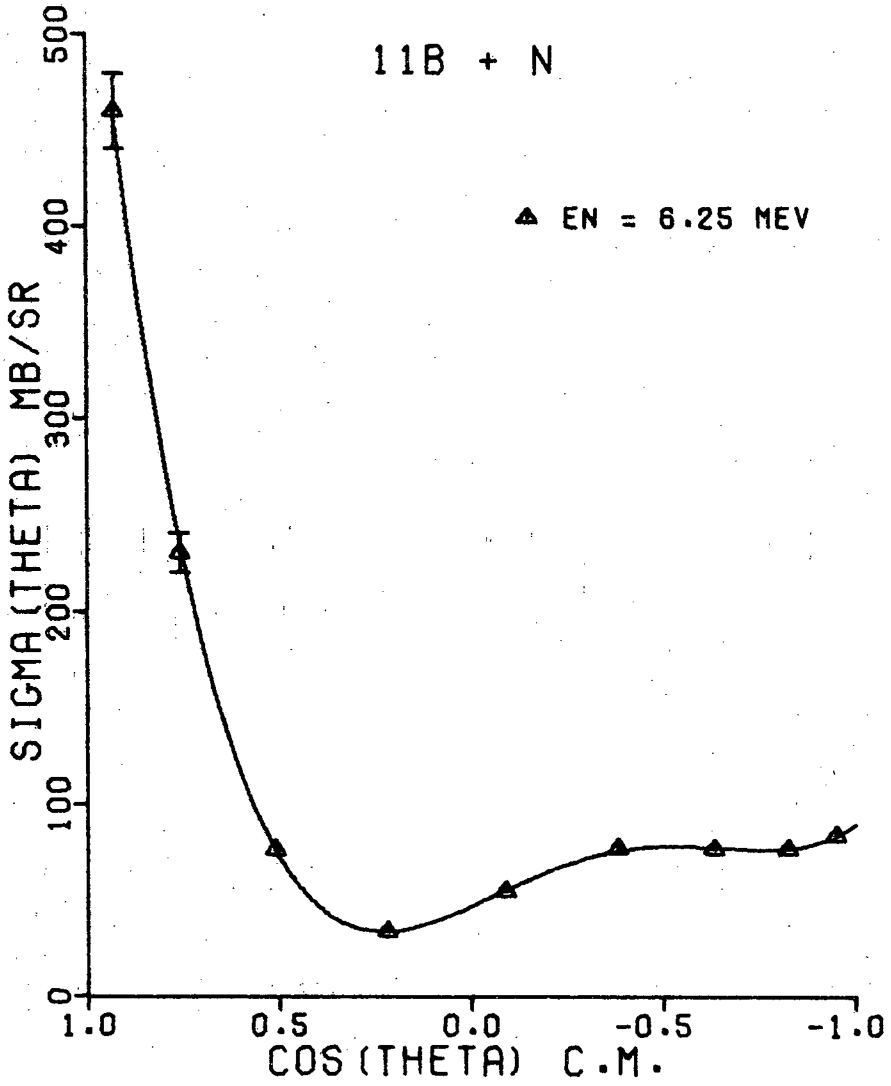

Figure 2.12

## MULTIPLE SCATTERING CORRECTION FACTORS VS. LAB ANGLE

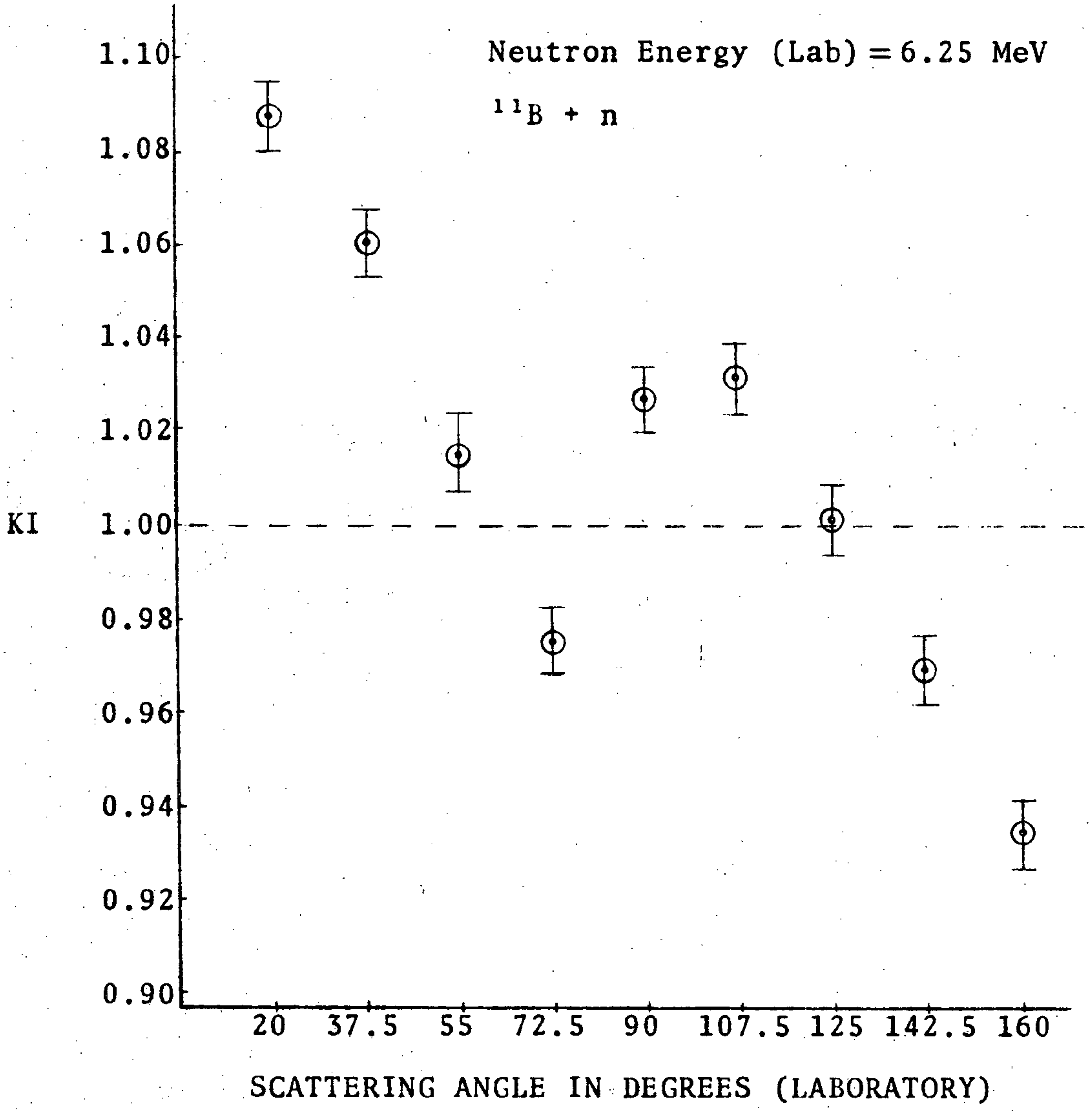

Figure 2.13

to the data should attempt, as far as possible, to answer just that question. That is, the error bars should represent the absolute and total uncertainly in the data, not just statistical uncertainty or just systematic errors. The following procedure was employed to determine the absolute error in the data of this experiment.

We wish to determine a quantity, x, which is a function of at least two other variables, say u and v, which are actually measured. The characteristics of x are determined from those for u and v and from the functional dependence x = f(u,v,...). Bevington (Be 69) derives the standard deviation for x, $\Delta x$ , which can be expressed as:

$$\Delta x^2 = \Delta_u^2\left(\frac{\partial x}{\partial u}\right)^2 + \Delta_v^2\left(\frac{\partial x}{\partial v}\right)^2 + 2\Delta_{uv}\left(\frac{\partial x}{\partial u}\right)\left(\frac{\partial x}{\partial v}\right) + \cdots \qquad (2\text{-}21)$$

The first two terms (averages of squares of deviations) will presumably dominate. The third term is the average of cross terms of deviations in u and v simultaneously. If u and v are uncorrelated, one would expect to find, on the average, approximately equal positive and negative values for these terms and their contribution would vanish. Therefore, if the fluctuation in the observations of u and v are uncorrelated, the equation for $\Delta x$ , Eq. (2-21), can be written:

$$\Delta x^2 = \Delta_u^2\left(\frac{\partial x}{\partial u}\right)^2 + \Delta_v^2\left(\frac{\partial x}{\partial v}\right)^2 + \cdots \qquad (2\text{-}22)$$

If we now consider a form of Eq. (2-19) with no terms divided out, i.e., no simplifying assumptions made, we may write:

$$\sigma(\theta,ENO) = \frac{RSS^2 \cdot RMR^2 \cdot RDS^2}{N \cdot RMD^2 \cdot RDZ^2} \times \left\{ \frac{N^{CTD}_{DET}(\theta,ENS)}{N^{CTD}_{MON}(\Psi,ENM)} - \frac{N^{CTD}_{DET}(S.O.)}{N^{CTD}_{MON}(S.O.)} \right\} \times \frac{Y^{CTD}_{MON}(ENM)}{Y^{CTD}_{DET}(ENS)} \times \frac{\sigma_{T(p,n)}(0^\circ,EP')}{\sigma_{T(p,n)}(0^\circ,EP)} \times \frac{Y(np'os)}{Y(npos)} \times \frac{n'_s}{n_s} \qquad (2\text{-}23)$$

To make Eq. (2-23) a bit more manageable, let us reassign quantities in Eq. (2-23) as follows:

$$CON = \frac{RSS^2 \cdot RMR^2 \cdot RDS^2}{N \cdot RMD^2 \cdot RDZ^2}$$

$$CSISO = \frac{N^{CTD}_{DET}(\theta,ENS)}{N^{CTD}_{MON}(\Psi,ENM)} - \frac{N^{CTD}_{DET}(S.O.)}{N^{CTD}_{MON}(S.O.)}$$

$$RE = Y^{CTD}_{MON}(ENM) / Y^{CTD}_{DET}(ENS)$$

$$XS = \sigma_{T(p,n)}(0^\circ,EP') / \sigma_{T(p,n)}(0^\circ,EP)$$

$$YNP = Y(np'os) / Y(npos)$$

$$NS = n'_s / n_s$$

Then:

$$\sigma(\theta,ENO) = CON \times CSISO \times RE \times XS \times YNP \times NS \qquad (2\text{-}24)$$

From Eq. (2-22) and a little algebra we obtain:

$$\frac{\Delta\sigma^2(\theta,ENO)}{\sigma^2(\theta,ENO)} = \frac{\Delta CON^2}{CON^2} + \frac{\Delta CSISO^2}{CSISO^2} + \frac{\Delta RE^2}{RE^2} + \frac{\Delta XS^2}{XS^2} + \frac{\Delta YNP^2}{YNP^2} + \frac{\Delta NS^2}{NS^2} \qquad (2\text{-}25)$$

We now consider each term in Eq. (2-25). The first term involves distances and the total number of nuclei in the sample, all of which were measured to one percent or less. The second term in Eq. (2-25) involves the counting statistics which varied somewhat but were usually less than two percent. The statistics of the third term, involving relative efficiency measurements, were always less than two percent. The uncertainty in the shape of the zero-degree yield of the tritium (p,n) reaction was considered known to about one percent (Appendix 4). The fifth term in Eq. (2-25), involving charge normalization, was assigned one percent (Appendix 2) and finally, the last term in Eq. (2-25) is discussed in Appendix 3 and the uncertainty of this term was three percent. Solving Eq. (2-25) with the various values discussed above yields:

$$\Delta\sigma(\theta,\mathrm{ENO}) = 0.045 \times \sigma(\theta,\mathrm{ENO})$$

or an uncertainty in the measured differential cross section of approximately 4.5 percent. When the uncertainty in the corrections due to multiple scattering are taken in to account, we arrive at

$$\Delta\sigma(\theta,\mathrm{ENO}) = 0.047 \times \sigma(\theta,\mathrm{ENO})$$

or a total uncertainty of approximately 4.7 percent. In Section 2.6, where comparisons of angular distributions on $^{12}$C taken by the present system are compared with those of several other laboratories, we will see that this error assignment for the total and absolute error of the differential cross sections of $^{11}B + n$ measured in the present experiment is indeed verified. The statistical errors in Eq. (2-25) are taken into account automatically by the on-line data analysis program and, therefore, the error in the data will reflect to some extent the counting statistics of a given energy-angle measurement.

## 2.6 System Calibration and Accuracy

The present method of data reduction is dependent, as are other methods, on the stability of the electronic systems during the experiment. This section will first address itself to the problem of setting the bias level of the main neutron detector and monitor, and the associated problem of system stability. Comparisons of measurements by this system with those of other laboratories will then be discussed.

There exist two prime objectives when the detector (or monitor) bias is set: 1) it should be set high enough to eliminate background or unwanted "noise", and 2) it must be set low enough to detect with good efficiency the lowest energy neutrons one wishes to measure. A standard rule-of-thumb used in this experiment was to set the bias at one-half the minimum neutron energy to be detected, e.g., if the lowest energy neutron incident on $^{11}B$ was 4.0 MeV, then at 160 degrees, the scattered neutron energy would be 2.8 MeV and the bias would therefore be set at approximately 1.4

MeV.

The procedure used in setting the bias was reasonably simple. Compton spectra of recoil electrons from gamma rays from the radioactive isotopes $^{60}$Co and $^{137}$Cs were accumulated in the Nuclear Data 3300 multichannel analyzer (MCA). $^{60}$Co and $^{137}$Cs gamma rays correspond to 1.04 MeV and 0.478 MeV maximum recoil electrons, respectively. These two points (half way points on the Compton edges) give a relatively good electron-recoil-energy vs. channel-number calibration. Using an electron vs. proton energy response curve for NE224 liquid scintillator (Cz 64) and an extrapolated response curve based on NE218 (Ma 70), one can determine the channel corresponding to the electron-, and hence, proton-recoil-energy corresponding to the neutron energy at which the bias is to be set.

As described in Section 2.3 and illustrated in Figure 2.9, the detector dynode signal was routed to an Ortec 460 delay line amplifier (DLA) and on to an Ortec 420 single channel analyzer (SCA). The bias level or threshold was set with the SCA in integral mode and displayed in the MCA so that the proper cut-off channel could be verified. For this application, a bias level set to within 50 keV of the desired level was satisfactory.

Significantly more important is the ability of the electronic system to maintain a constant bias level without drifting. To insure that this was indeed the case, gated and ungated spectra of $^{60}$Co and $^{137}$Cs were taken daily utilizing the dashed line circuitry shown in Figure 2.9. First, ungated (total Compton spectrum) dynode pulses were accumulated in ADC's 4 and 5 for the detector and monitor, respectively. Then, the same signals were gated by the SCA (all signals greater than a cut-off or threshold level) and again accumulated in ADC's 4 and 5. All this information was stored on a computer disk. The runs were precisely timed and radioactive sources were maintained carefully at the same geometry for each of these measurements. These gamma checks were made at least once a day for the duration of data acquisition. Figure 2.14 shows overlays of four such checks throughout several days. The advantage of this kind of check is twofold: 1) it demonstrates the stability of the SCA used, in this case, as an input discriminator and 2) it will certainly show up clearly any drift of electronic system gain from the photomultiplier tube to the MCA. As can be seen from Figure 2.14, no discernable shift in either input discriminator or overall system gain was observed. Further, as can be seen from Figure 2.14, it is possible to detect a drift of the discriminator as small as a fractional part of a channel, but no change was ever observed in as long as a two week period in either the input discriminator or the electronic gain of the system.

With the neutron-producing and -detecting system as described here-to-fore, with the relatively simple scheme for data reduction, and with the demonstrated stability described above, one should certainly expect to be able to

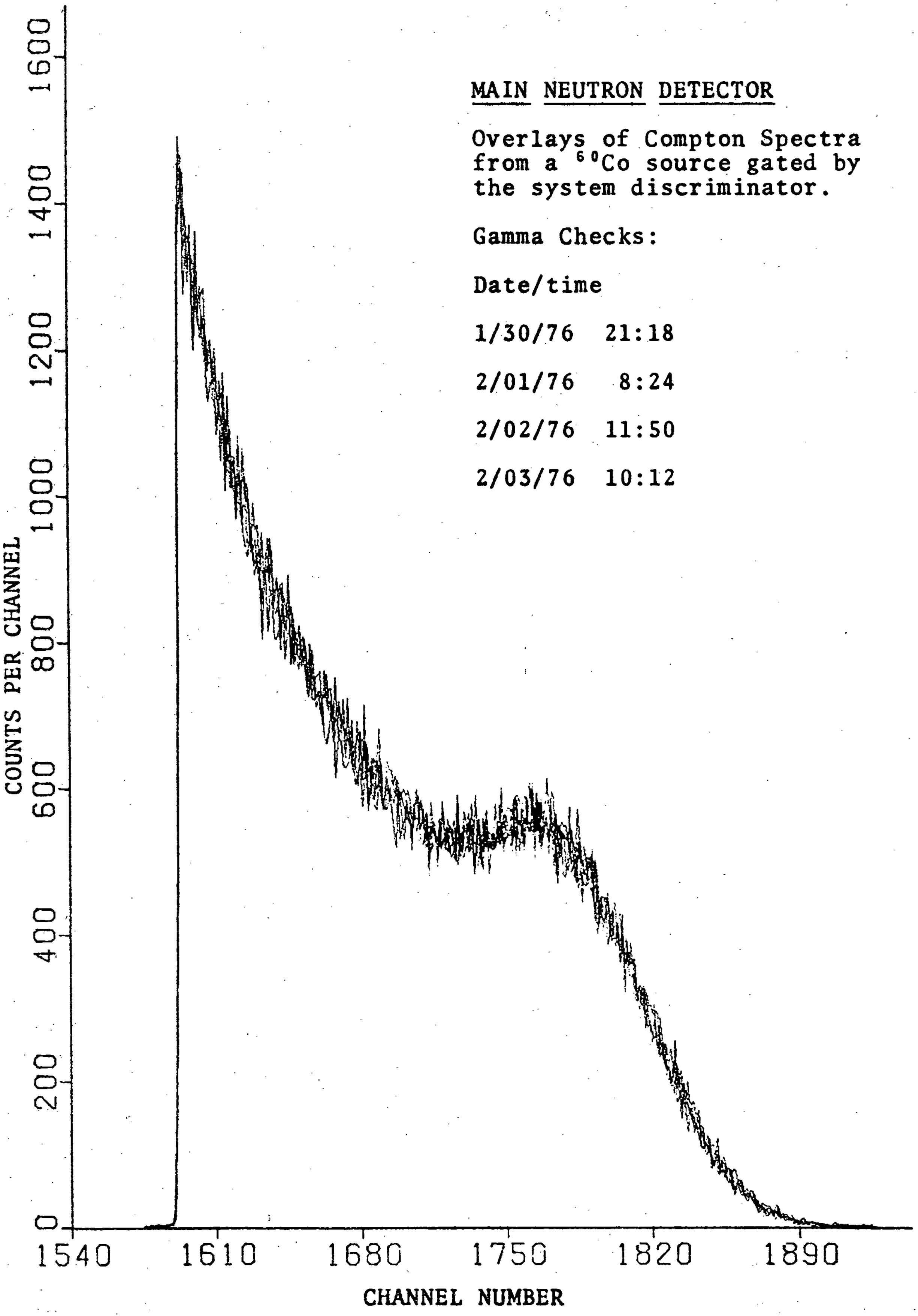

Figure 2.14 Main neutron detector Compton spectra for $^{60}$Co.

measure absolute differential cross sections to within the calculated uncertainty of 4.7 percent. Therefore, we turn now to comparisons of measurements taken by this system with those of several other laboratories with entirely different schemes of data acquisition and reduction.

It is clear that a good check of the total system is to measure the elastic differential cross section on a nuclide that is already well-established. Carbon-12 is such a nuclide with previous measurements by Galati, et al. of the University of Kentucky (Ga 72) and Perey, et al. of the Oak Ridge National Laboratory (Pe 69). Energies selected for measurement of $^{12}C + n$ elastic differential cross sections were subjected to three criteria: 1) cross section measurements must have already been made at useful energies for this experiment, 2) the energies must not lie in regions of significant resonance structure, and 3) the energies should be spaced throughout the energy range of measurements on $^{11}B$.

Differential cross sections in this experiment were measured for $^{12}C + n$ at neutron energies (laboratory frame) of 4.078 MeV, 5.048 MeV, and 6.940 MeV. The $^{12}C$ sample used was machined from reactor grade graphite to a right circular cylinder with a diameter of 3.00 cm, a height of 3.62 cm, and a mass of 48.100 grams. The sample contained $2.414 \times 10^{24}$ carbon atoms and the multiple scattering corrections were similar in magnitude to those for $^{11}B$ discussed earlier. Figure 2.15 shows a graphical comparison of the elastic

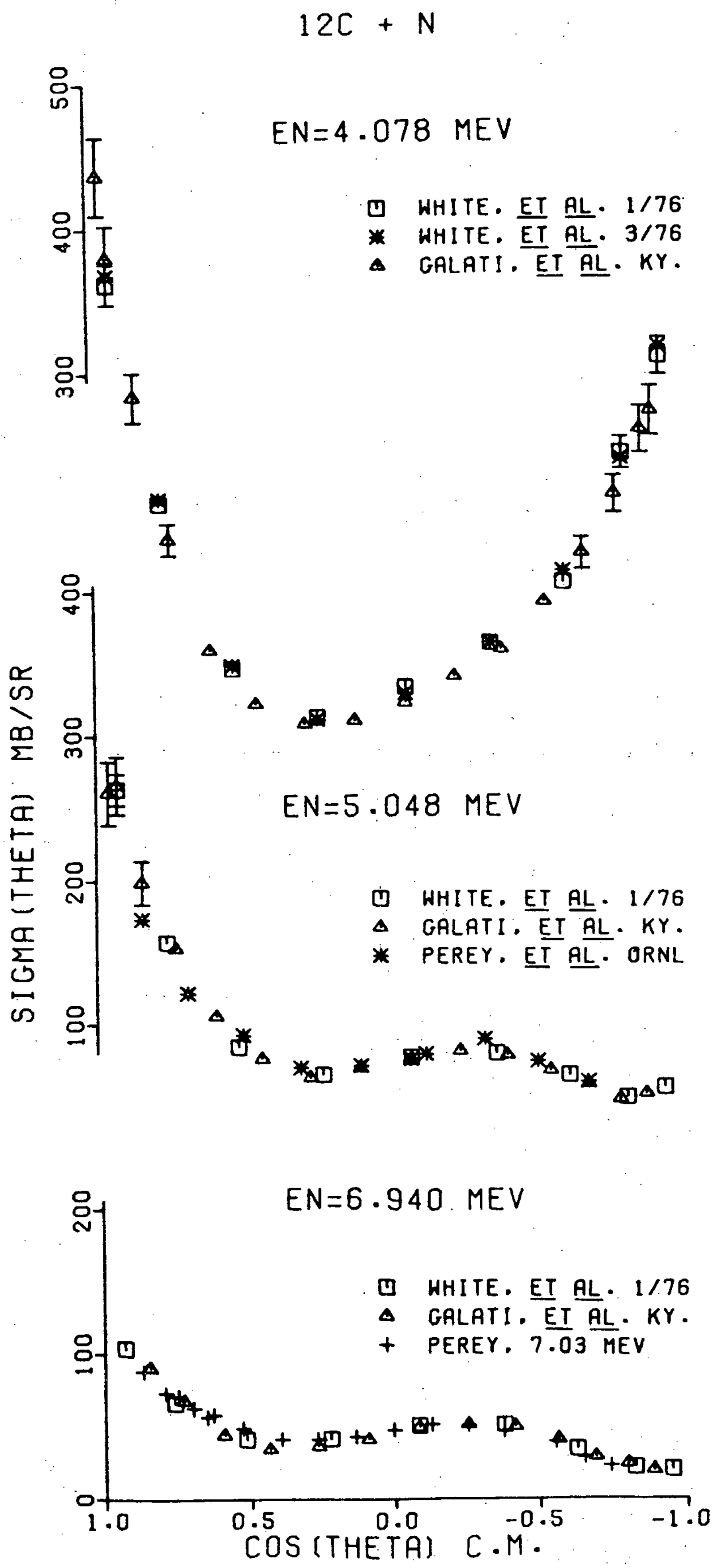

Figure 2.15 Plot of comparisons of $^{12}C$ + n from various laboratories.

differential cross section at these energies with those of Galati, et al. and Perey, et al. It is apparent that both the shape and absolute value of the data are in excellent agreement with both Galati, et al. and Perey, et al. Table 2.2 is a comparison of the integrated elastic cross sections for the data shown in Figure 2.15. Table 2.3 lists the actual differential cross sections taken with this system on $^{12}C$ and further, data taken by a repeat measurement two months later at a different detector bias setting. The agreement in absolute values of these two sets of data establishes the consistency with which measurements can be accomplished with this system.

It should be noted here that the experimental methods and correction codes for each of the three laboratories were entirely different. The fact that the agreement is so good demonstrates the accuracy with which these points can now be considered to be known. The relative ease and straightforward nature of these measurements compared to the hydrogen scattering measurement should certainly establish these points as practical calibration standards for neutron work in this enegy range.

## 2.7 Experimental Results

The data for this experiment were taken in four separate measurements over a nine month period from June, 1975 to February, 1976. The first measurements in June, 1975 covered the neutron energies from 4 MeV to 4.5 MeV. The

Table 2.2

Comparisons of the integrated elastic scattering cross sections for $^{12}C + n$ from the data shown in Figure 2.15. All data were fitted via least-squares to a series of five Legendre polynomials.

| Neutron Energy (Lab) | $B_o$ (mb) | $\sigma_{el} = 4\pi B_o$ (b) |
|---|---|---|
| 4.078 MeV | | |
| White, <u>et</u> <u>al</u>. 1/76 | 152.7 | 1.92 |
| White, <u>et</u> <u>al</u>. 3/76 | 153.8 | 1.93 |
| Galati, <u>et</u> <u>al</u>. Ky. | 147.1 | 1.85 |
| 5.048 MeV | | |
| White, <u>et</u> <u>al</u>. 1/76 | 94.7 | 1.19 |
| White, <u>et</u> <u>al</u>. 3/76 | 95.6 | 1.20 |
| Galati, <u>et</u> <u>al</u>. Ky. | 94.1 | 1.18 |
| Perey, <u>et</u> <u>al</u>. ORNL | 86.8 | 1.14* |
| 6.940 MeV | | |
| White, <u>et</u> <u>al</u>. 1/76 | 48.1 | 604 (mb) |
| White, <u>et</u> <u>al</u>. 3/76 | 48.6 | 611 |
| Galati, <u>et</u> <u>al</u>. Ky. | 48.9 | 614 |
| Perey, 7.03 MeV | 45.6 | 601* |

*Values quoted from reference Pe 69.

## Table 2.3

Comparison of $^{12}C + n$ elastic differential cross sections measured in the present experiment. Angles and cross sections are given in the center-of-mass system. Cross sections are in units of mb/sr. The errors in mb/sr for the 1/76 data are also shown.

Neutron Energy (Lab) 4.078 MeV

| Angle | $\sigma(\theta)$ 1/76 | $\sigma(\theta)$ 3/76 | Error |
|---|---|---|---|
| 21.6 | 362.4 | 368.1 | 15.9 |
| 40.4 | 209.7 | 213.0 | 9.2 |
| 58.9 | 95.6 | 97.5 | 4.5 |
| 77.1 | 61.9 | 60.1 | 3.0 |
| 94.8 | 82.5 | 78.2 | 3.8 |
| 112.1 | 113.6 | 113.5 | 5.4 |
| 128.9 | 155.8 | 163.5 | 8.1 |
| 145.4 | 245.7 | 242.2 | 12.2 |
| 161.6 | 312.9 | 319.5 | 14.5 |

Neutron Energy (Lab) 5.048 MeV

| Angle | $\sigma(\theta)$ 1/76 | $\sigma(\theta)$ 3/76 | Error |
|---|---|---|---|
| 21.6 | 263.5 | 264.1 | 12.5 |
| 40.4 | 157.5 | 161.3 | 7.7 |
| 58.9 | 85.2 | 86.4 | 4.2 |
| 77.1 | 66.0 | 65.4 | 3.1 |
| 94.8 | 78.4 | 78.7 | 3.7 |
| 112.1 | 81.0 | 79.9 | 3.8 |
| 128.9 | 65.7 | 64.0 | 3.2 |
| 145.4 | 49.9 | 51.9 | 2.7 |
| 161.6 | 56.7 | 58.3 | 3.1 |

Neutron Energy (Lab) 6.940 MeV

| Angle | $\sigma(\theta)$ 1/76 | $\sigma(\theta)$ 3/76 | Error |
|---|---|---|---|
| 21.6 | 104.1 | 104.7 | 5.2 |
| 40.4 | 66.5 | 67.8 | 3.4 |
| 58.9 | 41.8 | 41.4 | 2.1 |
| 77.1 | 41.8 | 43.9 | 2.0 |
| 94.8 | 50.8 | 51.9 | 2.5 |
| 112.1 | 51.0 | 49.6 | 2.4 |
| 128.9 | 34.8 | 34.8 | 1.7 |
| 145.4 | 21.5 | 20.1 | 1.2 |
| 161.6 | 20.1 | 22.9 | 1.4 |

July, 1975 run extended these measurements to 5.5 MeV and the September, 1975 run extended the measurements to 7.5 MeV. In January, 1976 a remeasurement of the differential cross sections for neutron energies from 4 MeV to 5 MeV and from 6.5 MeV to 8 MeV was made. This series of measurements (always overlapping with the previous measurements) and remeasurement afforded numerous opportunities for comparisons of consistency of the differential cross section measurements. The results on $^{12}C + n$, shown in Figure 2.15 and Table 2.3, are typical of the consistency of measurements also obtained on $^{11}B + n$.

The differential cross sections were measured for nine laboratory angles from 20 degrees to 160 degrees at 17.5 degree increments. Figure 2.16 is a plot of a typical time-of-flight spectrum for both sample in and sample out for an incident neutron energy of 6.25 MeV and scattering angle of 125 degrees. Figure 2.17 shows a normalized subtracted spectrum of the two spectra in Figure 2.16. Tabular results for the differential cross sections are given in Appendix 7. Each angular distribution (center of mass system) was least-squares fitted to a series of Legendre polynomials, i.e.,

$$\sigma(\theta, \mathrm{ENO}) = \sum_L B_L(\mathrm{ENO})\, P_L(\cos\theta)$$

Figure 2.18 is a plot of the Legendre expansion coefficients $B_L(\mathrm{ENO})$ as a function of laboratory neutron energy for L values up to and including L=5. It is clear from Figure 2.18 that partial waves up to and including $\ell=2$ (L=4)

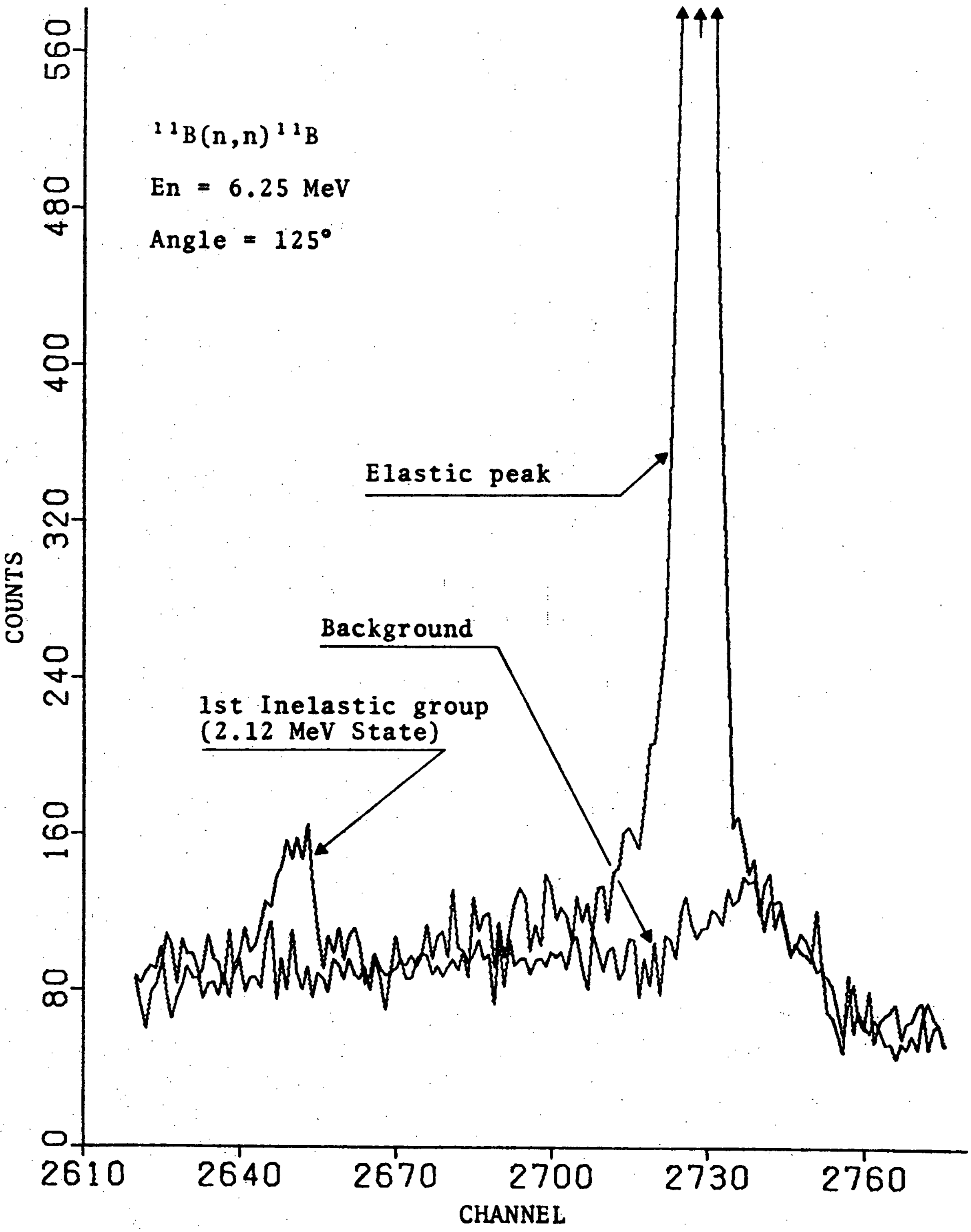

Figure 2.16 Typical time-of-flight spectra for both sample in and sample out measurements.

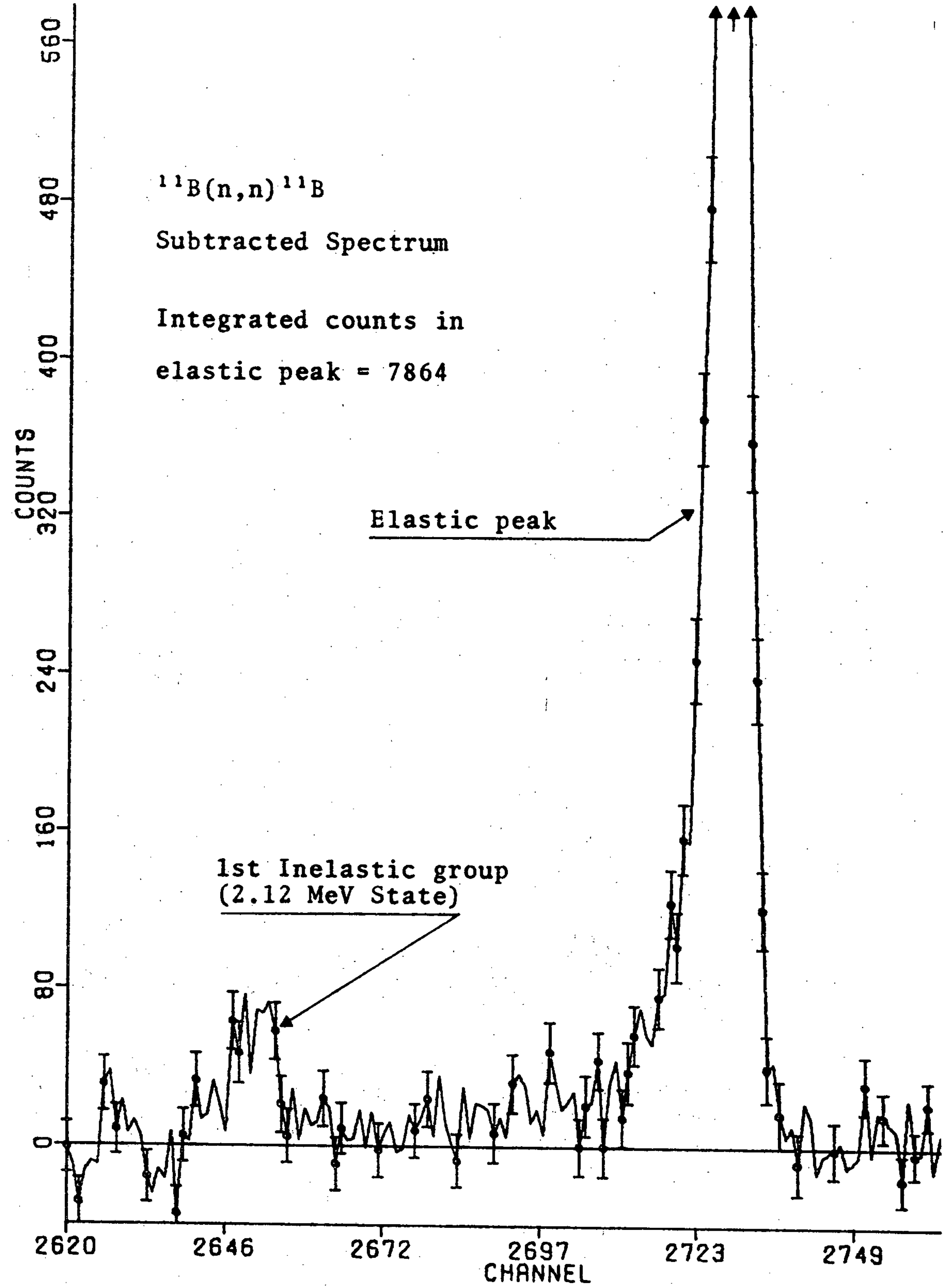

Figure 2.17 Subtracted spectrum of the two spectra in Figure 2.16.

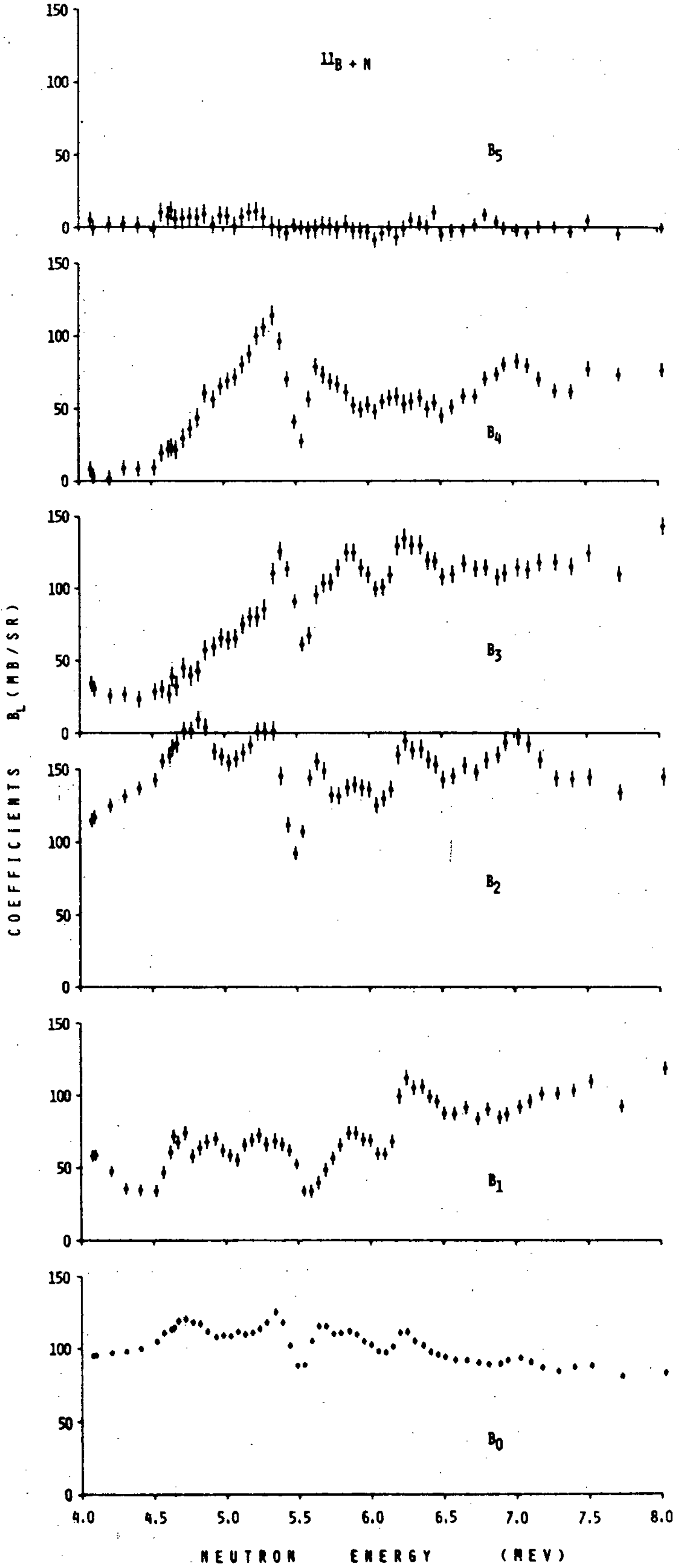

Figure 2.18 Plot of Legendre Expansion Coefficients vs. Laboratory Neutron Energy for L≤5.

are present in this experiment. Figure 2.19 is a plot of the Legendre expansion coefficients from a least-squares fit with L=4. The Legendre expansion coefficients for all the data are given in tabular form in Appendix 8. Also included in Figure 2.19 are various angular distributions measured at the indicated energies to show the changes in the relative shape of those distributions with energy. From this figure several general features are clear. The d-wave ($\ell$=2) strength becomes significant about 4.5 MeV. The large dip at 5.5 MeV which has been seen previously (Fo 61, Ca 71) in total cross section measurements is pronounced through all of the Legendre coefficients and is therefore formed by d-waves as partial waves with $\ell$=2 is the only way to reach the B4 coefficient. These resonance effects will be discussed thoroughly in Section 3.4 on results of the R-matrix analysis.

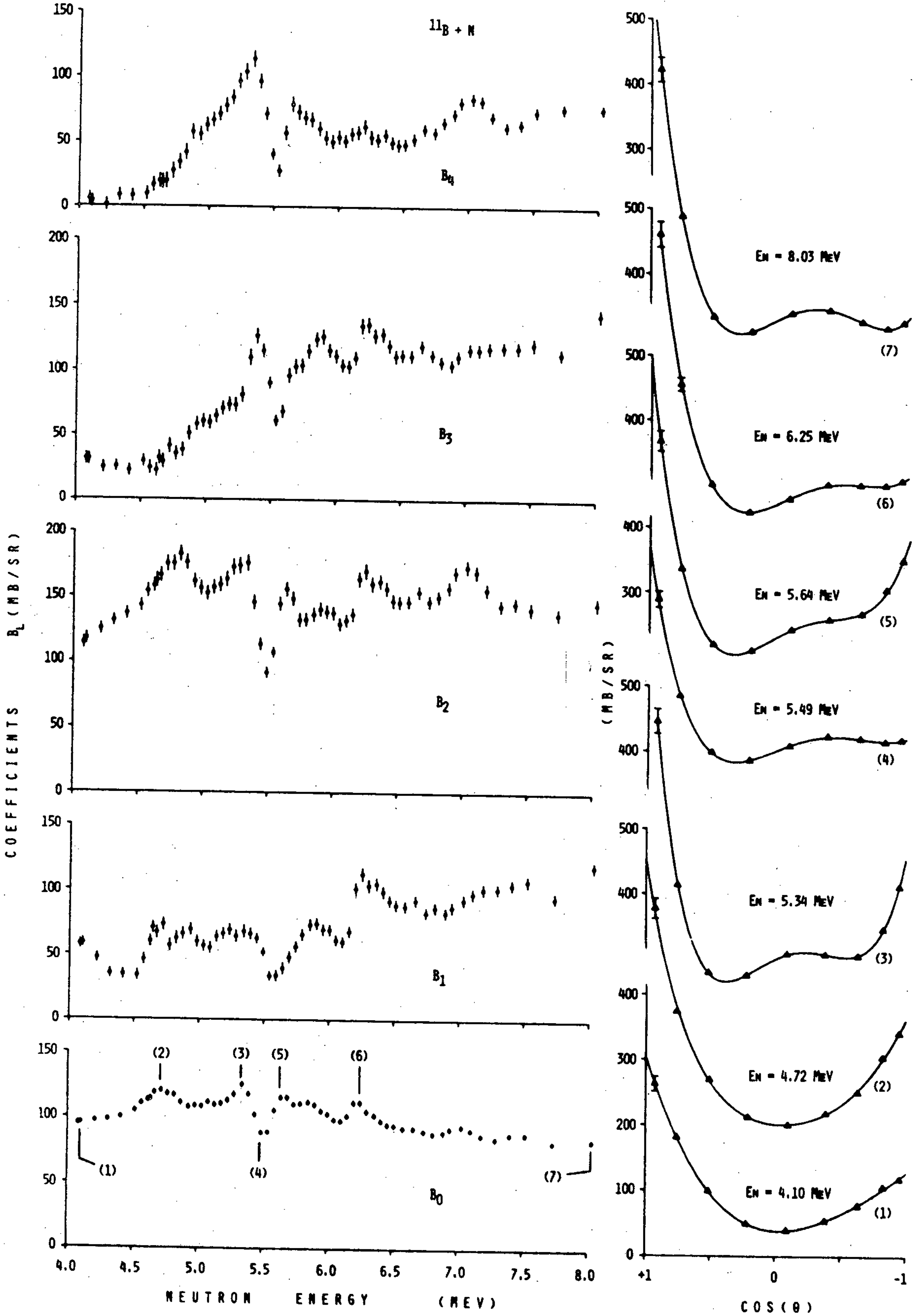

Figure 2.19 Coefficients $B_L$ and representative angular distributions of $\sigma_{n_0}(\theta)$ for $^{11}$B + n.

# CHAPTER 3

# DATA ANALYSIS

## 3.1 General Scattering Theory

It is apparent from the previous chapter that a significant effort is involved in obtaining differential cross sections to an uncertainty of less than five percent. In this chapter, it will be shown why this kind of measurement is important, i.e., how actual nuclear structure information is derived from the measurement of angular distributions of neutrons scattered from light nuclei. We first consider a review of the general scattering problem with the various angular-momentum coupling schemes. We will derive the relation between the scattering matrix and the differential cross section in a given coupling scheme by partial wave expansion and then consider the transformation of the scattering matrix from one coupling scheme to another.

Section 3.2 will consider the R-matrix theory which is a resonance theory suitable for application to the kind of compound resonance reactions observed in the Legendre polynomial expansion coefficients of the differential cross sections taken on $^{11}$B via the $^{11}$B(n,n)$^{11}$B reaction. The R-matrix theory is essentially a reparameterization of the scattering matrix in terms of more physically meaningful (measureable) quantities. The outline of the data analysis scheme, shown in Figure 3.1, will be fully discussed in Sections 3.2 and 3.3. A program to do the data analysis was

## GENERAL OUTLINE OF DATA ANALYSIS SCHEME

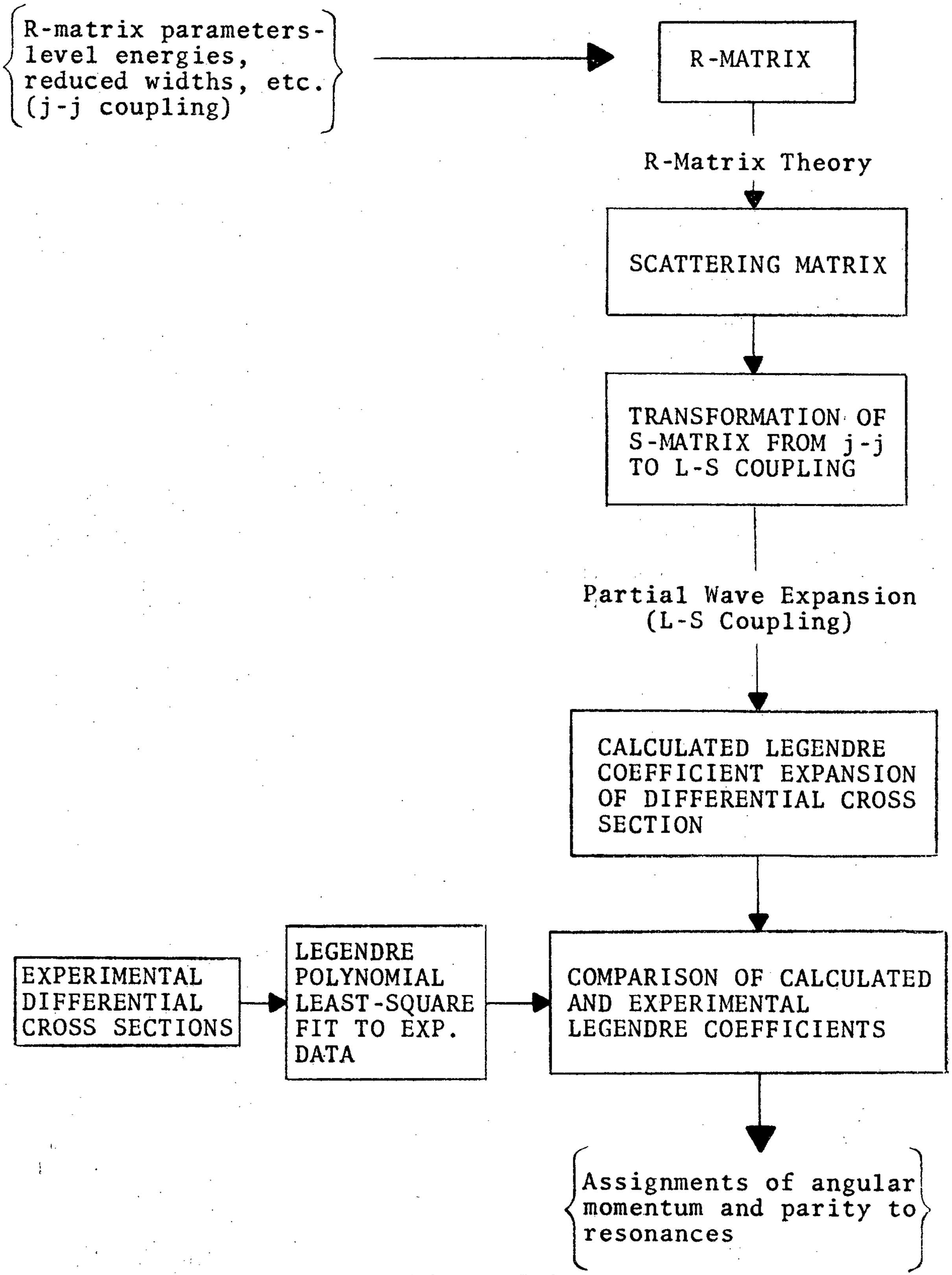

Figure 3.1

written. Salient points for this program are as follows: 1) the various resonance parameters are assumed from an inspection of the experimental data, 2) a choice of either the j-j or L-S coupling scheme is made and the R-matrix is formed, 3) the scattering matrix is formed from the R-matrix, 4) if the coupling scheme used is j-j, the scattering matrix is transformed to L-S coupling and 5) the Legendre polynomial expansion coefficients of the differential cross sections are calculated in the L-S coupling scheme and compared with those obtained by least-squares fitting to the actual data. From this comparison, definitive assignments of angular momentum and parity for the various resonances of the compound nucleus $^{12}B$ may, in principle, be made. We will see however, that in very complicated spectra such as in the present experiment, definitive assignments may not always be possible, but probable assignments and relative strengths of various partial waves contributing to the resonances may be determined.

The reason for forming the R-matrix in j-j coupling will be explained in the next section. A question may arise as to why, if the R-matrix is formed in the j-j coupling scheme, the calculated Legendre expansion coefficients are derived from the scattering matrix in L-S coupling. The answer is that simplified analytic expressions already exist (Bl 52) to calculate, in an efficient manner, the Legendre coefficients from the scattering matrix in L-S coupling. While the expression for the differential cross section in terms of the scattering matrix in j-j coupling is not employed here, Appendix 5 derives the proper expression which may be used as a working equation for future reference. From this point an investigator needing this approach would be able to work out a compacted formalism for the Legendre expansion coefficients in terms of the scattering matrix in j-j coupling similar to that already accomplished in L-S coupling by Blatt and Biedenharn (Bl 52).

### 3.1.1 Angular Momentum Coupling Schemes

Let us consider the diagram below where a projectile (neutron) is incident upon a target nucleus in its ground state and is thereby scattered from that nucleus at some angle θ with respect to its incident direction.

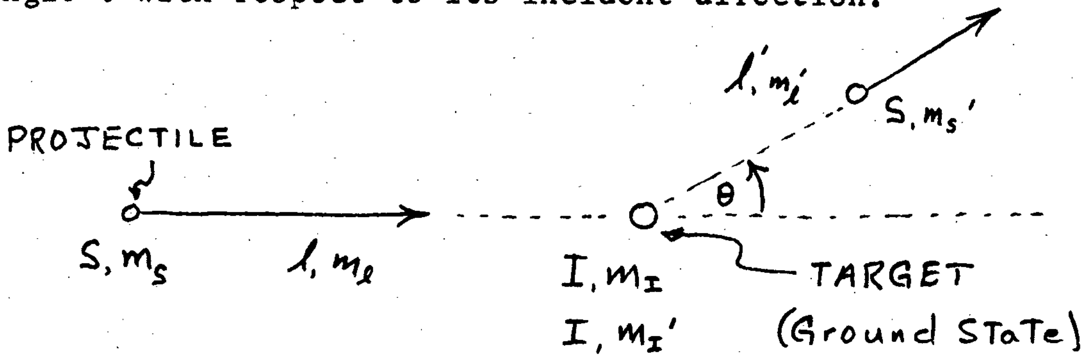

The quantities $S$ and $I$ represent the spins of the projectile and target respectively, $m_S$ and $m_I$ are their quantum projections. The quantum number $l$ is the relative orbital angular momentum of the projectile and the target and $m_l$ its quantum projection. The primed quantities represent the outgoing channel, i.e., the spins and relative orbital angular momentum after scattering. We are only going to consider elastic scattering. Therefore, the spin of the projectile will not change, however, its projection may. Similarly, the spin of the target nucleus will not change but its projection may. As long as the total angular momentum is conserved, the relative orbital angular momentum and its quantum projection may change. An uncoupled wave function describing the system may be written as a product wave function

$$\Psi \propto |l m_l\rangle |S m_s\rangle |I m_I\rangle$$

where $|l m_l\rangle$, $|S m_S\rangle$, and $|I m_I\rangle$ are the wave functions describing the orbital, projectile spin, and target spin angular momenta respectively. To solve the general scattering problem a coupled wave function must be written, and, as there are several ways to vectorially couple the three angular momenta, there are also several ways to couple the wave functions. We consider first the L-S coupling scheme where the two spin vectors are coupled to yield an intermediate "channel spin" vector and this vector is then coupled to the orbital angular momentum, i.e.,

$$\vec{S} + \vec{I} \rightarrow \vec{\mathcal{S}} \quad \text{AND} \quad \vec{l} + \vec{\mathcal{S}} \rightarrow \vec{J}$$

where $\vec{\mathcal{S}}$ is the channel spin and $\vec{J}$ is the total angular momentum. We may write for the wave function:

$$|S m_s\rangle |I m_I\rangle = \sum_{\mathcal{S}} (S I m_s m_I | \mathcal{S} m_{\mathcal{S}}) |\mathcal{S} m_{\mathcal{S}} S I\rangle \tag{3-1}$$

and

$$|\mathcal{S} m_{\mathcal{S}}\rangle |l m_l\rangle = \sum_{J} (l \mathcal{S} m_l m_{\mathcal{S}} | JM) | JM l \mathcal{S}\rangle \quad (3\text{-}2)$$

The uncoupled wave function is represented by the coupled wave function as follows:

$$\psi_{l\text{-}\mathcal{S}} \sim \sum_{J\mathcal{S}} (sI m_s m_I | \mathcal{S} m_{\mathcal{S}})(l \mathcal{S} m_l m_{\mathcal{S}} | JM) | JM l \mathcal{S}\rangle \quad (3\text{-}3)$$

where $|JMl\mathcal{S}\rangle$ represents the coupled wave function and $(sI m_s m_I | \mathcal{S} m_{\mathcal{S}})$ and $(l\mathcal{S} m_l m_{\mathcal{S}} | JM)$ are the vector coupling or Clebsch-Gordan coefficients (Co 35) which tell, essentially, how much of each of the new coupled wave functions is necessary in the sum to represent the uncoupled wave function. A channel (either entrance or exit) is defined in L-S coupling as a set of good quantum numbers $J$, $M$, $l$, and $\mathcal{S}$ in the sense that $|JMl\mathcal{S}\rangle$ is an eigenfunction of the angular momentum operators $\hat{J}^2$, $\hat{J}_z$, $\hat{l}^2$, and $\hat{\mathcal{S}}^2$, i.e.,

$$\hat{J}^2 |JMl\mathcal{S}\rangle = J(J+1)\hbar^2 |JMl\mathcal{S}\rangle, \text{ etc.}$$

Let us now consider the j-j coupling scheme where the projectile spin is coupled to the orbital angular momentum and this intermediate vector is then coupled to the ground state spin of the target nucleus, i.e.,

$$\vec{l} + \vec{S} \rightarrow \vec{j} \text{ AND } \vec{I} + \vec{j} \rightarrow \vec{J}$$

We may write for the wave function describing this system:

$$|l m_l\rangle |s m_s\rangle = \sum_{j} (l s m_l m_s | j m_j) | j m_j l \mathcal{S}\rangle \quad (3\text{-}4)$$

and

$$|j m_j\rangle |I m_I\rangle = \sum_J (j I m_j m_I | J M) \, |J M j I\rangle \qquad (3\text{-}5)$$

The uncoupled wave function is represented by the coupled wave functions as follows:

$$\psi_{j\text{-}j} \sim \sum_{jJ} (l s m_l m_s | j m_j)(j I m_j m_I | J M) \, |J M j I\rangle \qquad (3\text{-}6)$$

where $|J M j I\rangle$ represents the coupled wave function and $(l s m_l m_s | j m_j)$ and $(j I m_j m_I | J M)$ are the vector coupling coefficients. A channel is defined in j-j coupling as a set of good quantum numbers $J$, $M$, $j$ and $I$ in a similar sense to that given above. For the reader who wishes to delve further into angular momentum theory an excellent reference is Rose (Ro 57). The reason the R-matrix is formed with j-j coupling parameters is that we believe the j-j scheme best represents the physical situation for the coupling of $^{11}$B + n. The shell model has been successful in predicting some states from a neutron particle-proton hole configuration where the neutron carries in the orbital and spin (intermediate j) angular momentum and then couples this with the ground state spin $I$ of the nucleus $^{11}$B. Since $^{11}$B always has the same spin $I$, the states $|J M j I\rangle$ have more physical significance than $|J M \ell \mathcal{S}\rangle$. We now proceed to utilize the coupled wave functions developed here in the next section (L-S coupling) and in Appendix 5 (j-j coupling).

### 3.1.2 Partial Wave Expansion

The purpose of this section is to define the scattering matrix, which contains all the information of the scattering process, and then, to develop the relationship between the scattering matrix and the differential cross section (actually the Legendre expansion coefficients of the differential cross section). Now the cross section can be calculated from the scattering matrix in j-j coupling, or the scattering matrix can be transformed from j-j coupling to L-S coupling and the cross section calculated in L-S coupling--it is still the same cross section. We choose to calculate the Legendre expansion coefficients of the differential cross section in L-S coupling because efficient equations, from a calculative point of view, have already been developed (Bl 52). Further, if one wishes to form the R-matrix parameters in L-S coupling, then no transformation is necessary on the scattering matrix before the differential cross sections are calculated.

There are numerous articles (Bl 52, Bl 52a, La 58, Wi 63) in the literature on general scattering theory including the relationship between the scattering matrix and the differential cross section derived in L-S coupling. It is more difficult to find references for the same theory developed in j-j coupling and therefore, Appendix 5 considers the theory in j-j coupling in detail, giving a final working equation for future reference.

We proceed here with the general scattering theory in L-S coupling. From orthogonality properties of the Clebsch-Gordan coefficients, we can write the coupled wave function in terms of the uncoupled wave functions from Eq. (3-2) as follows:

$$|JMl\mathcal{S}\rangle = \sum_{m_l m_s} (l\mathcal{S} m_l m_s | JM) \, |l m_l\rangle \, |\mathcal{S} m_s\rangle \qquad (3\text{-}7)$$

We consider the total wave function as a sum of the incident plane wave (which we will decompose into ingoing and outgoing spherical waves) and the scattered wave (which is composed of an outgoing spherical wave). Then the ingoing part of the total wave function must be equal to the ingoing part of the incident wave and the outgoing part of the total wave function must be the sum of the outgoing part of the incident wave and the outgoing part of the scattered wave.

The most general form of the total wave function will consist, at sufficiently large distances, of the superposition of ingoing and outgoing spherical waves as follows:

$$\psi^{\mathcal{S}}_{TOTAL} \simeq \frac{1}{rV^{1/2}} \sum_{JMl} \left( A^{JM}_{l\mathcal{S}} \, e^{-i(kr - l\pi/2)} - B^{JM}_{l\mathcal{S}} \, e^{+i(kr - l\pi/2)} \right) |JMl\mathcal{S}\rangle \qquad (3\text{-}8)$$

where $|JMl\mathcal{S}\rangle$ is defined in Eq. (3-7). We use the superscript $\mathcal{S}$ to imply that the channel spin is specified. Proper summing over possible channel spins is carried out later. The coefficients on the ingoing and outgoing waves, $A^{JM}_{l\mathcal{S}}$ and $B^{JM}_{l\mathcal{S}}$ respectively, are not independent because if the amplitudes of the ingoing waves are known, the amplitudes of the outgoing waves are determined uniquely by the wave equation. It is the relationship between these two coefficients which defines the scattering matrix, i.e.,

$$B^{JM}_{l's'} = \sum_{ls} S^{J}_{l's',ls} A^{JM}_{ls} \qquad (3\text{-}9)$$

Because the Hamiltonian is invariant under rotation, the scattering matrix cannot depend on M. We may write for the incident plane wave:

$$\psi^{s}_{inc} = e^{ikz} | s m_s \rangle$$

We utilize the common procedure of expanding this plane wave into a series of partial waves, i.e.,

$$\psi^{s}_{inc} = (4\pi)^{1/2} \sum_{l=0}^{\infty} i^{l} (2l+1)^{1/2} j_l(kr) | l 0 \rangle | s m_s \rangle$$

where $| l 0 \rangle = Y_{l0}(\theta)$, the spherical harmonic with no $\phi$ dependence. At large distances

$$j_l(kr) \xrightarrow[r \to \infty]{} \frac{e^{i(kr - l\pi/2)} - e^{-i(kr - l\pi/2)}}{2ikr}$$

We couple $| l 0 \rangle$ and $| s m_s \rangle$ to obtain:

$$| l 0 \rangle | s m_s \rangle = \sum_{JM} (l s 0 m_s | JM) | J M l s \rangle$$

and we may write for the incident wave function:

$$\psi^{s}_{inc} \simeq \frac{i(\pi)^{1/2}}{kr}\sum_{JMl}(l s 0 m_s|JM)\, i^{l}\,(2l+1)^{1/2}$$

$$\times\left\{e^{-i(kr-l\pi/2)} - e^{+i(kr-l\pi/2)}\right\}|JMls\rangle \qquad (3\text{-}10)$$

A comparison of the ingoing parts of Eq. (3-8) and Eq. (3-10) yields:

$$A^{JM}_{ls} = \frac{i(\pi v)^{1/2}}{K}(l s 0 m_s|JM)\, i^{l}(2l+1)^{1/2} \qquad (3\text{-}11)$$

and from Eq. (3-9) that

$$B^{JM}_{l's'} = \frac{i(\pi v)^{1/2}}{K}\sum_{l}(l s 0 m_s|JM)\, i^{l}(2l+1)^{1/2}\, S^{J}_{l's',ls} \qquad (3\text{-}12)$$

where no sum over $s$ is included as the channel spin is specified for the present. Now Eq. (3-8) can be written with primes on $l$ and $s$ and using Eq. (3-11) and (3-12) we have:

$$\psi^{s'}_{TOTAL} = \frac{i(\pi)^{1/2}}{kr}\sum_{JMl'}\Big\{(l's'0m_s|JM)\, i^{l'}(2l'+1)^{1/2}\, e^{-i(kr-l'\pi/2)}$$

$$-\sum_{l}(l s 0 m_s|JM)\, i^{l}(2l+1)^{1/2}\, S^{J}_{l's',ls}\, e^{+i(kr-l'\pi/2)}\Big\}|JMl's'\rangle$$

$$(3\text{-}13)$$

Of course, the first part of Eq. (3-13) is identical with the first part of Eq. (3-10) with primes on $l$ and $s$. Therefore, adding and subtracting the following

$$\frac{i(\pi)^{1/2}}{kr}\sum_{JMl'}(l's'0m_s|JM)\, i^{l'}(2l'+1)^{1/2}\, e^{+i(kr-l'\pi/2)}\,|JMl's'\rangle$$

to Eq. (3-13) yields $\psi^{s'}_{TOTAL} = \psi^{s'}_{inc} + \psi^{s'}_{SCATT}$, or that

$$\psi^{s'}_{SCATT} = \frac{i(\pi)^{1/2}}{kr}\Big\{\sum_{JMl'}(l's'0m_s|JM)\, i^{l'}(2l'+1)^{1/2} e^{+i(kr-l'\pi/2)}$$

$$\times|JMl's'\rangle - \sum_{JMll'}(ls0M_s|JM)\, i^{l}(2l+1)^{1/2} S^{J}_{l's',ls}$$

$$\times e^{+i(kr-l'\pi/2)}|JMl's'\rangle\Big\}$$

or

$$\psi^{s'}_{SCATT} = \frac{i(\pi)^{1/2}}{kr}\sum_{JMll'}(ls0M_s|JM)\, i^{l}(2l+1)^{1/2}(\delta_{ll'}\delta_{ss'} - S^{J}_{l's',ls})\, e^{+i(kr-l'\pi/2)}|JMl's'\rangle \qquad (3\text{-}14)$$

Decomposing $|JMl's'\rangle$ gives:

$$|JMl's'\rangle = \sum_{m_{l'}m_{s'}}(l's'm_{l'}m_{s'}|JM)\,|l'm_{l'}\rangle|s'm_{s'}\rangle \qquad (3\text{-}15)$$

Using Eq. (3-15) and the fact that $e^{-il'\pi/2} = i^{-l'}$, Eq. (3-14) yields:

$$\psi^{s'}_{SCATT} = \frac{i}{k}\frac{e^{ikr}}{r}\sum_{m_{s'}} f^{s'm_{s'},sm_s}(\theta,\phi)\,|s'm_{s'}\rangle \qquad (3\text{-}16)$$

where $f^{s'm_{s'},sm_s}(\theta,\phi)$ is the form or scattering factor. We are interested in the differential cross section for the process $s,m_s \rightarrow s',m_{s'}$ i.e., for the process from entrance channel $s, m_s$ to exit channel $s', m_{s'}$. The differential cross section can be represented for this scattering process as

$$d\sigma_{s'm_{s'},sm_s} = \bar{\lambda}^2\,|f^{s'm_{s'},sm_s}(\theta,\phi)|^2\,d\Omega \qquad (3\text{-}17)$$

where $\lambda\!\!\!^{-} = 1/k$ is the de Broglie wave length divided by $2\pi$ and the form factor or scattering factor, $f^{\mathcal{S}'m_{\mathcal{S}'},\mathcal{S}m_{\mathcal{S}}}_{(\theta,\phi)}$ is given by:

$$f^{\mathcal{S}'m_{\mathcal{S}'},\mathcal{S}m_{\mathcal{S}}}(\theta,\phi) = \sum_{JMll'm_{l'}} i^{l-l'}(\pi)^{1/2}(l\mathcal{S}0m_{\mathcal{S}}|JM)$$

$$\times\ (l'\mathcal{S}'m_{l'}m_{\mathcal{S}'}|JM)(\delta_{ll'}\delta_{\mathcal{S}\mathcal{S}'} - S^{J}_{l'\mathcal{S}',l\mathcal{S}})|l'm_{l'}\rangle \qquad (3\text{-}18)$$

where $|l'm_{l'}\rangle = Y_{l'm_{l'}}(\theta,\phi)$. Up to this point, the spin projections $m_{\mathcal{S}}, m_{\mathcal{S}'}$ have been specified, hence the dependence of $f(\theta,\phi)$ on $\phi$. For an unpolarized beam we may average over the incident spin projections, $m_{\mathcal{S}}$, and sum over the final spin projections, $m_{\mathcal{S}'}$, to get:

$$d\sigma_{\mathcal{S}'\mathcal{S}} = \frac{1}{2\mathcal{S}+1}\sum_{m_{\mathcal{S}}m_{\mathcal{S}'}} d\sigma_{\mathcal{S}'m_{\mathcal{S}'},\mathcal{S}m_{\mathcal{S}}} \qquad (3\text{-}19)$$

Finally, the differential cross section independent of channel spin $\mathcal{S}$ (or $\mathcal{S}'$) is obtained by averaging over the possible values of $\mathcal{S}$ and summing over the possible values of $\mathcal{S}'$, i.e.,

$$d\sigma = \sum_{\mathcal{S}\mathcal{S}'}\frac{(2\mathcal{S}+1)}{(2I+1)(2s+1)}\, d\sigma_{\mathcal{S}'\mathcal{S}} \qquad (3\text{-}20)$$

Eq. (3-17) together with Eqs. (3-18), (3-19), and (3-20) gives the final relation between the scattering matrix in L-S coupling and the differential cross section. The counterpart to this relation is derived in Appendix 5 for j-j coupling.

Blatt and Biedenharn (Bl 52) have simplified Eq. (3-19) in that they have carried out the evaluation of Eq. (3-19) with the following results as they apply to elastic neutron scattering:

$$d\sigma_{s's} = \frac{\bar{\lambda}^{2}}{2s+1} \sum_{L=0}^{\infty} B_L(s',s)\, P_L(\cos\theta)\, d\Omega \qquad (3\text{-}21)$$

where

$$B_L(s',s) = \frac{(-)^{s'-s}}{4} \sum_{J_1 J_2 l_1 l_2 l_1' l_2'} \bar{Z}(l_1 J_1 l_2 J_2, sL)\, \bar{Z}(l_1' J_1 l_2' J_2, s'L)$$

$$\times \text{R.P.} \left\{ \left( \delta_{l_1' l_1} \delta_{s's} - S^{J_1}_{l_1' s', l_1 s} \right)^{*} \left( \delta_{l_2' l_2} \delta_{s's} - S^{J_2}_{l_2' s', l_2 s} \right) \right\} \qquad (3\text{-}22)$$

The $P_L(\cos\theta)$ are Legendre polynomials and R.P. stands for the real part of the expression in brackets. It is important to note that the Eq. (4.6) of Blatt and Biedenharn is incorrect in the definition of the Z coefficients. The correct expression for the Z coefficients is as follows (La 58):

$$\bar{Z}(l_1 J_1 l_2 J_2, sL) = \left\{ (2l_1+1)(2l_2+1)(2J_1+1)(2J_2+1) \right\}^{1/2}$$

$$\times W(l_1 J_1 l_2 J_2, sL)\,(l_1 l_2 0 0 | L 0) \qquad (3\text{-}23)$$

where $W(l_1 J_1 l_2 J_2, sL)$ is the Racah coefficient as defined in reference Ra 42. These Z coefficients, as stated in Eq. (3-23) are usually referred to as z-bar coefficients ( $\bar{Z}$ ) and differ from the Z coefficients of Blatt and Biedenharn by a factor $i^{l_1 - l_2 - L}$.

As discussed in Chapter 2, the measured differential cross sections are expanded in a series of Legendre polynomials,

$$\sigma_{MEAS}(\theta, ENO) = \sum_{L=0}^{4} B_L(ENO)\, P_L(\cos\theta)$$

To make the calculated Legendre expansion coefficients consistent with the experimentally fitted Legendre expansion coefficients we redefine the Eq. (3-22) of Blatt and Biedenharn (above) as follows using Eqs. (3-22), (3-21), and (3-20):

$$d\sigma = \sum_{ss'} \frac{(2s+1)}{(2I+1)(2s+1)} \times \frac{\bar{\lambda}^2}{(2s+1)} \sum_{L=0}^{\infty} \frac{(-)^{s'-s}}{4} \sum_{J_1 J_2 l_1 l_2 l_1' l_2'} \bar{Z}(l_1 J_1 l_2 J_2, sL)$$

$$\times\, \bar{Z}(l_1' J_1 l_2' J_2, s'L) \times \mathrm{R.P.} \left\{ \left( \delta_{l_1' l_1} \delta_{s's} - S^{J_1}_{l_1' s', l_1 s} \right)^* \right.$$

$$\left. \times \left( \delta_{l_2' l_2} \delta_{s's} - S^{J_2}_{l_2' s', l_2 s} \right) \right\} P_L(\cos\theta)\, d\Omega$$

or

$$\sigma_{CALCULATED}(\theta, ENO) = \sum_{L=0}^{4} B_L(ENO)\, P_L(\cos\theta)$$

where

$$B_L(ENO) = \frac{\bar{\lambda}^2}{(2I+1)(2S+1)} \sum_{ss' J_1 J_2 l_1 l_2 l_1' l_2'} \frac{(-)^{s'-s}}{4} \bar{Z}(l_1 J_1 l_2 J_2, sL)$$

$$\times\, \bar{Z}(l_1' J_1 l_2' J_2, s'L) \times \mathrm{R.P.} \left\{ \left( \delta_{l_1' l_1} \delta_{s's} - S^{J_1}_{l_1' s', l_1 s} \right)^* \left( \delta_{l_2' l_2} \delta_{s's} - S^{J_2}_{l_2' s', l_2 s} \right) \right\}$$

(3-24)

Eq. (3-24) represents the final working expression for the Legendre expansion coefficients calculated from elements of the scattering matrix. It is this expression which was utilized in the Ohio R-matrix Analysis Program, ORMAP, described in Section 3.3.

### 3.1.3 Transformation of the Scattering Matrix

Since the study of different nuclei via the R-matrix theory may include different coupling schemes, it is desirable to be able to form the R-matrix in either the j-j or L-S coupling scheme. We have the necessary relations to obtain the cross section from the scattering matrix in L-S coupling so all that remains is to develop the transformation which will transform elements of the scattering matrix in j-j coupling to the corresponding elements in L-S coupling (Mo 76). We seek the transformation:

$$S^{J}_{\ell' j', \ell j} \Longrightarrow S^{J}_{\ell' \mathcal{S}', \ell \mathcal{S}}$$

where $S^{J}_{\ell' j', \ell j}$ is defined in Appendix 5. We can write for elastic scattering the total wave functions in L-S and j-j coupling as follows:

$$\psi^{L\text{-}S}_{(\ell s I J M)} \sim \mathcal{I}[\ell(sI)\mathcal{S}, JM] - \sum_{\ell' \mathcal{S}'} S^{J}_{\ell' \mathcal{S}', \ell \mathcal{S}} \, \mathcal{O}[\ell'(sI)\mathcal{S}', JM] \tag{3-25}$$

$$\psi^{j\text{-}j}_{(\ell s I J M)} \sim \mathcal{I}[(\ell s) j I, JM] - \sum_{\ell' j'} S^{J}_{\ell' j', \ell j} \, \mathcal{O}[(\ell' s) j' I, JM] \tag{3-26}$$

where $\mathcal{I}$ represents an ingoing wave, $\mathcal{O}$ represents an outgoing wave, and $S^J$ represents the scattering matrix. We want to find $S^J_{\ell'\mathscr{s}',\ell\mathscr{s}}$ in terms of $S^J_{\ell'j',\ell j}$. Consider three angular momenta and their total; $j_1$, $j_2$, $j_3$, and $j_{TOT}$ and let $j' = j_1 + j_2$ and $j'' = j_2 + j_3$. Then we may write (Ro 57):

$$\Psi_{j_{TOT},M}(j') = \sum_{j''} R_{j''j'} \Psi_{j_{TOT},M}(j'') \qquad (3\text{-}27)$$

where

$$R_{j''j} = (2j''+1)^{1/2}(2j'+1)^{1/2} W(j_1 j_2 j_{TOT} j_3, j'j'') \qquad (3\text{-}28)$$

and $W(j_1 j_2 j_{TOT} j_3, j'j'')$ are Racah coefficients (Ra 42). If we make the following correspondences:

$$\overset{j_1}{\vec{\ell}} + \overset{j_2}{\vec{S}} \longrightarrow \overset{j'}{\vec{j}} + \overset{j_3}{\vec{I}} \longrightarrow \overset{j_{TOT}}{\vec{J}}$$

$$\overset{j_2}{\vec{S}} + \overset{j_3}{\vec{I}} \longrightarrow \overset{j''}{\vec{\mathscr{s}}} + \overset{j_1}{\vec{\ell}} \longrightarrow \overset{j_{TOT}}{\vec{J}}$$

we can write:

$$\mathscr{I}[(\ell s)jI, JM] = \sum_{\mathscr{s}} \mathscr{I}[\ell(sI)\mathscr{s}, JM]\, R(\ell s J I, j\mathscr{s}) \qquad (3\text{-}29)$$

and similarly:

$$O[(\ell' s)j'I, JM] = \sum_{\mathscr{s}'} O[\ell'(sI)\mathscr{s}', JM]\, R(\ell' s J I, j'\mathscr{s}') \qquad (3\text{-}30)$$

Substituting Eqs. (3-29) and (3-30) into Eq. (3-26) yields:

2

$$\psi^{j-j}_{(\ell sIJM)} \sim \sum_{\mathscr{s}} \mathcal{I}[\ell(sI)\mathscr{s}, JM]\, R(\ell sJI, j\mathscr{s})$$

$$-\sum_{\ell' j'} S^{J}_{\ell' j', \ell j} \sum_{\mathscr{s}'} O[\ell'(sI)\mathscr{s}', JM]\, R(\ell' sJI, j'\mathscr{s}') \quad (3\text{-}31)$$

Since R is unitary it can be shown (Ro 57) that:

$$\sum_{e} R_{ef} R_{eg} = \delta_{fg} \quad \text{i.e.,}$$

$$\sum_{j} R(\ell sJI, j\mathscr{s})\, R(\ell sJI, j\mathscr{s}'') = \delta_{\mathscr{s}\mathscr{s}''} \quad (3\text{-}32)$$

Using Eq. (3-32) on Eq. (3-31) we obtain:

$$\psi^{\ell-\mathscr{s}''}_{(\ell sIJM)} \sim \sum_{j} R(\ell sJI, j\mathscr{s}'')\, \psi^{j-j}_{(\ell sIJM)} = \sum_{\mathscr{s}} \mathcal{I}[\ell(sI)\mathscr{s}, JM]\, \delta_{\mathscr{s}\mathscr{s}''}$$

$$-\sum_{\ell' j'} S^{J}_{\ell' j', \ell j} \sum_{\mathscr{s}' j} R(\ell' sJI, j'\mathscr{s}')\, O[\ell'(sI)\mathscr{s}', JM]\, R(\ell sJI, j\mathscr{s}'') \quad (3\text{-}33)$$

If Eq. (3-33) is compared with Eq. (3-25) we find that

$$S^{J}_{\ell'\mathscr{s}', \ell\mathscr{s}} = \sum_{jj'} R(\ell sJI, j\mathscr{s})\, S^{J}_{\ell' j', \ell j}\, R(\ell' sJI, j'\mathscr{s}') \quad (3\text{-}34)$$

Eq. (3-34) is the transformation we seek. It is the expression which was utilized in the R-matrix program ORMAP, described in Section 3.3, to transform j-j coupled elements of the scattering matrix to the corresponding L-S coupled elements.

## 3.2 R-Matrix Theory Formulation

The R-matrix theory is a way of parameterizing so that the energy dependence of the scattering matrix can be calculated. It makes the approximation that many quantities are energy independent, e.g., $\gamma^2$, $R_o$, and b, all of which are explained in the next section. It is most easily applied to resonances which are distinct and well spaced in energy, but also, as this paper will demonstrate, useful in obtaining nuclear structure information where the compound spectra are fairly complicated. The R-matrix theory involves, essentially, a reparameterization of the elements of the scattering matrix. While the elements of the scattering matrix have a less direct physical meaning, the elements of the R-matrix are, in principle, more directly related to nuclear properties obtainable from experiment, e.g., the energies and widths of the states, etc. The following discussion of the R-matrix theory is separated into two parts: 1) the derivation of the R-matrix and 2) the connection between the R-matrix and the scattering matrix. While there are numerous erudite articles in the literature on R-matrix theory (La 58, Vo 59, Vo 62, Wi 63), the details are carried out here, in a hopefully consistent, readable manner which may serve as a practical guide for future experimentalists in neutron scattering experiments.

### 3.2.1 Derivation of the R-Matrix Relation

In the R-matrix theory of nuclear reactions we consider two regions: the "internal" region where the nuclear potential is non-zero and the "external" region where the potential is zero. We consider these two regions to be separated by a definite boundary. Let us consider a wave function $\Psi_{INT}$ in the "internal" region, i.e., a wave function describing a number of nucleons in the volume $\tau$. Then:

$$H \Psi_{INT} = E \Psi_{INT} \qquad (3\text{-}35)$$

We may expand this wave function $\Psi_{INT}$ in terms of some internal orthogonal set, $X_\lambda$, where $X_\lambda$ satisfies the same Hamiltonian as $\Psi_{INT}$ and orthogonality is assured by the appropriate choice of boundary condition, i.e.,

$$H X_\lambda = E_\lambda X_\lambda \qquad (3\text{-}36)$$

$$\frac{r_c}{X_\lambda} \frac{d X_\lambda}{d r_c} \bigg|_{r_c = a_c} = b_c \qquad (3\text{-}37)$$

Then from Eq. (3-36) and Eq. (3-37) we have that:

$$\int_\tau X_\lambda^* X_{\lambda'} \, d\tau = \delta_{\lambda\lambda'} \qquad (3\text{-}38)$$

where $\tau$ is the volume of the internal region. We can expand $\Psi_{INT}$ as follows:

$$\Psi_{INT} = \sum_\lambda C_\lambda X_\lambda \qquad (3\text{-}39)$$

where:

$$C_\lambda = \int_\tau \Psi_{INT} X_\lambda^* \, d\tau \qquad (3\text{-}40)$$

We may proceed to solve for the $C_\lambda$ as follows:

$$X_\lambda^* \left( H \Psi_{INT} = E \Psi_{INT} \right) \qquad (3\text{-}41a)$$

$$\Psi_{INT} \left( H X_\lambda^* = E_\lambda X_\lambda^* \right) \qquad (3\text{-}41b)$$

Subtracting and integrating these two equations over the internal region yields:

$$\int_\tau \left( \Psi_{INT} H X_\lambda^* - X_\lambda^* H \Psi_{INT} \right) d\tau = (E_\lambda - E) \int_\tau \Psi_{INT} X_\lambda^* \, d\tau \qquad (3\text{-}42a)$$

From Eq. (3-40) we see that:

$$C_\lambda = (E_\lambda - E)^{-1} \int_\tau \left( \Psi_{INT} H X_\lambda^* - X_\lambda^* H \Psi_{INT} \right) d\tau \qquad (3\text{-}42b)$$

We assume that:

$$\int_\tau \left( \Psi_{INT} V X_\lambda^* - X_\lambda^* V \Psi_{INT} \right) d\tau = 0$$

We integrate Eq. (3-42b) by parts (Green's Theorem) to get:

$$C_\lambda = (E_\lambda - E)^{-1} \int_S \frac{\hbar^2}{2M_c} \left( X_\lambda^* \nabla_n \Psi_{INT} - \Psi_{INT} \nabla_n X_\lambda^* \right) dS \qquad (3\text{-}43)$$

where the integral S is over the surface of the internal region. The problem is now to find expressions for $\nabla_n \Psi_{INT}$ and $\Psi_{INT}$ <u>on the surface</u> (i.e., boundary between the internal and external regions). We write for $\Psi$ in the external region:

$$\Psi_{EXT} = \sum_c u_c \phi_c \qquad (3\text{-}44)$$

where: $\Phi_c$ = channel wave function, i.e., contains all quantum numbers, etc. other than radial function, and also the factor 1/r,

$u_c$ = radial part of the wave function.

If we consider a surface in configuration space made up of the intersection of incoming and outgoing channels, as seen in the two-dimensional diagram below,

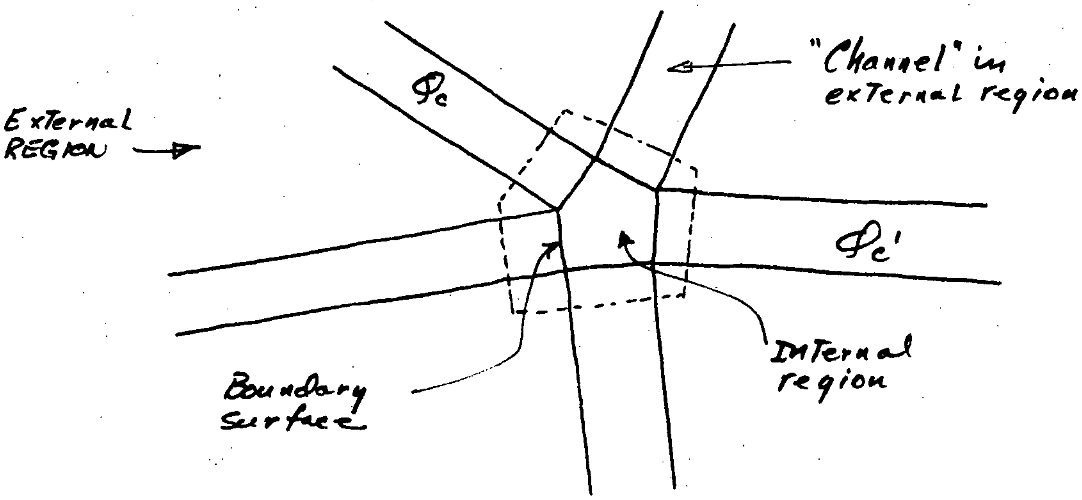

we see that the $\Phi_c$'s are orthogonal IF we pick a boundary surface equal to or larger than the surface formed by the intersection of the incoming and outgoing channels. That is, the overlap $\int_S \Phi_c^* \Phi_{c'} \, dS$ will be zero, or

$$\int_S \Phi_c^* \Phi_{c'} \, dS = \delta_{cc'} \tag{3-45}$$

Since the $\Phi_c$'s form a complete set of functions on a boundary surface equal to or larger than the surface formed by the intersection of the various channels we may use this set to find expansions for $\nabla_n \Psi_{ext}$ and $\Psi_{ext}$ on the surface. We define the following "value" and "derivative" quantities respectively:

$$V_c \equiv \left(\frac{\hbar^2}{2m_c a_c}\right)^{1/2} u_c(a_c) \qquad (3\text{-}46a)$$

$$D_c \equiv \left(\frac{\hbar^2}{2m_c a_c}\right)^{1/2} r_c \frac{du_c(r_c)}{dr_c}\bigg|_{r_c=a_c} \qquad (3\text{-}46b)$$

where $a_c$ is the value of $r_c$ at the channel surface. These equations may be written in integral form as follows:

$$V_c = \left(\frac{\hbar^2}{2m_c a_c}\right)^{1/2} \int_S \varphi_c^* \Psi_{ext}\, dS \qquad (3\text{-}47a)$$

and

$$D_c = \left(\frac{a_c \hbar^2}{2m_c}\right)^{1/2} \int_S \varphi_c^* \nabla_n (r_c \Psi_{ext})\, dS \qquad (3\text{-}47b)$$

where $\Psi_{ext} = \sum_c u_c \varphi_c$ (<u>on the surface</u>) may be used to show equivalence with Eq. (3-46a) and Eq. (3-46b). Now $\Psi_{ext}$ and $\nabla_n \Psi_{ext}$ may be obtained from Eq. (3-46a) and Eq. (3-46b) as follows:

$$\Psi_{ext}\Big|_{r_c=a_c} = \sum_c u_c \varphi_c\Big|_{r_c=a_c} = \sum_c \left(\frac{2m_c a_c}{\hbar^2}\right)^{1/2} V_c \varphi_c \qquad (3\text{-}48a)$$

$$\nabla_n(r_c \Psi_{ext})\Big|_{r_c=a_c} = \Psi_{ext}\Big|_{r_c=a_c} + a_c \nabla_n \Psi_{ext}\Big|_{r_c=a_c} = \sum_c \frac{du_c}{dr_c}\Big|_{r_c=a_c}(a_c \varphi_c) \quad \underline{\underline{OR}}$$

$$\nabla_n(\Psi_{ext})\Big|_{r_c=a_c} = \sum_c \left(\frac{2m_c}{a_c \hbar^2}\right)^{1/2} (D_c - V_c)\varphi_c \qquad (3\text{-}48b)$$

Recall: $\Psi_{ext}\Big|_{r_c=a_c} = \Psi_{INT}\Big|_{r_c=a_c}$ and $\nabla_n \Psi_{ext}\Big|_{r_c=a_c} = \nabla_n \Psi_{INT}\Big|_{r_c=a_c}$ (3-49)

Equations (3-48a) and (3-48b) substituted into Eq. (3-43) yield:

$$C_\lambda = (E_\lambda - E)^{-1} \sum_c (D_c V_{\lambda c}^* - V_c D_{\lambda c}^*) \qquad (3\text{-}50)$$

where $V_{\lambda c}^*$ and $D_{\lambda c}^*$ are defined for $X_\lambda^*$ similarly to Eq. (3-47a) and Eq. (3-47b). Equation (3-50) is exact when the boundary surface is equal to or larger than the surface formed by the intersection of the various ingoing and outgoing channels. Recall from Eq. (3-36) that we had for the orthogonal internal states:

$$H X_\lambda = E_\lambda X_\lambda$$

where:

$$\int_\tau X_\lambda^* X_\lambda \, d\tau = \delta_{\lambda\lambda'}$$

From the general boundary condition (Eq. (3-37)):

$$\left(\frac{r_c}{X_\lambda^*}\frac{dX_\lambda^*}{dr_c}\right|_{r_c=a_c} = b_c \quad \underline{\underline{\text{OR}}} \quad \frac{D_{\lambda c}^*}{V_{\lambda c}^*}\left(\equiv \frac{\delta_{\lambda c}}{\gamma_{\lambda c}}\right) = b_c \qquad (3\text{-}51)$$

Eq. (3-50) becomes:

$$\begin{aligned} C_\lambda &= (E_\lambda - E)^{-1} \sum_c V_{\lambda c}^* (D_c - b_c V_c) \\ &= (E_\lambda - E)^{-1} \sum_c \gamma_{\lambda c} D_c^0 \qquad (3\text{-}52) \end{aligned}$$

where:

$$D_c^0 = D_c - b_c V_c$$

Using this value for $C_\lambda$ in Eq. (3-39) we have:

$$\Psi_{INT} = \sum_c \left[ \sum_\lambda \frac{X_\lambda \gamma_{\lambda c}}{E_\lambda - E} \right] D_c^0 \qquad (3\text{-}53)$$

This equation relates the value of $\Psi_{INT}$ at any point in the volume $\tau$ to its "derivatives" (actually derivative and value) on the surface S. Operating on Eq. (3-53) with

$$\left(\frac{\hbar^2}{2M_{c'}a_{c'}}\right)^{1/2}\int_S \phi_{c'}^* \, dS$$

yields:

$$\left(\frac{\hbar^2}{2M_{c'}a_{c'}}\right)^{1/2}\int_S \Psi_{INT}\,\phi_{c'}^* \, dS = \sum_c \int_S \sum_\lambda \left(\frac{X_\lambda \gamma_{\lambda c}}{E_\lambda - E}\right) D_c^0 \left(\frac{\hbar^2}{2M_{c'}a_{c'}}\right)^{1/2} \phi_{c'}^* \, dS \tag{3-54}$$

Using Eq. (3-47a) in Eq. (3-54) we obtain:

$$V_{c'} = \sum_c R_{c'c} D_c^0 \tag{3-55}$$

where:

$$R_{c'c} = \sum_\lambda \frac{\gamma_{\lambda c'}\gamma_{\lambda c}}{E_\lambda - E} \tag{3-56}$$

Equation (3-55) defines the fundamental R-matrix relation, i.e., the value in any channel is related to the derivative quantity $D_c^0$ in all channels. We may write Eqs. (3-55) and (3-56) in matrix notation as follows:

$$\mathbb{V} = \mathbb{R}\,\mathbb{D}^0 \tag{3-57}$$

where:

$$\mathbb{R} = \sum_\lambda \frac{(\gamma_\lambda \times \gamma_\lambda)}{E_\lambda - E} \tag{3-58}$$

### 3.2.2 Relation Between the R-Matrix and Scattering Matrix

We have, from Eq. (3-55), defined the fundamental R-Matrix relation and have further given (Eq. (3-56)) an expression for R in terms of various "internal" parameters ( $\gamma_{\lambda c}$ and $E_\lambda$ ). The problem is now to develop a relation between the scattering matrix and the R-matrix. For an external wave function, in general, we can write (from Eq. (3-8)):

$$\Psi = \sum_c V_c^{-1/2} (A_c I_c - B_c O_c) r^{-1} |JM\ell s\rangle \tag{3-59}$$

where:

$$B_{c'} = \sum_c S_{c'c} A_c \quad \underline{\underline{\text{OR}}} \quad \mathbb{B} = \mathcal{S}\mathbb{A} \tag{3-60}$$

From Eq. (3-55) we have:

$$V_{c'} = \sum_c R_{c'c} D_c^\circ$$

The "value" and "derivative" quantities for the external wave functions can be written as follows:

$$V_c = \left(\frac{\hbar^2}{2m_c a_c}\right)^{1/2} \frac{1}{V^{1/2}} u(\rho_c)\Big|_{r_c=a_c} = \left(\frac{\hbar^2}{2}\right)^{1/2} \rho_c^{-1/2} u_c(\rho_c)\Big|_{r_c=a_c} \tag{3-61a}$$

$$D_c = \left(\frac{\hbar^2}{2m_c a_c}\right)^{1/2} \frac{1}{V^{1/2}} \rho_c \frac{du}{d\rho_c}\Big|_{r_c=a_c} = \left(\frac{\hbar^2}{2}\right) \rho_c^{+1/2} \frac{d\,u(\rho_c)}{d\rho_c}\Big|_{r_c=a_c} \tag{3-61b}$$

where $\rho_c = k r_c$

Using Eq. (3-59) in Eqs. (3-61a) and (3-61b) and substituting into Eq. (3-57) we have (in matrix form):

$$\rho^{-1/2}(\mathbb{I}\mathbb{A}-\mathbb{O}\mathbb{B})=\mathbb{R}\left\{\rho^{+1/2}(\mathbb{I}'\mathbb{A}-\mathbb{O}'\mathbb{B})-\mathbb{b}\rho^{-1/2}(\mathbb{I}\mathbb{A}-\mathbb{O}\mathbb{B})\right\} \tag{3-62}$$

Rearranging and factoring Eq. (3-62) gives:

$$(\mathbb{O}\rho^{-1/2}-\mathbb{R}\mathbb{O}'\rho^{1/2}+\mathbb{R}\mathbb{b}\mathbb{O}\rho^{-1/2})\mathbb{B}=(\mathbb{I}\rho^{-1/2}-\mathbb{R}\mathbb{I}'\rho^{-1/2}+\mathbb{R}\mathbb{b}\mathbb{I}\rho^{-1/2})\mathbb{A} \tag{3-63}$$

$$\mathbb{O}\rho^{-1/2}(\mathbb{1}-\mathbb{R}(\rho\mathbb{O}'\mathbb{O}^{-1}-\mathbb{b}))\mathbb{B}=\mathbb{I}\rho^{-1/2}(\mathbb{1}-\mathbb{R}(\rho\mathbb{I}'\mathbb{I}^{-1}-\mathbb{b}))\mathbb{A} \tag{3-64}$$

Let:

$$\mathbb{L}=\rho\mathbb{O}'\mathbb{O}^{-1}=\mathcal{S}+i\mathbb{P} \tag{3-65a}$$

$$\mathbb{L}^{*}=\rho\mathbb{I}'\mathbb{I}^{-1}=\mathcal{S}-i\mathbb{P} \tag{3-65b}$$

and

$$\mathbb{L}^{0}=\mathbb{L}-\mathbb{b}\ \left(=(\mathcal{S}-\mathbb{b})+i\mathbb{P}\right) \tag{3-66a}$$

$$\mathbb{L}^{0*}=\mathbb{L}^{*}-\mathbb{b}\ \left(=(\mathcal{S}-\mathbb{b})-i\mathbb{P}\right) \tag{3-66b}$$

where $\mathcal{S}$ is the shift factor and $\mathbb{P}$ the penetration factor. The diagonal matrix $\mathbb{b}$ is the boundary condition from Eq. (3-37). Then we may write for Eq. (3-64):

$$\mathbb{B}=\rho^{+1/2}\mathbb{O}^{-1}(\mathbb{1}-\mathbb{R}\mathbb{L}^{0})^{-1}(\mathbb{1}-\mathbb{R}\mathbb{L}^{0*})\mathbb{I}\rho^{-1/2}\mathbb{A} \tag{3-67}$$

If we compare Eq. (3-67) with Eq. (3-60) we find that:

$$\mathbb{S}=\rho^{+1/2}\mathbb{O}^{-1}(\mathbb{1}-\mathbb{R}\mathbb{L}^{0})^{-1}(\mathbb{1}-\mathbb{R}\mathbb{L}^{0*})\mathbb{I}\rho^{-1/2} \tag{3-68}$$

Equation (3-68) gives the required connection between the R-matrix as given in Eq. (3-58) and the scattering matrix as defined in Eq. (3-9). We define

$$\Omega_c \equiv (I_c / O_c)^{1/2}_{r_c = a_c} \qquad (3\text{-}69)$$

As can be seen in Appendix 6:

$$P_c = (\rho_c / I_c O_c)_{r_c = a_c} \qquad (3\text{-}70)$$

$$\omega = (O_c' I_c - I_c' O_c)_{r_c = a_c} = 2i \qquad (3\text{-}71)$$

Then:

$$\Omega_c P_c^{1/2} = \left( \frac{I_c}{O_c} \cdot \frac{\rho_c}{I_c O_c} \right)^{1/2} = \rho_c^{1/2} O_c^{-1} \qquad (3\text{-}72)$$

$$P_c^{-1/2} \Omega_c = \left( \frac{I_c O_c}{\rho_c} \cdot \frac{I_c}{O_c} \right)^{1/2} = I_c \rho_c^{-1/2} \qquad (3\text{-}73)$$

and we can write:

$$\mathbb{S}^{J\pi} = \mathbf{\Omega} \mathbb{P}^{1/2} (\mathbb{1} - \mathbb{R}^{J\pi} \mathbb{L}^{0} ]^{-1} (\mathbb{1} - \mathbb{R}^{J\pi} \mathbb{L}^{0*}) \mathbb{P}^{-1/2} \mathbf{\Omega} \qquad (3\text{-}74)$$

$$\boxed{\mathbb{S}^{J\pi} = \mathbf{\Omega} (\mathbb{1} + 2i \mathbb{P}^{1/2} (\mathbb{1} - \mathbb{R}^{J\pi} \mathbb{L}^{0} ]^{-1} \mathbb{R}^{J\pi} \mathbb{P}^{1/2}) \mathbf{\Omega}} \qquad (3\text{-}75)$$

The values for the scalar matrices $\mathbf{\Omega}$, $\mathbb{P}$, and $\mathbb{L}^{0}$ are derived and summarized in Appendix 6.

## 3.3 The Computer Program ORMAP

The Ohio (University) R-Matrix Analysis Program, ORMAP, was written for this experiment and programmed on the Laboratory's IBM 1800 computer. It is a multichannel, multilevel program which, for the analysis of data in this experiment, utilized three channels and up to five levels of the same total angular momentum and parity ($J^{\pi}$). The program takes as input information the J and $\pi$ of resonances, the number of levels (of a given $J^{\pi}$) with corresponding level energies $E_{\lambda}$, the number of channels, values of orbital, channel spin, and intermediate j (j-j coupling) angular momentum in those channels, the appropriate reduced widths, boundary conditions, and background (or $R_{o\,c'c}^{J\pi}$) terms. The program utilizes a format-free assembler-read routine with a sophisticated analysis of the input parameter cards to detect possible errors in the numerous input parameters. The program further takes as input information the Legendre expansion coefficients of the experimental differential cross sections (see Section 2.7).

The program ORMAP formulates the R-matrix from the various input parameters in accordance with Eq. (3-56),

$$R_{c'c}^{J\pi} = \left\{ \sum_{\lambda=1}^{N\leq 5} \frac{\gamma_{\lambda c'} \gamma_{\lambda c}}{E_{\lambda} - E} + R_{o\,c'c} \right\}^{J\pi} \qquad (3\text{-}76)$$

where $R_{o\,c'c}^{J\pi}$ is the so-called background term, i.e., the contributions to the cross section of resonance states far removed from the region of interest. $R_{o\,c'c}^{J\pi}$ may be written as:

$$R_{o\,c'c}^{J\pi} = \sum_{\lambda=N+1}^{\infty} \frac{\gamma_{\lambda c'} \gamma_{\lambda c}}{E_{\lambda} - E} \simeq \text{CONSTANT}$$

We will see that $R_{o\,c'c}^{J\pi}$ = constant is a reasonable assumption for the experimental data over a wide range of energies.

Once the R-matrix is formed, the scattering matrix is calculated via Eq. (3-75),

$$\mathbb{S}^{J\pi} = \Omega\left(\mathbb{1} + 2i\,\mathbb{P}^{1/2}\left(\mathbb{1} - \mathbb{R}^{J\pi}\mathbb{L}^{\circ}\right)^{-1}\mathbb{R}^{J\pi}\mathbb{P}^{1/2}\right)\Omega$$

The R-matrix was formed with parameters in j-j coupling in this analysis. Therefore, when the scattering matrix is calculated, its elements are in j-j coupling and must be transformed to L-S coupling. This is accomplished via Eq. (3-34),

$$S^{J\pi}_{l's',ls} = \sum_{jj'} R(lsJI,js)\,S^{J\pi}_{l'j',lj}\,R(l'sJI,j's')$$

and in the program by the transformation subroutine. If the user specifies j-j coupling, the program uses Eq. (3-34) to transform the scattering matrix to L-S coupling before proceeding to the calculation of the Legendre coefficients. Of course, if the user specifies L-S coupling, no transformation is required.

The final step in the calculation involves Eq. (3-24),

$$B_L(ENO) = \frac{\bar{\lambda}^2}{(2I+1)(2s+1)} \sum_{s's\,J_1J_2\,l_1l_2\,l_1'l_2'} \frac{(-)^{s'-s}}{4}\,\bar{Z}(l_1J_1l_2J_2,sL)\,\bar{Z}(l_1'J_1l_2'J_2,s'L)$$

$$\times\, R.P.\left\{\left(\delta_{l_1'l_1}\delta_{s's} - S^{J_1}_{l_1's',l_1s}\right)^{*}\left(\delta_{l_2'l_2}\delta_{s's} - S^{J_2}_{l_2's',l_2s}\right)\right\}$$

Legendre expansion coefficients $(B_L(ENO))$ were calculated from R-matrix parameters through L=4. A question might arise as to why these $B_L(ENO)$ are calculated and compared to the $B_L(ENO)$ obtained from least-squares fitting of the experimental data instead of comparing directly the experimental cross sections. The reason for this is that over the energy range from approximately 100 keV to 8 MeV neutron energy there exist roughly two hundred angular distribution measurements of from five to nine angles each. This is a significant amount of data and it is more manageable in the form of Legendre expansion coefficients. More importantly, the nuclear structure information we seek is more evident in these expansion coefficients as the partial waves contributing to particular resonances are many times evident directly by observing plots of the Legendre expansion coefficients.

The output of ORMAP is on a Calcomp plotter with optional listing of $B_l(ENO)$ coefficients. The program first plots the expansion coefficients of the experimental data and then the coefficients are calculated from the R-matrix parameters. A visual comparison between calculated and experimental results is made and R-matrix parameters are then adjusted accordingly to improve the fit to the data. The computer execution time for one energy with nine possible values of angular momentum and parity, three channels and five allowed levels per $J^\pi$ is two minutes.

Mention should be made here of the use of an IBM 1800 computer for this type of calculation. With only 13K of memory and approximately 50K of disk space available to the user, and with the 1800 computer roughly first generation equipment, considerable effort was necessarily expended to make this program fit into the computer and to be efficient. Since the laboratory's 1800 computer has no floating point hardware, all angular momenta are doubled internally such that all Racah and Clebsch-Gordan subroutines could be written using integer arithmetic. Further, Eq. (3-24) was summed over channels instead of individual quantum numbers, reducing the sum over eight quantum numbers to a sum over six channel indices. This same technique was employed in Eq. (3-34), the transformation equation, and thereby provided the most efficient scheme for the extremely large number of calculations implied by Eqs. (3-24) and (3-34). While a much larger, faster, and newer generation computer is definitely more suited to this type of calculation, the results considered in Section 3.5 demonstrate what can be accomplished on difficult spectra with a smaller and slower computer and some clever programming.

## 3.4 Results of R-matrix Analysis

The R-matrix analysis program ORMAP was used to analyze the neutron elastic differential cross section data measured in this experiment as well as earlier data of Lane, *et al.* (La 70) and Nelson, *et al.* (Ne 73). Both earlier sets of data have been previously analyzed with the R-matrix using L-S coupling with certain restrictions on allowed channels, i.e., $\ell \leq 2$ and no change of $\ell$ between entrance and exit channels. The present work represents the first time data on $^{11}$B+n have been analyzed in j-j coupling and with a change allowed for the $\ell$-values between entrance and exit channels. Considering the ground state spin of $^{11}$B and the fact that experimentally only Legendre coefficients through L=4 were necessary to fit the data, thus implying the incident neutron beam contains partial waves through $\ell=2$, nine possible values of angular momentum and parity can be formed for compound states in $^{12}$B from neutron elastic scattering. Because of the large number of parameters involved in fitting the experimental data, the boundary condition in each channel was set equal to the energy average of the corresponding shift factor for each channel and was not varied. While this choice is rather arbitrary, making the boundary condition equal to zero makes the background term, $R o_{c'c}^{J\pi}$, more energy dependent (We 71). Therefore, the present choice was made in an attempt to minimize the energy dependence of $R o_{c'c}^{J\pi}$.

A considerable amount of background ($R o_{c'c}^{J\pi}$) and radius parameter variation was carried out through ORMAP before the final background terms and nuclear radius were selected. Figure 3.2 shows a plot using only the $R o_{c'c}^{J\pi}$ terms for a nuclear radius parameter of 4.5 Fermis. These values were used in the R-matrix analysis. Once this general background is established, the analysis can proceed with variations of $J^{\pi}$ assignments, level energies and level widths as discussed in the following sections.

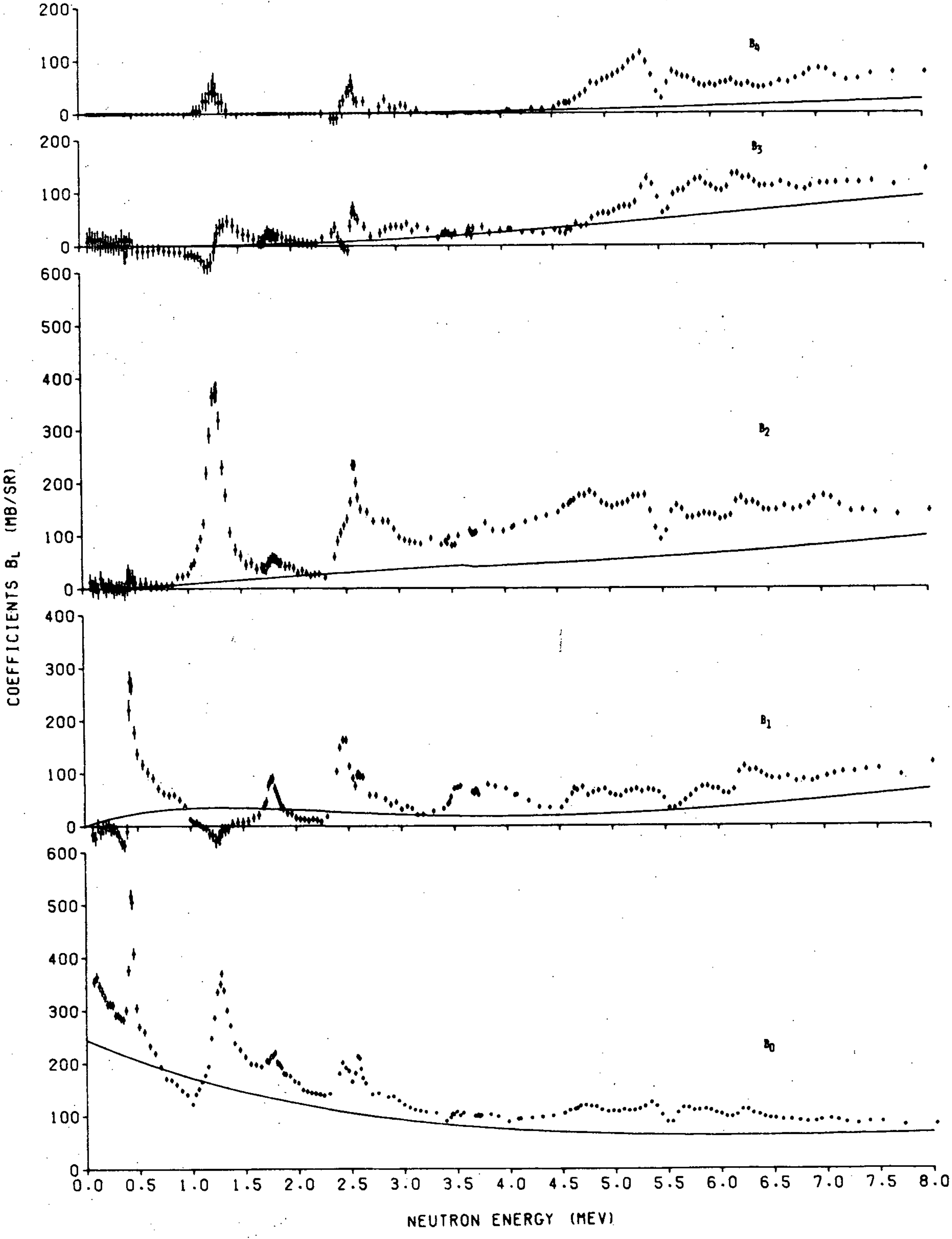

Figure 3.2 Plot of background used in R-matrix analysis vs. Legendre expansion coefficients of the experimental data.

### 3.4.1 Analysis of the Region from 0.0 MeV to 2.3 MeV

Figure 3.3 shows a plot of the R-matrix fit to the data of Lane, et al. from 0.1 MeV to 2.3 MeV neutron energy. Table 3.1 gives the possible $J^{\pi}$ combinations that can be formed from neutrons elastically scattered from $^{11}B$ with partial waves up to and including $\ell=2$ along with the various R-matrix parameters used in all the fits to data in the present work. Much of the difference from 0.0 to 0.6 MeV between this plot and that of Figure 3.2 is from the effect of two largely single-particle bound states, i.e., $1^-$ at $E_\lambda=-0.75$ MeV and $2^-$ at $E_\lambda=-1.70$ MeV. The very narrow $3^-$ ($\approx$3 eV) d-wave state at approximately 20 keV and a very narrow $1^-$ s-wave state at approximately 1.0 MeV have not been included in this fit. The $3^-$ state at 20 keV is so narrow that its effect would be negligible until the d-wave penetrability becomes larger (see Figure 3.16) and then any effect would be included in the $R_{0_{c'c}}^{J\pi}$ background term. The $1^-$ s-wave state at 1.0 MeV is narrow enough to be ignored in the study of the major structure in this region. The $2^+$ state at 0.43 MeV neutron energy is well fitted in both shape and magnitude and its previous assignment is confirmed. The broad $2^-$ state at 1.1 MeV and the $4^-$ state at 1.26 MeV neutron energy are fitted well in shape and reasonably well in magnitude. The $1^+$ state at 1.77 MeV is well fitted in shape and slightly low in magnitude in the $B_0$ and $B_2$ terms. It is likely that a readjustment of the background parameters would solve this problem. However,

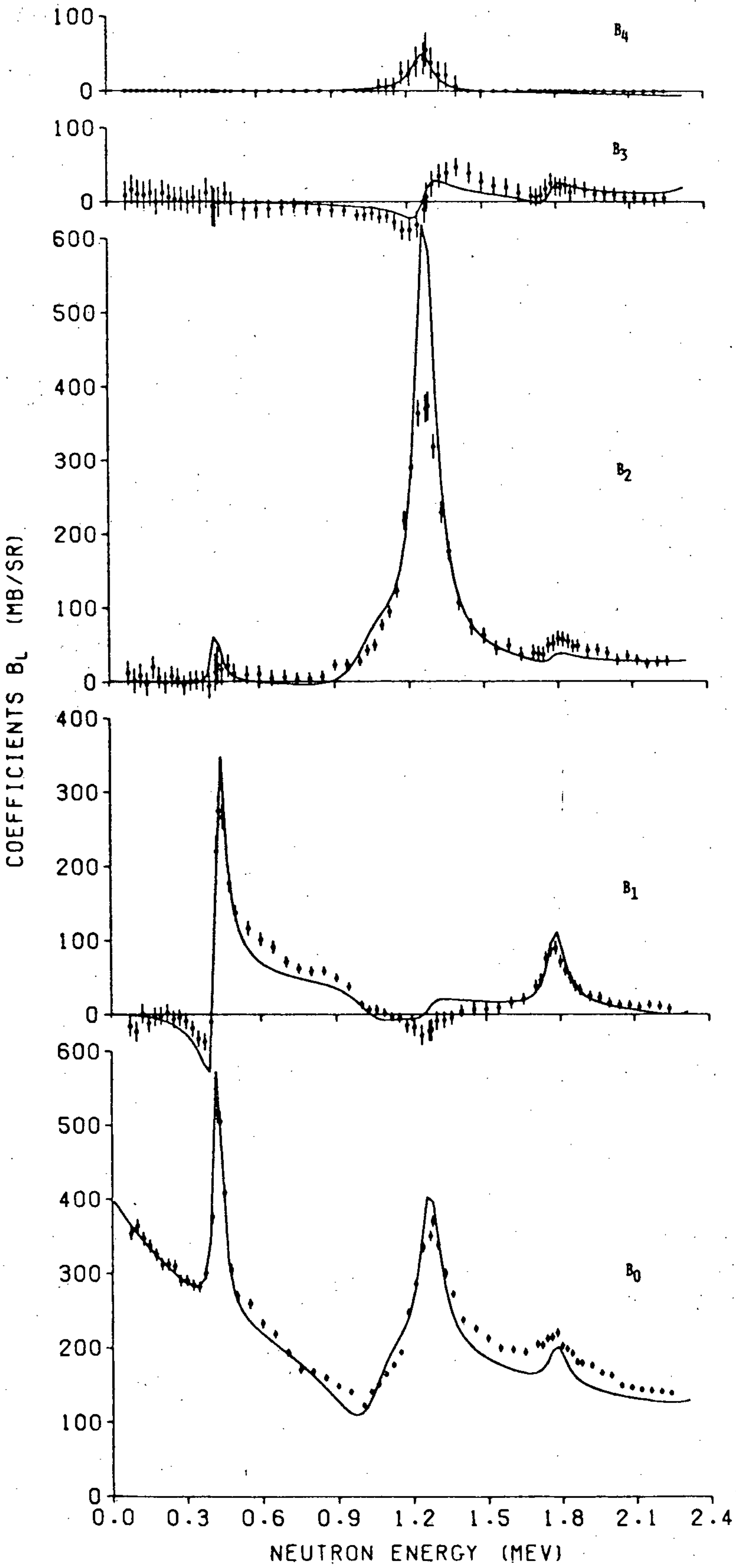

Figure 3.3 Plot of R-matrix fit for 0.0<En<2.4 MeV.

Table 3.1

R-matrix parameters for levels in $^{12}B$ used for final fit as shown in Figure 3.6. The nuclear radius parameter used in this R-matrix analysis was 4.5 Fermis.

| | Levels (MeV) | | | Reduced Width Amplitudes | | | Backgrounds | | | | Boundary Conditions | |
|---|---|---|---|---|---|---|---|---|---|---|---|---|
| $J^\pi$ | En(lab) | Ex(cm) | Eλ(cm) | $\gamma_{\lambda c}$ $(\mathrm{MeV,cm})^{1/2}$ | | | $Ro^{J^\pi}_{c'c}$ | | | | $B_c$ | |
| | | | | d-3/2 | | | | d-3/2 | | | | |
| $0^-$ | 4.60 | 7.59 | 4.10 | 0.3 | | | | 0.25 | | | (ℓ=2) | -0.500 |
| | | | | | | | | p-3/2 | | | | |
| $0^+$ | -- | -- | -- | -- | | | | 0.35 | | | (ℓ=1) | -0.125 |
| | | | | s-1/2 | d-3/2 | d-5/2 | | s-1/2 | d-3/2 | d-5/2 | | |
| $1^-$ | -- | -- | -0.75 | 0.70 | 0.00 | 0.00 | s-1/2 | 0.00 | 0.30 | 0.00 | (ℓ=0) | 0.000 |
| | 4.58 | 7.57 | 4.12 | 0.30 | 0.20 | 0.45 | d-3/2 | 0.30 | 0.25 | 0.00 | (ℓ=2) | -0.500 |
| | 4.75 | 7.73 | 4.22 | 0.30 | 0.45 | 0.20 | d-5/2 | 0.00 | 0.00 | 0.15 | (ℓ=2) | -0.500 |
| | | | | p-1/2 | p-3/2 | | | | | | | |
| $1^+$ | 1.77 | 4.99 | 1.60 | 0.10 | 0.25 | | | p-1/2 | p-3/2 | | | |
| | 3.53 | 6.60 | 3.17 | 0.20 | 0.20 | | p-1/2 | 0.35 | 0.00 | | (ℓ=1) | -0.125 |
| | 3.88 | 6.92 | 3.45 | -0.28 | 0.28 | | p-3/2 | 0.00 | 0.35 | | (ℓ=1) | -0.125 |
| | 5.85 | 8.73 | 5.30 | 0.20 | 0.00 | | | | | | | |
| | | | | s-1/2 | d-3/2 | d-5/2 | | | | | | |
| $2^-$ | -- | -- | -1.70 | 0.60 | 0.00 | 0.00 | | s-1/2 | d-3/2 | d-5/2 | | |
| | 1.09 | 4.37 | 0.65 | 0.40 | 0.00 | -0.65 | s-1/2 | 0.00 | 0.30 | 0.00 | (ℓ=0) | 0.000 |
| | 2.85 | 5.98 | 2.05 | 0.00 | 0.65 | 0.65 | d-3/2 | 0.30 | 0.25 | 0.00 | (ℓ=2) | -0.500 |
| | 4.80 | 7.77 | 4.26 | 0.00 | 0.40 | 0.25 | d-5/2 | 0.00 | 0.00 | 0.15 | (ℓ=2) | -0.500 |
| | 6.25 | 9.10 | 5.65 | 0.00 | 0.25 | 0.25 | | | | | | |
| | | | | p-1/2 | p-3/2 | | | p-1/2 | p-3/2 | | | |
| $2^+$ | 0.43 | 3.76 | 0.30 | 0.12 | 0.40 | | p-1/2 | 0.35 | 0.00 | | (ℓ=1) | -0.125 |
| | | | | | | | p-3/2 | 0.00 | 0.35 | | (ℓ=1) | -0.125 |

Table 3.1 (continued)

| | Levels (MeV) | | | Reduced Width Amplitudes | | Backgrounds | | | Boundary Conditions | |
|---|---|---|---|---|---|---|---|---|---|---|
| $J^{\pi}$ | En(lab) | Ex(cm) | Eλ(cm) | $\gamma_{\lambda c}$ (MeV,cm)$^{1/2}$ | | $Ro^{J^{\pi}}_{c'c}$ | | | $B_c$ | |
| | | | | d-3/2 | d-5/2 | | d-3/2 | d-5/2 | | |
| $3^-$ | 2.58 | 5.73 | 2.285 | 0.28 | 0.20 | d-3/2 | 0.25 | 0.00 | (ℓ=2) | -0.500 |
| | 5.31 | 8.24 | 4.77 | 0.35 | 0.35 | d-5/2 | 0.00 | 0.15 | (ℓ=2) | -0.500 |
| | 5.65 | 8.56 | 5.12 | 0.20 | 0.20 | | | | | |
| | | | | p-3/2 | | | p-3/2 | | | |
| $3^+$ | 2.45 | 5.61 | 2.20 | 0.25 | | | 0.35 | | (ℓ=1) | -0.125 |
| | | | | d-5/2 | | | d-5/2 | | | |
| $4^-$ | 1.26 | 4.52 | 0.31 | 0.95 | | | 0.15 | | (ℓ=2) | -0.500 |

these parameters were chosen to fit the entire region from 0.0 to 8.0 MeV and in the beginning it was not known that the data of Nelson, et al. ($2.3 < E_n < 4.0$ MeV) were low by 10% to 15% (see Section 3.5). Therefore, the background parameters should be readjusted to give slightly more magnitude in the even polymomial terms. However, the fit to the data is certainly sufficient to confirm the assigmments of Lane, et al. below 2.3 MeV neutron energy. It should be pointed out here that the narrow $1^-$ state at 1.0 MeV neutron energy not included in this R-matrix analysis is not the $1^-$ member of the $[1p_{3/2}^{-1}, 1d_{5/2}]$ particle-hole multiplet (see Section 3.6) as it is much too narrow to be formed by this simple coupling.

### 3.4.2 Analysis of the Region from 2.3 MeV to 4.0 MeV

Figure 3.4 shows a plot of the R-matrix fit to the data of Nelson, et al. from 2.0 MeV to 4.0 MeV neutron energy. The two well-defined resonances at 2.45 MeV and 2.75 MeV neutron energy have been previously assigned $3^+$ and $3^-$ respectively and those assignments are confirmed by the present R-matrix fit which is in agreement with the data in both shape and magnitude. However, in the present R-matrix analysis, the broad state reported at 2.65 MeV neutron energy by Nelson, et al. could not be fitted assuming a $1^-$ state as previously (tentatively) assigned. A $2^-$ assignment to this broad resonance produced the solid curve shown in Figure 3.4 while a $1^-$ assignment produced the

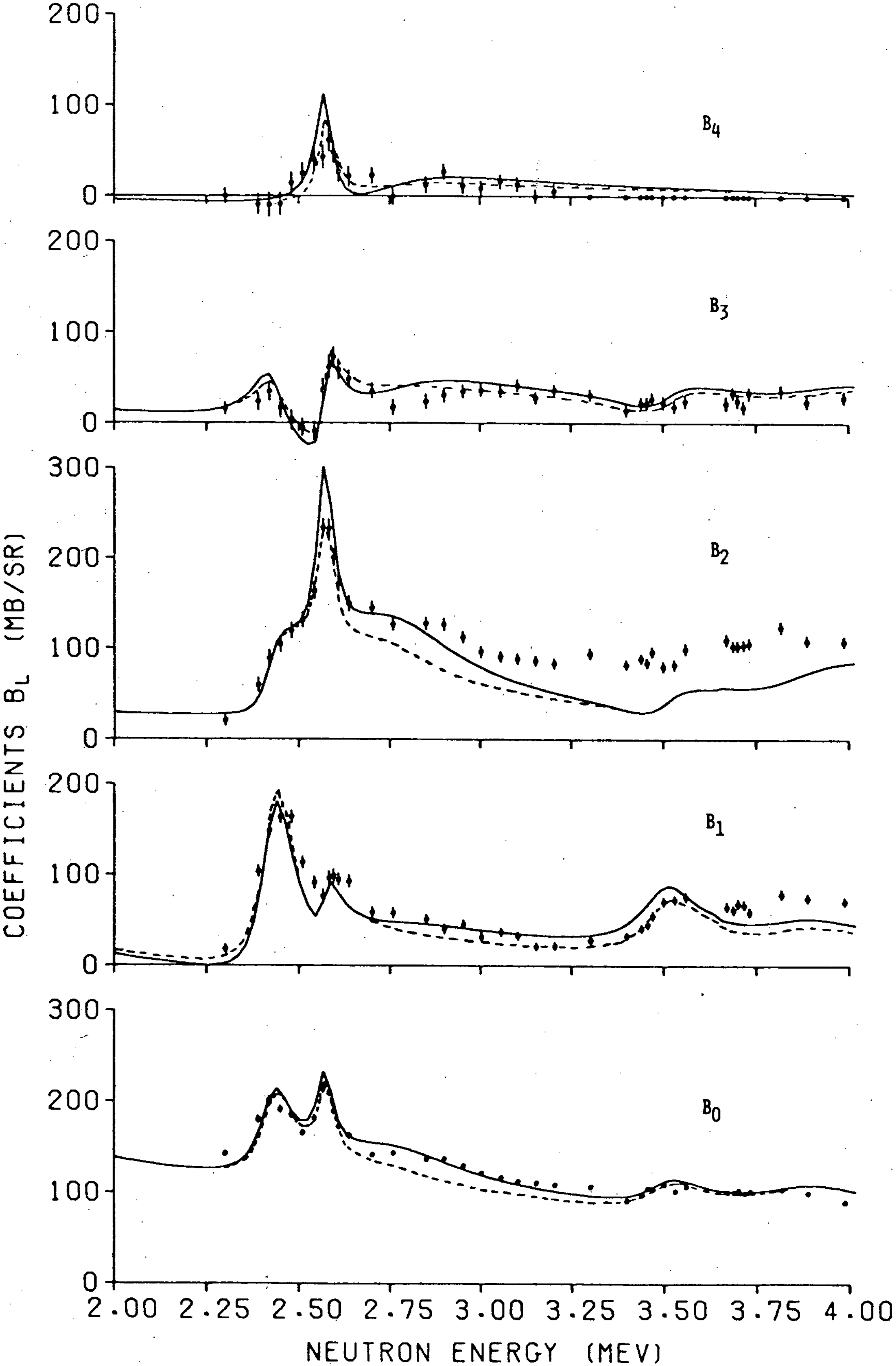

Figure 3.4 Plot of R-matrix fit for 2.0<En<4.0 MeV.

dashed line. It seems clear that the $2^-$ assignment fits the data better, particularly in view of the fact that the data of Nelson, et al. appear to be approximately 10% low in this region (see Section 3.5). While there may be some support from shell model theory for a $1^-$ assignment here (see Section 3.6) the experimental data do not necessarily confirm its existence at this energy. This is an important assignment from the standpoint of nuclear structure and will be considered further in Chapter 4. The present R-matrix fit from 3.0 to 4.0 MeV leaves something to be desired. Hundreds of cases of angular momentum and parity assignments with variations in R-matrix parameters were tried without success in fitting this region. While two $1^+$ assignments as previously (tentatively) assigned by Nelson, et al. are shown in Figure 3.4, it is obvious that difficulty exists in fitting the $B_1$ and $B_2$ coefficients in this region. Positive parity assignments helped to fit the $B_1$ terms and negative parity assignments, the $B_2$ terms, as expected. However, no combination could be found that would yield a respectable fit to this region and it is concluded by the author from hundreds of attempts to fit this region that either some unusually complicated resonance phenomenon is occuring in this region for which the correct R-matrix parameters were not found, or that the data are wrong. Section 3.5 and Chapter 4 will further discuss the problems of the data in this energy region.

### 3.4.3 Analysis of the Region from 4.0 MeV to 8.0 MeV

Figure 3.5 shows a plot of the R-matrix fit to the present data from 4.5 to 7.5 MeV neutron energy. It is apparent from the data and from the fit to the data that this is a much more complicated region with which to deal. First, the region from 4.5 to 5.0 MeV neutron energy is composed of several narrow resonances which are only partially resolved by recent high resolution total cross section measurements (see Au 76 and Figure 3.13) and resolved in the present differential cross section measurements as only a broad composite resonance. The magnitude of the $B_2$ coefficient in this region is large with the $B_3$ and $B_4$ coefficients showing only increasing trends. Numerous combinations of positive and negative parity states were tried, but it was difficult to maintain the shape and magnitude in $B_0$ and $B_1$ while increasing the magnitude of the $B_2$ coefficients, and at the same time limiting the magnitude of the $B_3$ coefficients. The final fit to this region is only partially successful. Because of the complexity of the problem, it is doubtful that further effort is warranted or would provide any more meaningful results since much of the underlying finer structure here is not resolved in this experiment or even in the higher resolution total cross section measurement of Auchampaugh, et al. However, a certain amount of information has been obtained from this effort. First, in order to achieve a general shape fit to this energy region in all coefficients, only states of

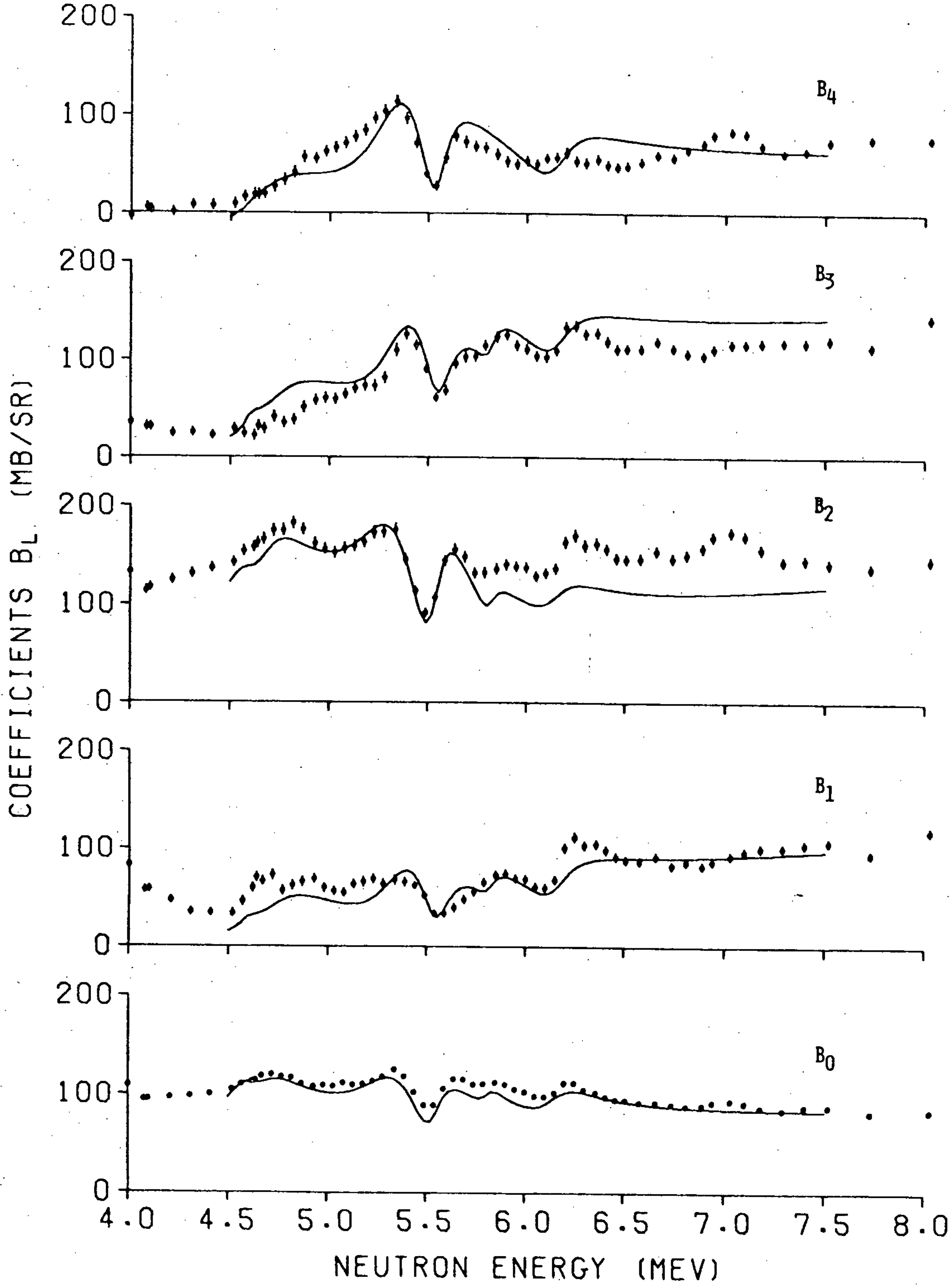

Figure 3.5 Plot of R-matrix fit for 4.0<En<8.0 MeV.

negative parity gave agreement. No combination of positive-parity states or combination of positive- and negative-parity states came even close to fitting the shape and magnitude of the Legendre coefficients in this region. Further, no success was achieved in the fitting with negative parity states of angular momentum greater that 2. The fit to the data in Figure 3.5 in this region consists of $0^-$, $1^-$, and $2^-$ states (see Table 3.1). While these parameters give the best fit to data, they are not to be construed as new assignments. They are undoubtedly not unique and a different combination of $1^-$ and $2^-$ states may give an improved fit to the data. As will be seen in Section 3.5, these values of $J^\pi$ in this region are consistent with what is known in the analog energy region of $^{12}C$. Another difficulty with trying to fit the region from 4.0 to 5.0 MeV is that resonance structure from 3.0 to 4.0 MeV will certainly effect the present fit from 4.0 to 5.0 MeV and the present analysis has been unable to fit the region from 3.0 to 4.0 MeV. In spite of this difficulty, the numerous R-matrix calculations with various combinations of states made in this region suggest that this composite peak is made up largely of $1^-$ and some $2^-$ strengths.

One of the main purposes for an R-matrix analysis of the present data was to determine the cause of the large dip in the total cross section at 5.5 MeV neutron energy. This dip has been observed by all total cross section measurements in this energy region. Such a dip is normally a characteristic effect of the interference between two states of the same angular momentum and parity having roughly the same probability for formation and decay in the same channels. The fact that this dip is seen in all the higher Legendre expansion coefficients is significant because it imposes limits on the angular momentum and parity of the resonance states which cause this effect. Sum rules of the angular momentum coupling coefficients (Bl 52) limit the states to $2^-$, $3^-$, or $4^-$ assignments. With $2^-$ assignments at 5.30 and 5.65 MeV neutron energy the magnitude of the fit was too small to begin to give the significant increase and interference effect seen in the $B_2$ and $B_4$ coefficients. With $3^-$ assignments and equal reduced widths in both d-3/2 and d-5/2 channels (see Table 3.1) the fit in Figure 3.5 was obtained. While $4^-$ assignments gave a better fit to the data than $2^-$ assignments, they still did not produce as good a fit as the $3^-$ assignments. As can be observed in Figure 3.5, the most difficult feature of these data to reproduce via the R-matrix was the sudden and significant increase in the $B_4$ coefficient around 4.5 MeV followed by the large dip at 5.5 MeV. It can be seen that the fit to the $B_4$ coefficients is good in both shape and magnitude. It is interesting to note that the best fit with $3^-$ assignments was obtained with equal reduced widths in both d-3/2 and d-5/2 channels (see Table 3.1) even though the shell model predicts mainly d-3/2 strength in this region (see Section 3.6).

Beyond the pronounced interference dip there exist two resolved resonances at 5.84 and 6.21 MeV neutron energy, respectively. The resonance at 6.21 MeV shows evidence of being a composite peak made up of two resonances but this was not clearly resolved in either total cross section measurements or in the present data. For the resonance at 5.85 MeV neutron energy the R-matrix analysis yielded a best fit with a $1^+$ assignment. It is not clear from the Legendre expansion coefficients of the differential cross section whether this peak is present or not in the $B_4$ term. Negative parity assignments greatly increased the magnitude of the $B_4$ terms while the positive parity assignment gave resonable shape and magnitude agreement in $B_0$, $B_1$, and $B_3$ coefficients while not affecting the $B_4$ coefficients, as would be expected from the aforementioned sum rules. Therefore, this state has been tentatively assigned $1^+$.

The state at 6.21 MeV neutron energy has been assigned a very tentative $2^-$ and may well indeed be an unresolved composite of two resonances. While the shape and magnitude of the fit to this resonance are reasonable in most of the coefficients the key factor for this negative parity assignment comes in the $B_4$ coefficient which is the least well-fit. In order to get the correct shape of the fit to the $B_4$ coefficients above 5.5 MeV it was necessary to postulate a negative parity (d-wave) state to interfere with the $3^-$ (d-wave) state, thus "forcing" the shape of the fit to conform to the data. There can be no doubt that a reasonably strong d-wave state exists in this region. The problem of the magnitude of the fit in the $B_0$ and $B_2$ coefficients above approximately 5.6 MeV is due to this interference of the $2^-$ d-wave state with the $3^-$ d-wave state at 5.66 MeV neutron energy. It is clear from Figure 3.5 that not exactly the correct parameters have been found and this may further be compounded if the resonance at 6.21 MeV neutron energy is indeed two unresolved resonances.

A final interesting feature in this region is the broad structure at 7.0 MeV neutron energy. No success whatsoever was enjoyed in attempting to fit this structure with R-matrix parameters. From the data of Figure 3.5, it appears to be composed of d-waves, but it is not seen in the recent total cross section work of Auchampaugh, et al. (Au 76 and Figure 3.13). Several very narrow resonances have been observed in this region (Aj 75, Au 76) and it is conceivable that they are narrow d-wave states, the unresolved composite of which is seen in the present work. As the terms which make up the even Legendre polynomial coefficients contain squared as well as cross terms, while the odd Legendre polynomial coefficients only contain cross terms, perhaps, on the average, the effect seen in the present data is reasonable. However, no solid explanation of this phenomenon is available at this time. Figure 3.6 shows the final R-matrix fit to the data of $^{11}B+n$ for neutron energies from 0.075 to 8.00 MeV.

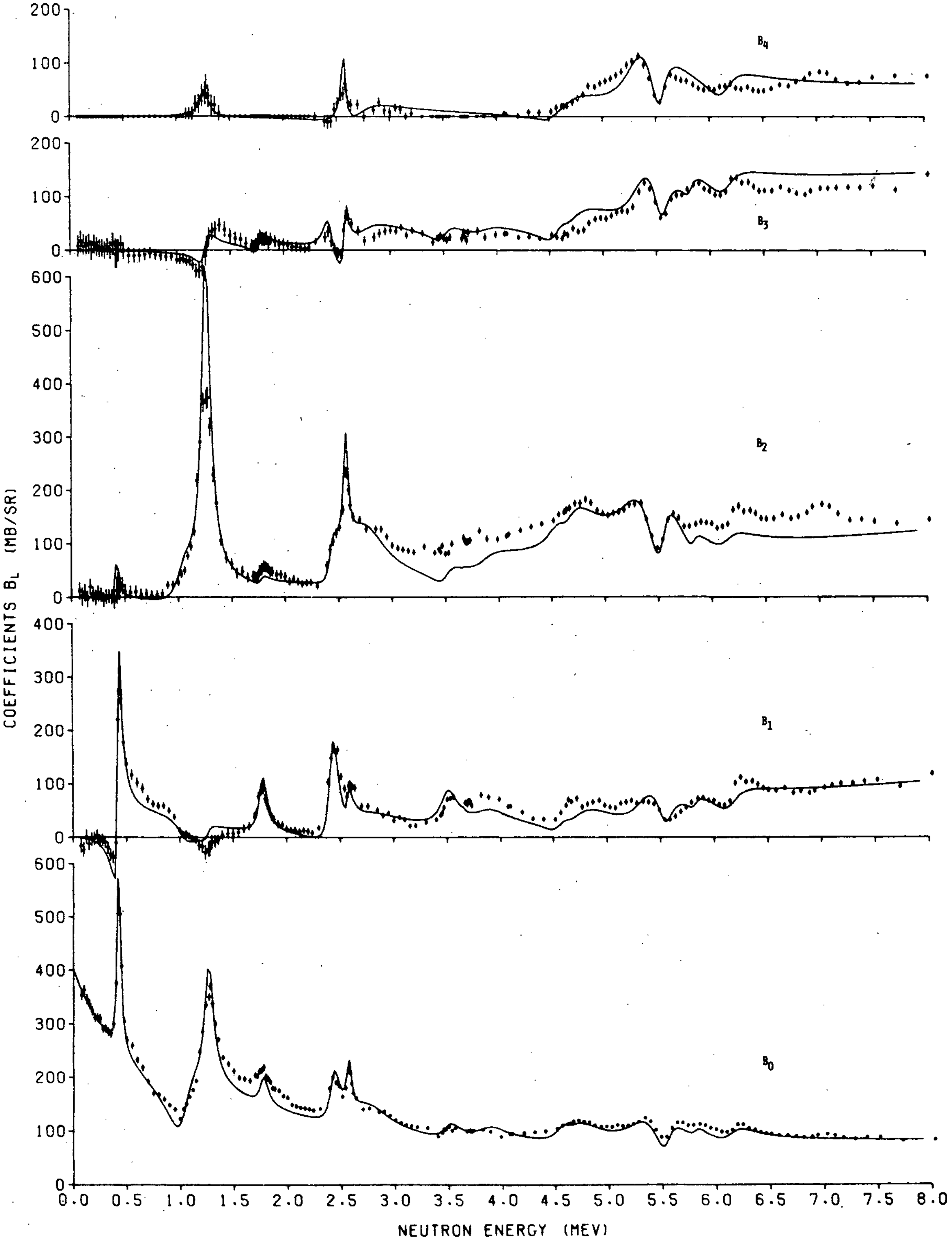

**Figure 3.6 Final R-matrix fit to the data of $^{11}B+n$.**

## 3.5 Comparison of Data with other A=12 Experiments

There exists a very limited number of measurements of neutron differential scattering cross sections on $^{11}B$ in the 4 MeV to 8 MeV region (Ne 73, Po 70, Ho 69). Section 3.5.1 will make graphical and numerical comparisons with what is known from the literature. Recent total cross section measurements (Au 76) are compared with the present integrated elastic data and the integrated nonelastic cross section is inferred in Section 3.5.2. Comparisons of results obtained in other reactions leading to states in $^{12}B$ and to T=1 states in $^{12}C$ are also discussed.

### 3.5.1 Comparison with other $^{11}B + n$ Measurements

Nelson, *et al*. (Ne 73) have measured differential elastic cross sections from 2.4 MeV to 4.4 MeV. A comparison of that measurement at 4.09 MeV with the present elastic results is shown in Figure 3.7 and Table 3.2. The curve in Figure 3.7 is a least-squares fit of five Legendre polynomials to the present data. Table 3.2 is a comparison of the integrated elastic cross sections for various sets of data. While the shape agreement is generally satisfactory, Nelson's measurements at 3.99, 4.09, 4.19, 4.29, and 4.39 MeV average 7 to 15 percent low in absolute value of the integrated elastic cross section when compared to the present work. As the 4.08 MeV measurement was also a $^{12}C$+n check point which demonstrated the accuracy of the present work, it is concluded that Nelson's measurements are 7 to 15

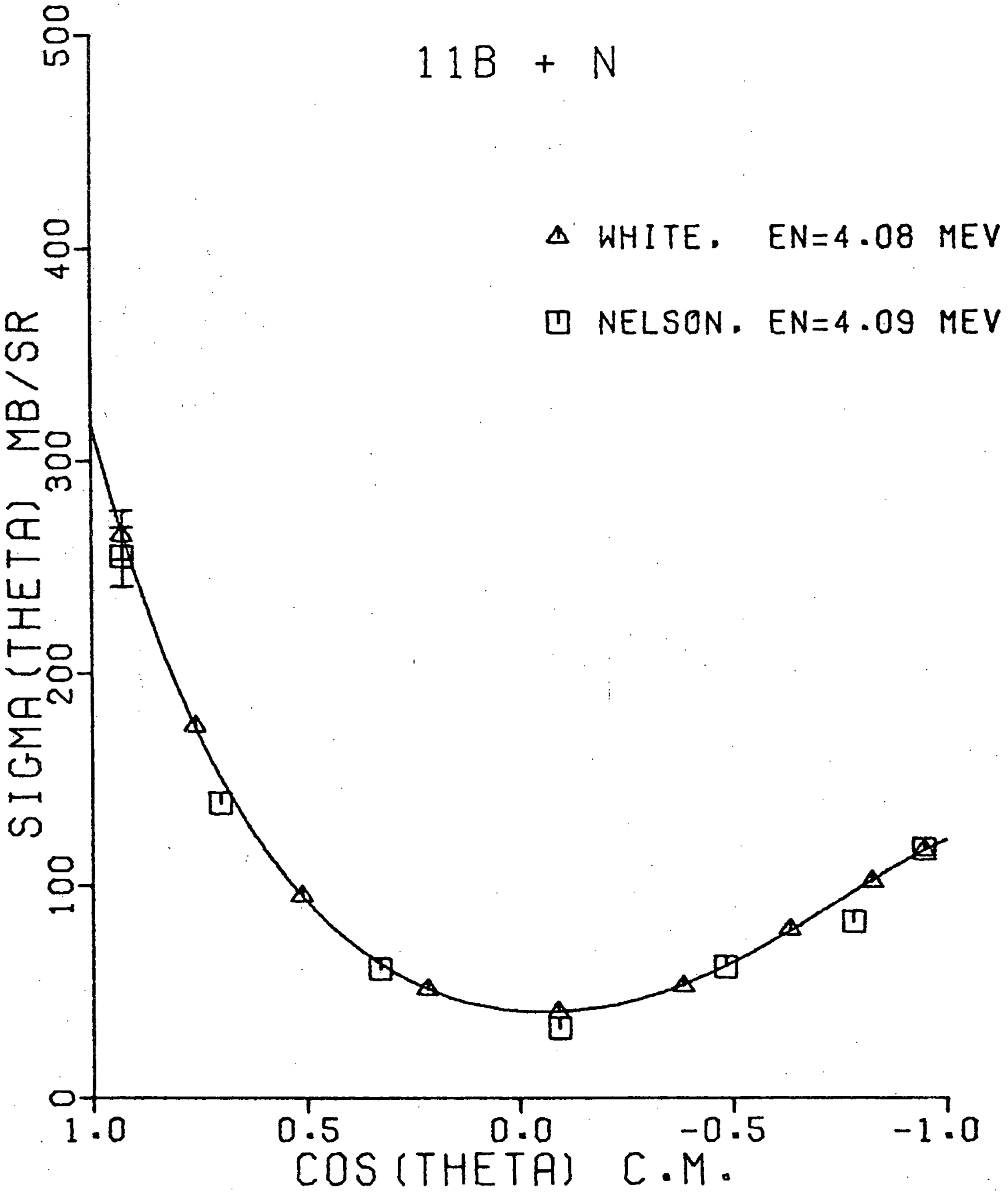

Figure 3.7 Plot of comparison of data of White, et al. and Nelson, et al. for En=4.08 MeV.

Table 3.2

Comparisons of the integrated elastic differential cross sections ($\sigma_{el}=4\pi B_o$) of other measurements with the present data.

| Neutron (Lab) Energy | | $\sigma_{el}=4\pi B_o$ | Difference |
|---|---|---|---|
| White, *et al.* | 4.00 MeV | 1374 mb | |
| Nelson, *et al.* | 3.99 | 1131 | 17.7% low |
| White, *et al.* | 4.08 | 1196 | |
| White, *et al.* | 4.10 | 1202 | |
| Nelson, *et al.* | 4.09 | 1112 | 7.3% low |
| White, *et al.* | 4.21 | 1221 | |
| Nelson, *et al.* | 4.19 | 1171 | 4.1% low |
| White, *et al.* | 4.31 | 1235 | |
| Nelson, *et al.* | 4.29 | 1098 | 11.1% low |
| White, *et al.* | 4.41 | 1260 | |
| Nelson, *et al.* | 4.39 | 1066 | 15.4% low |
| White, *et al.* | 4.31 | 1235 | |
| Porter, *et al.* | 4.31 | 1199 | |
| Porter, *et al.* | 4.34 | 1403 | 17.0% high |
| White, *et al.* | 4.82 | 1475 | |
| Porter, *et al.* | 4.82 | 1761 | 19.4% high |
| White, *et al.* | 7.52 | 1106 | |
| Hopkins, *et al.* | 7.55 | 1270 | 14.8% high |

percent low in the 4.0 to 4.4 MeV region. Section 3.5.2 will discuss Nelson's measurements from 2.4 to 4.0 MeV. The only other differential scattering cross section measurements in this region are those of Porter, *et al.* (Po 70). Figure 3.8 shows a comparison of the present elastic data with two elastic measurements of Porter at 4.31 MeV and 4.34 MeV. Table 3.2 gives the integrated elastic cross section for these two measurements which are only 30 keV apart in a region where the cross section is known to be slowly varying (see Section 3.5.2), yet there exists a 16 percent difference in these two measurements. It can further be seen that Porter's 4.31 MeV measurement is not consistent (within error bars) in shape with his 4.34 MeV measurement and it is still further obvious that significant difficulty exists with the forward angle measurement of that work. This difficulty has been confirmed in correspondence with the group of researchers who performed that work (La 72). The only other measurement in this region is one at 4.82 MeV, also by Porter, *et al.* The shape and absolute value of that measurement at 4.82 MeV also differ in a similar way from the present measurement at 4.31 MeV and suggest Porter's elastic measurements to be approximately 18 percent high in the 4 MeV to 5 MeV region.

There exists one measurement of the neutron differential elastic scattering cross section at 7.55 MeV by Hopkins and Drake (Ho 69). The comparison with the present data at 7.52 MeV is shown in Figure 3.9. While the shape is

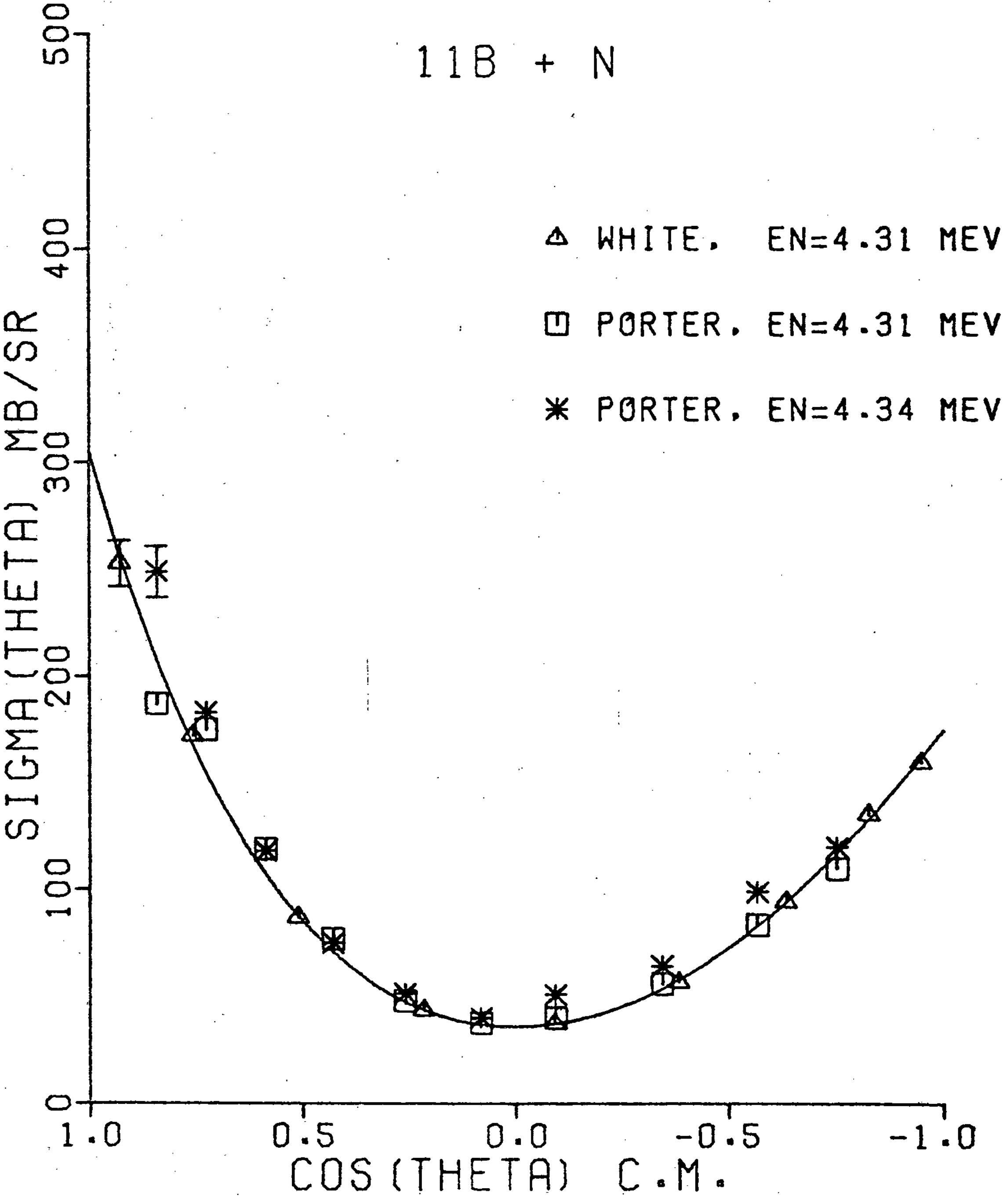

Figure 3.8 Plot of comparison of data of White, et al. and Porter, et al. for En=4.31 MeV.

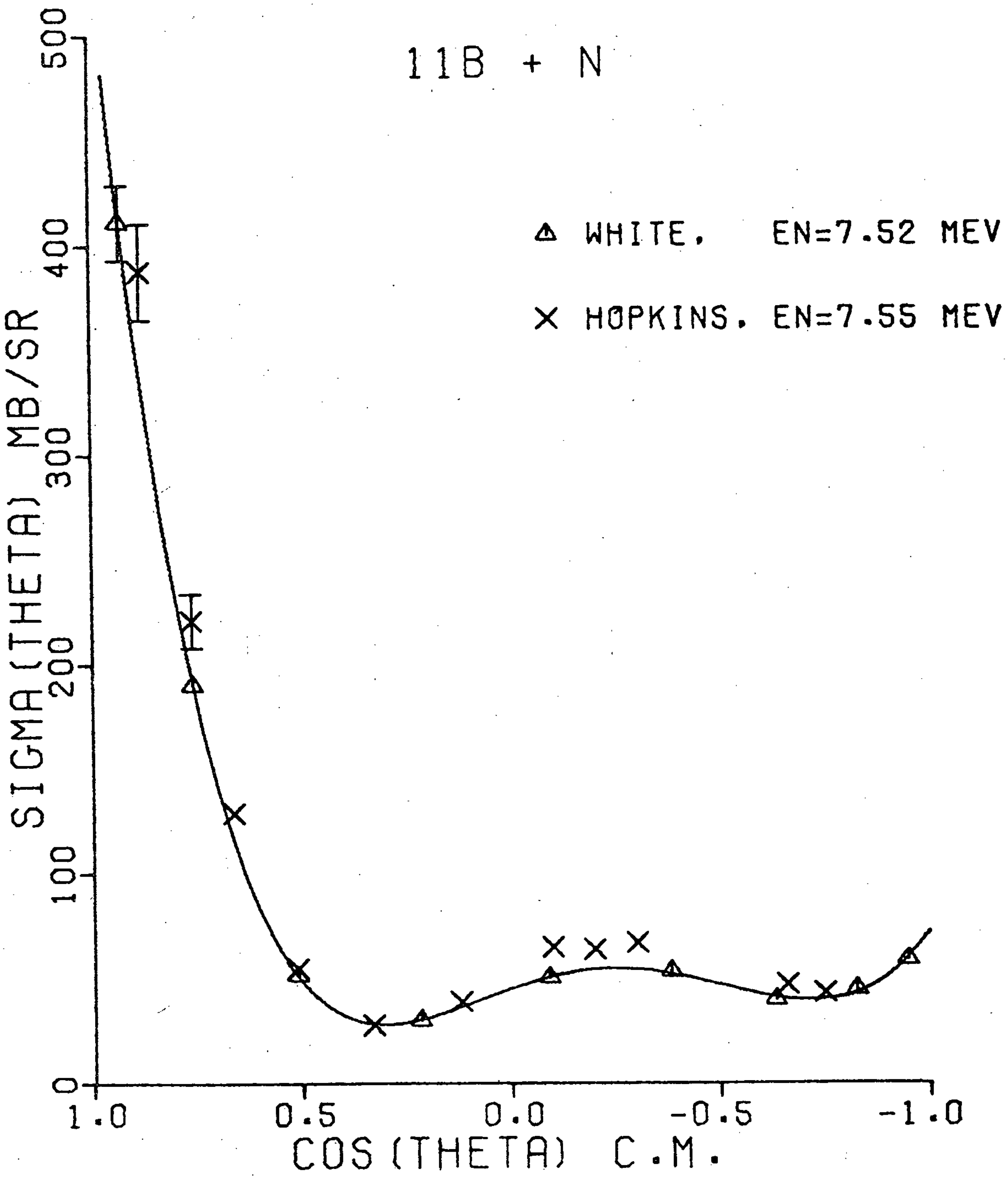

Figure 3.9 Plot of comparison of data of White, et al. and Hopkins, et al. for En=7.52 MeV.

in general agreement, the absolute values of Hopkins' data points are approximately 15% higher than those of the present work. There exist some very narrow resonances in this region and the 30 keV difference in the measurements could contribute to the difference seen in the plot. The excellent agreement in shape and absolute value of the $^{12}C$ check point at 6.94 MeV for the present results compared with those of other laboratories, and the consistency of remeasurement of the present data lend credence to the measurement at 7.52 MeV reported here.

### 3.5.2 The Integrated Nonelastic Cross Section for $^{11}B+n$

Recent high resolution total cross section measurements of $^{11}B+n$ by Auchampaugh, *et al*. (Au 76) at Los Alamos Scientific Laboratory are compared in this section with the integrated elastic scattering cross section measurements of Lane, *et al*. (La 70) from 0.1 to 2.3 MeV neutron energy, Nelson, *et al*. (Ne 73) from 2.3 to 4.0 MeV and the present work from 4.0 to 8.0 MeV. Figure 3.10 shows the comparison of Lane, *et al*. with Auchampaugh, *et al*. It can be seen that the agreement of the two measurements is quite good as should be expected since the first inelastic group from the first excited state of $^{11}B$ is not reached below 2.32 MeV neutron energy. As can be seen in Figure 3.11, the next inelastic groups are reached at 4.85, 5.48, and 7.35 MeV respectively. The $(n,\alpha)$ channel is reached at 7.24 MeV. Other than the $(n,\gamma)$ channel discussed in the next section

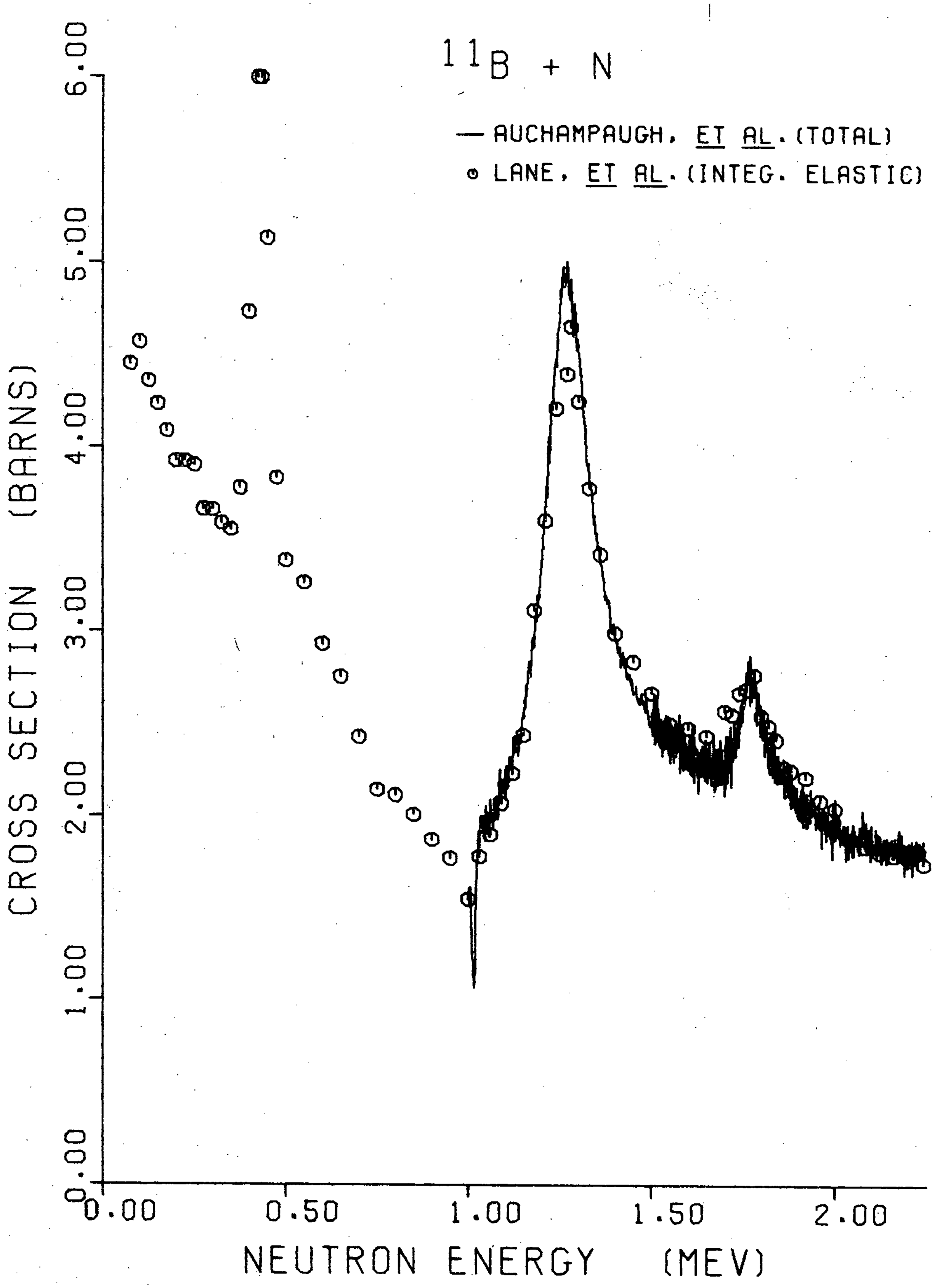

Figure 3.10 Plot of $^{11}B + n$ total cross section vs. integrated elastic cross section for $0.1 < En < 2.3$ MeV.

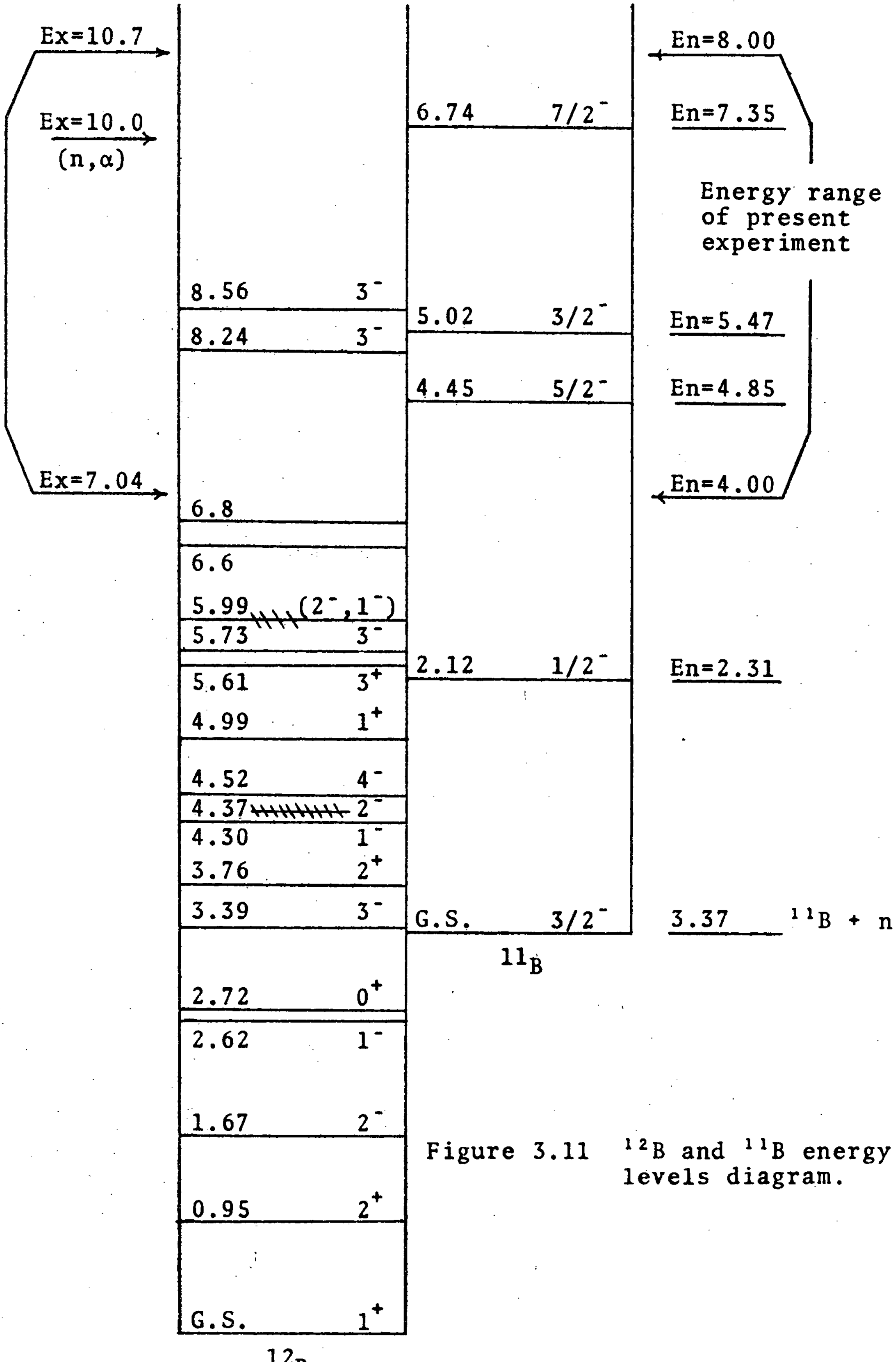

Figure 3.11 $^{12}B$ and $^{11}B$ energy levels diagram.

there exist no other reaction channels below 8.0 MeV.

Figure 3.12 shows the work of Nelson, et al. compared to that of Auchampaugh, et al. Even though the first inelastic group is reached at 2.32 MeV, it is unlikely that the magnitude and energy dependence of the inelastic cross section can make up the difference between the total and integrated elastic scattering cross section as shown in Figure 3.12. In the work of Lind and Day (Li 61) the excitation function for the 2.14 MeV gamma-ray excited by neutron inelastic scattering in $^{11}B$ was measured from threshold to approximately 3.2 MeV neutron energy. With the exception of a narrow resonance at 2.6 MeV with a peak height of approximately 40 mb, the cross section up to 3.2 MeV averaged less than 20 mb, an order of magnitude less than that indicated by the difference between the total and integrated elastic scattering cross section in Figure 3.12. Porter, et al. (Po 70) have measured the inelastic differential scattering cross section at 3.18 and 3.74 MeV neutron energy and have given for the integrated inelastic cross sections 11 mb and 45 mb, respectively, while the difference between the total and integrated inelastic cross sections for these same energies from Figure 3.12 give approximately 200 mb and 250 mb, respectively. Further discussion of these and related measurements in this energy range are considered in Chapter 4.

Figure 3.13 is a comparison of the present work with that of Auchampaugh, et al. Several general features are

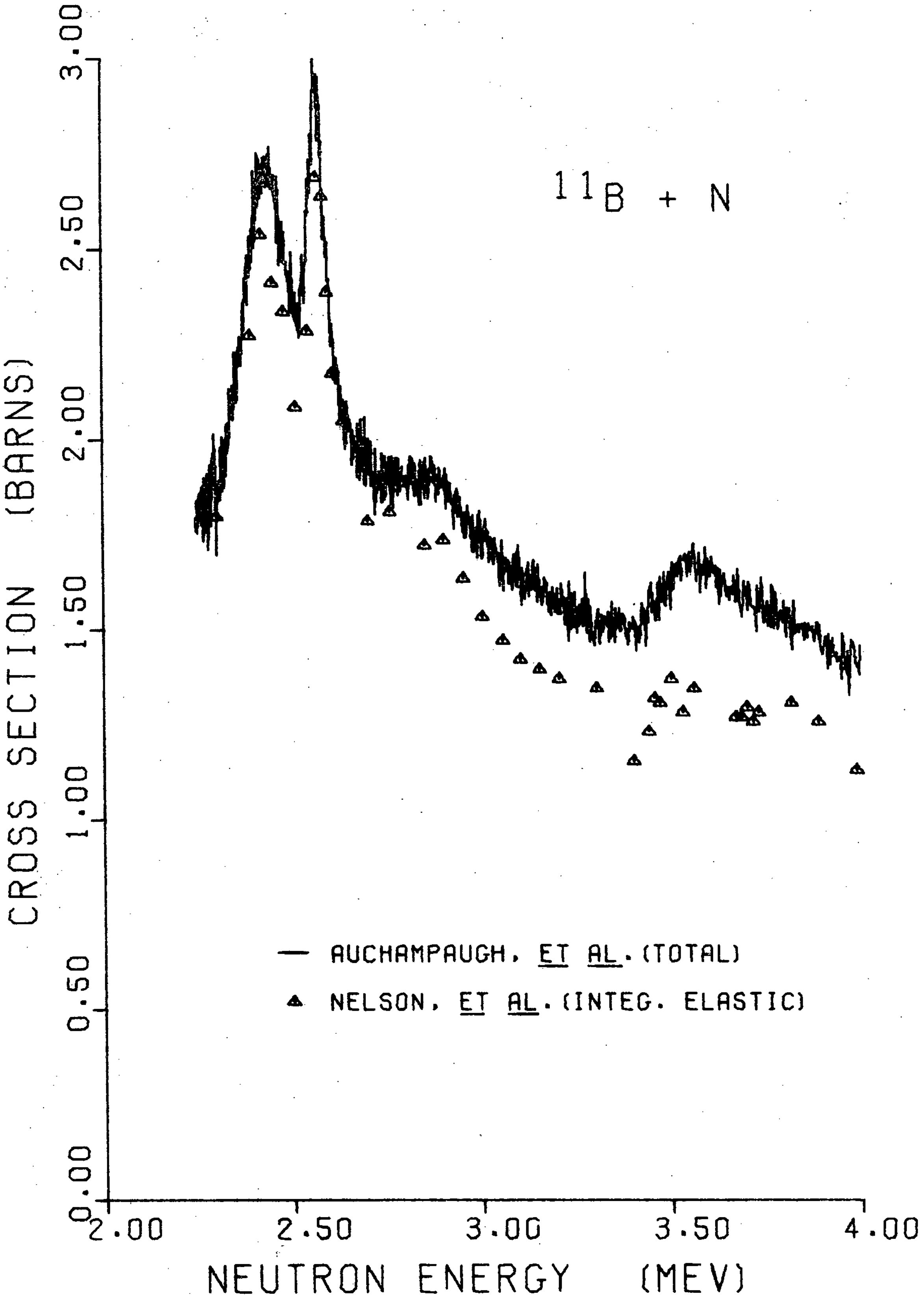

Figure 3.12 Plot of $^{11}$B + n total cross section vs. integrated elastic cross section for $2.0<E_n<4.0$ MeV.

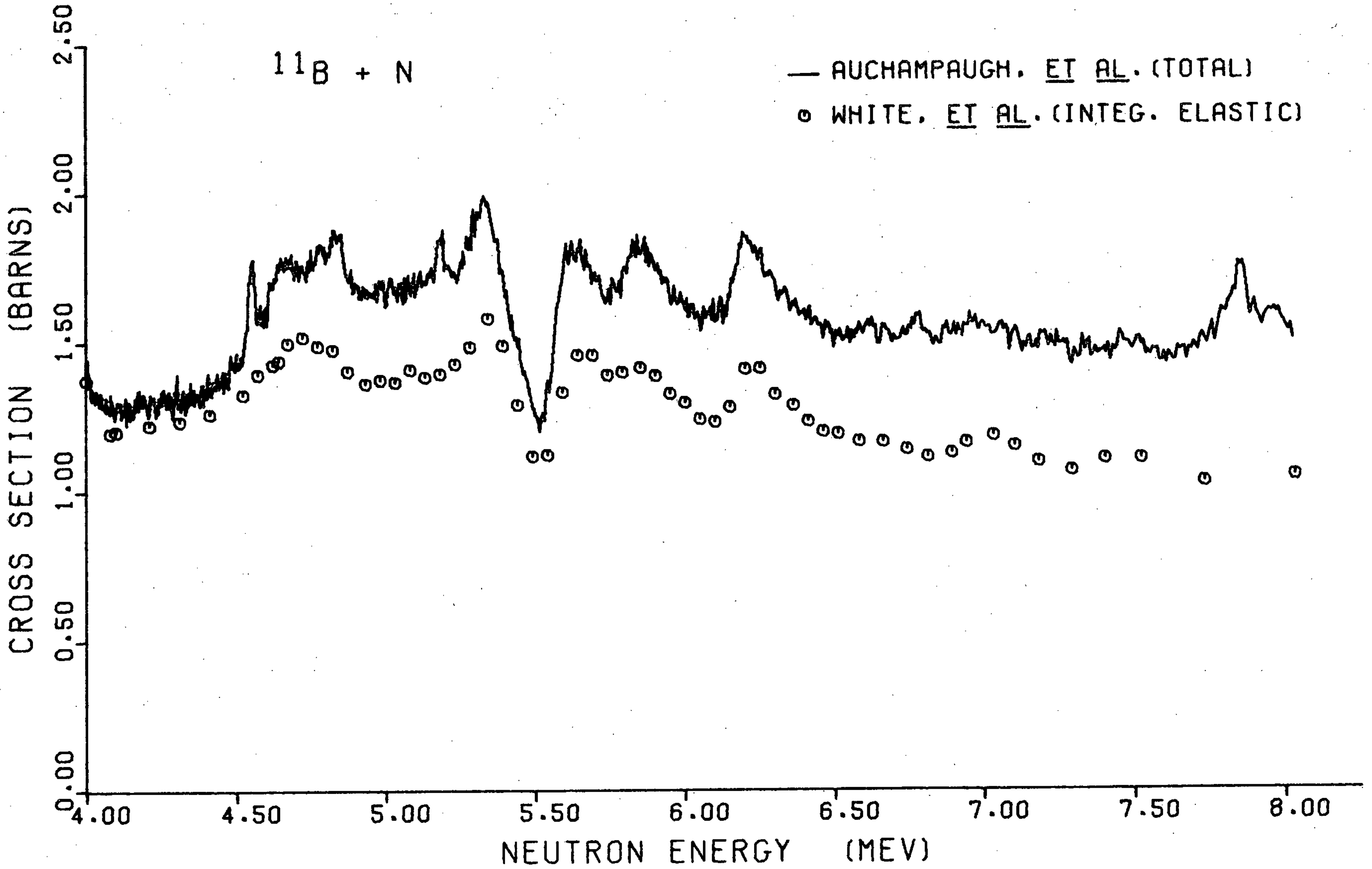

Figure 3.13 Plot of $^{11}$B + n total cross section vs. integrated elastic cross section for 4.0<En<8.0 MeV.

immediately clear. First, the structure agreement of the two sets of data indicate a close agreement in the energy calibration of the two experiments. Second, the change in the inelastic cross section is significant at approximately 4.5 MeV where significant resonance structure is seen in both the total and integrated elastic cross sections. Figure 3.14 shows a plot of the integrated nonelastic cross section obtained by subtraction of the present data from a computer average of the data of Auchampaugh, et al. which took into account the difference in resolution of the two experiments. The error bars on the data points in Figure 3.14 were assigned a value of 10% based on the absolute error stated for the total cross section work of Auchampaugh, et al. and for the error on the integrated elastic cross sections from the present measurements. It should be noted that while the average error on each data point in the present differential cross section measurements is approximately 4.7%, the average error on the integrated cross section of an angular distribution is only about 1.7%. Since the $(n,\alpha)$ channel is not open below 7.23 MeV, Figure 3.14 represents the total integrated inelastic cross section up to 7.23 MeV. This plot may be compared to measurements of the inelastic cross section of Porter, et al. at 4.31 and 4.82 MeV. Porter, et al. obtained 70 mb for the integrated inelastic cross section at 4.31 MeV which agrees almost exactly with that obtained in Figure 3.14 at 4.31 MeV. Porter, et al. obtained 162±10 mb for the integrated

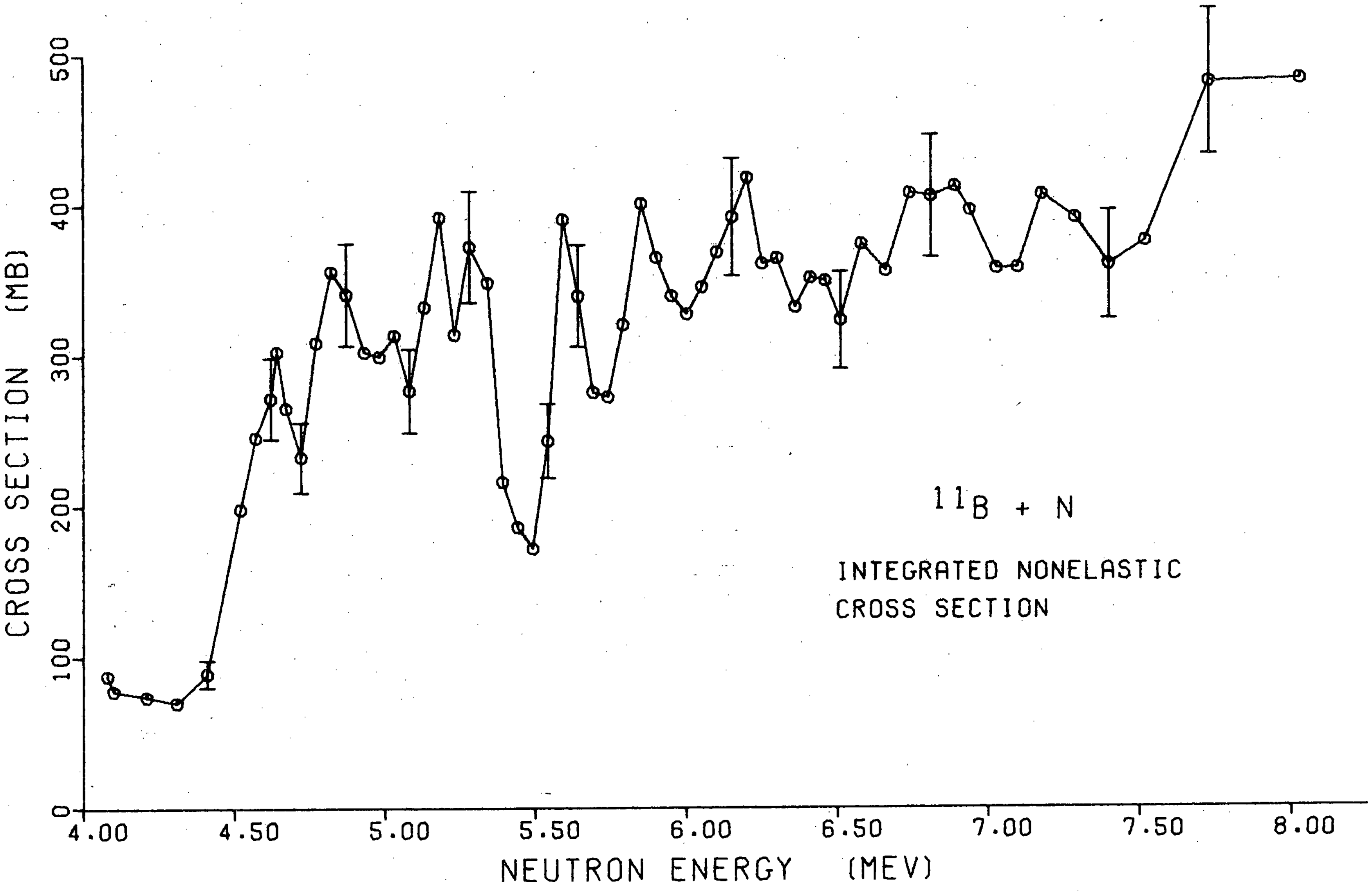
500
400
300
200
100
0
CROSS SECTION (MB)
4.00
4.50
5.00
5.50
6.00
6.50
7.00
7.50
8.00
NEUTRON ENERGY (MEV)
$^{11}B + N$
INTEGRATED NONELASTIC
CROSS SECTION

Figure 3.14

inelastic cross section at 4.82 MeV while the present work indicates that quantity to be 350±35 mb. The reason for this factor of two discrepancy between these two sets of data is not clear, and such a large disagreement indicates clearly that careful measurement of the inelastic cross sections should be made directly for 4.0 to 8.0 MeV. The uncertainty in the data of Auchampaugh, et al. is 1.5% and that of the present integrated work approximately 1.7%. The 4.82 MeV point is only 230 keV from a measured $^{12}C$+n distribution at 5.05 MeV, the results of which are shown in Figure 2.15. Remeasurement of the $^{12}C$+n distribution at 5.05 MeV showed consistency of the present work to be within 3% and in excellent agreement with that of Galati, et al. (Ga 72). It is therefore concluded that the plot in Figure 3.14 is a more accurate representation of the integrated inelastic cross section than that of Porter, et al.

The only other inelastic scattering measurement on $^{11}B$ has been made by Hopkins, et al. (Ho 69) at 7.55 MeV. They obtained 52±16 mb and 168±25 mb for the integrated inelastic cross sections from the first and second inelastic groups, respectively. Estimation of contributions from higher levels was 70±40 mb for a total of 290±50 mb for the integrated nonelastic cross section at 7.55 MeV. That value from the present work is 380±40 mb. While the plot in Figure 3.14 should never be considered to be a substitute for direct measurement of the inelastic cross sections, it does provided valuable information on the average magnitude of the integrated nonelastic cross section from 4.75 MeV to 7.75 MeV. In addition, it clearly shows the prominent interference dip at 5.50 MeV. This is significant because, as discussed in Section 3.4, the second best R-matrix fit to this interference region in the data was with two $4^-$ states. However, as can be seen in Figure 3.15, a $4^-$ state can only decay by d-waves to the second excited state of $^{11}$B ($5/2^-$), and further, cannot decay to the first excited state of $^{11}$B ($1/2^-$) for $\ell$ less than 4. As Figure 2.18 indicated, there exists no evidence that partial waves greater than $\ell=2$ are present. Figure 3.16 shows the penetrabilities for s-, p-, and d-waves. The outgoing neutrons for the second excited state of $^{11}$B (4.45, $5/2^-$) would have only 420 keV of energy and Figure 3.16 clearly shows the d-wave penetrability for this energy to be essentially zero. Therefore, since the interference from the two resonances at Ex=8.24 MeV and 8.56 MeV is seen in the total integrated inelastic cross section, $4^-$ assignments can be ruled out. On the other hand, as can be seen in Figure 3.15, the $3^-$ assignments allow decay to both excited states, the $\ell$-values being consistent with both the penetrabilities and experimental measurement.

### 3.5.3 Other Reactions Leading to States in the A=12 System

Related to the present measurements and R-matrix analysis are studies of several reactions leading to states in $^{12}$B and $^{12}$N as well as T=1 analog states in $^{12}$C. The first to be considered is the $^{11}B(n,\gamma)^{12}B$ or neutron capture

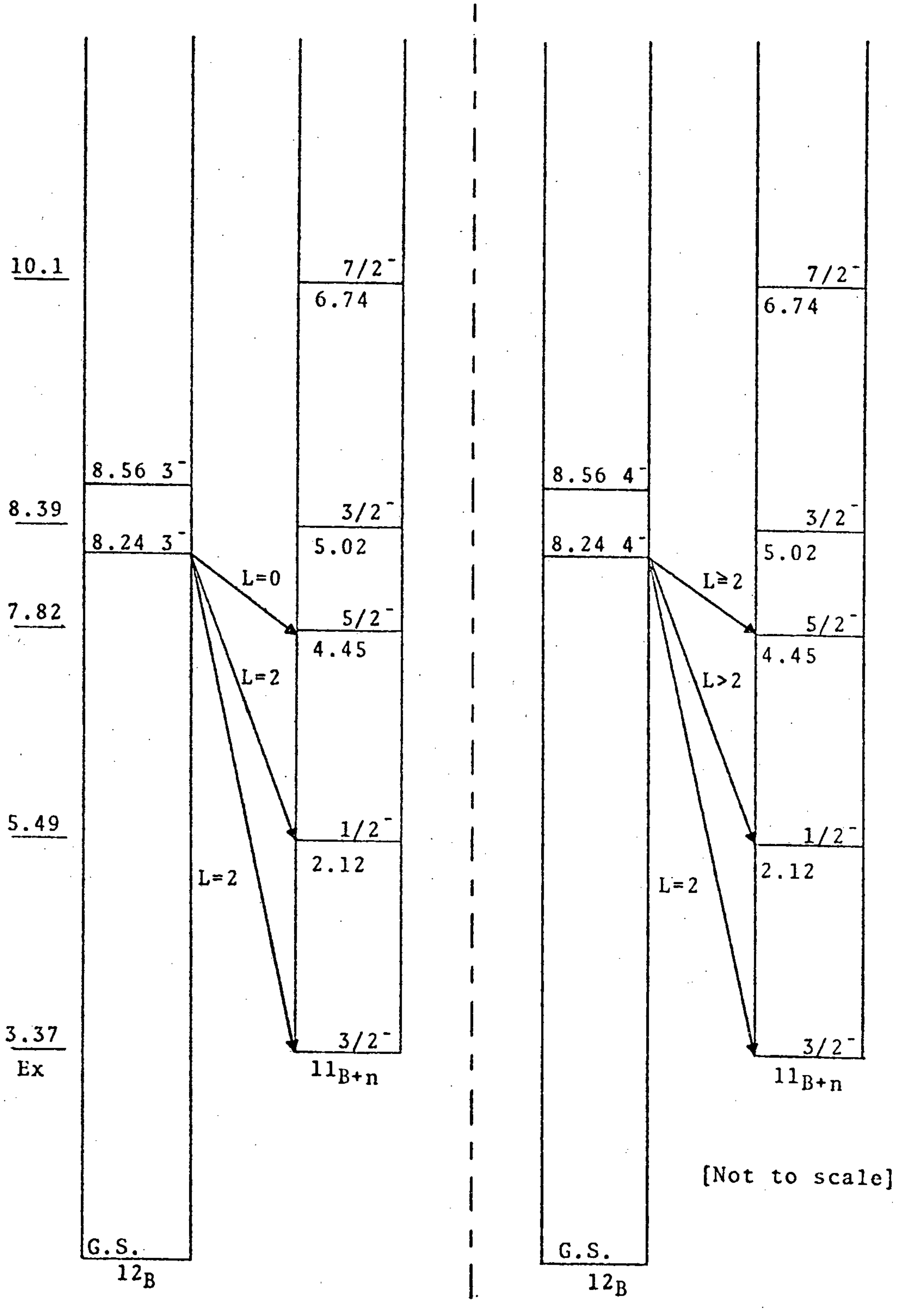

Figure 3.15 Decay scheme of $^{12}B^*$ to excited states in $^{11}B$. The neutron separation energy from $^{12}B$ is 3.37 MeV as indicated on the plot.

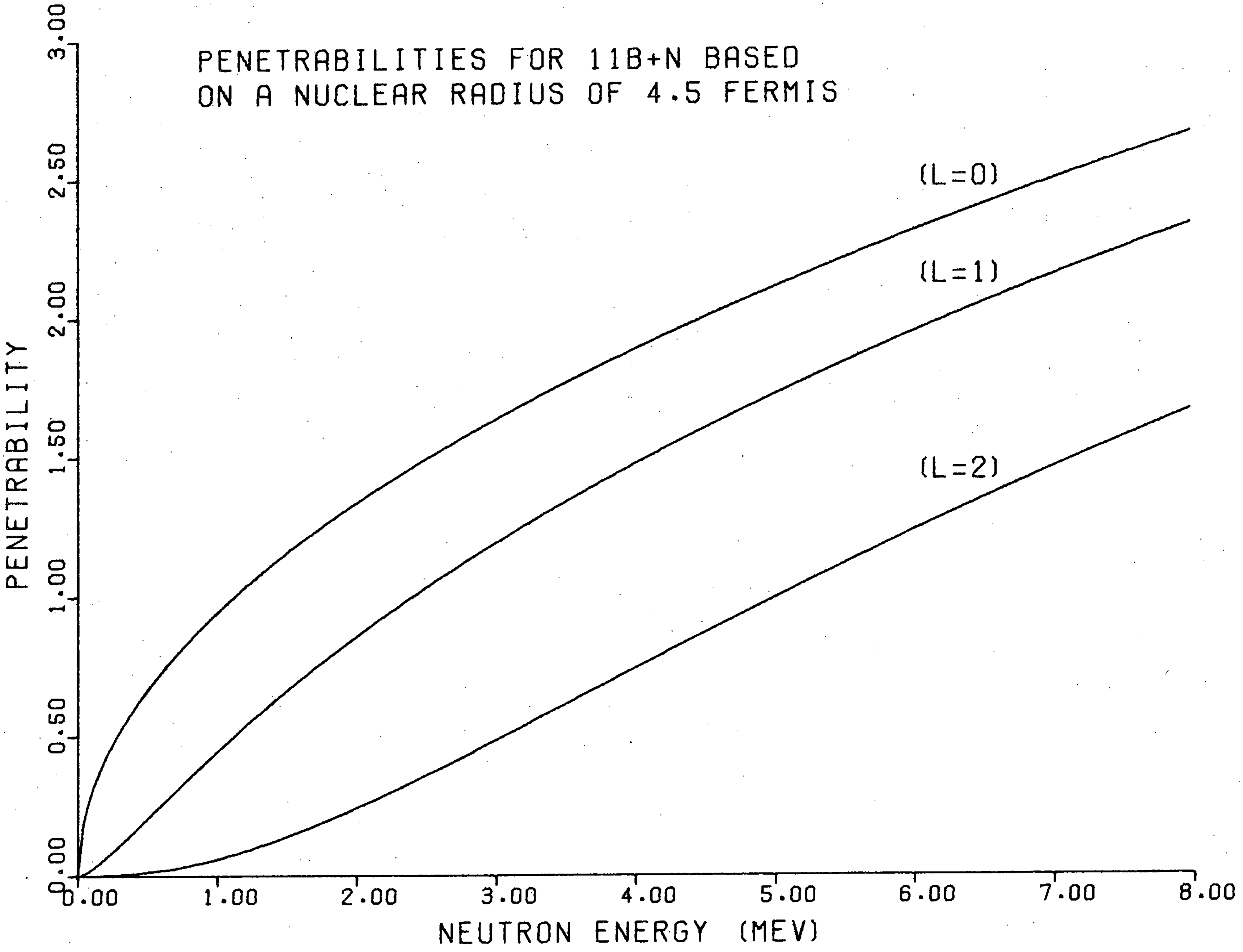
PENETRABILITIES FOR 11B+N BASED
ON A NUCLEAR RADIUS OF 4.5 FERMIS
(L=0)
(L=1)
(L=2)
PENETRABILITY
0.00
0.50
1.00
1.50
2.00
2.50
3.00
0.00
1.00
2.00
3.00
4.00
5.00
6.00
7.00
8.00
NEUTRON ENERGY (MEV)

Figure 3.16

reaction. Imhof, et al. (Im 62) have measured the cross section for this reaction from 0.14 MeV to 2.33 MeV (neutron energy) and at thermal energy. The measured value of this cross section for thermal neutrons is 5±3 mb. In the neutron energy range from 0.14 MeV to 2.30 MeV there exists some resonance structure but the cross section is in the microbarn region throughout. Therefore, this channel was neglected in the R-matrix analysis. There exists no known $(n,\gamma)$ measurement above 2.30 MeV on $^{11}B$.

Recent measurement of the $^{9}Be(^{7}Li,\alpha)^{12}B$ cross section has been made at $E(^{7}Li)=20$ MeV (Aj 75) and 37 states of $^{12}B$ with excitation energies less than 14 MeV were observed. However, no new assignments of angular momentum or parity were made. States in $^{12}B$ at excitation energies of 8.24, 8.58, 8.70, and 9.03 MeV seen in both the present work and that of Aj 75 have been discussed in Section 3.4.3. While a great deal of study has been made on the A=12 system, there exist few measurements on any of these nuclei in the energy region corresponding to the present study on $^{12}B$ where direct comparison of states can be made.

States in $^{12}B$ are also of interest in the study of the structure of $^{12}C$. The region of the present data on $^{12}B$ corresponds to excitation energies of approximately 22 MeV to 26 MeV (c.m.) in $^{12}C$ (see Figure 3.17). The states observed in $^{12}B$ are pure T=1 states and have their isobaric analogs in $^{12}C$. However, the corresponding energy region of $^{12}C$ contains both T=0 and T=1 states and therefore, the

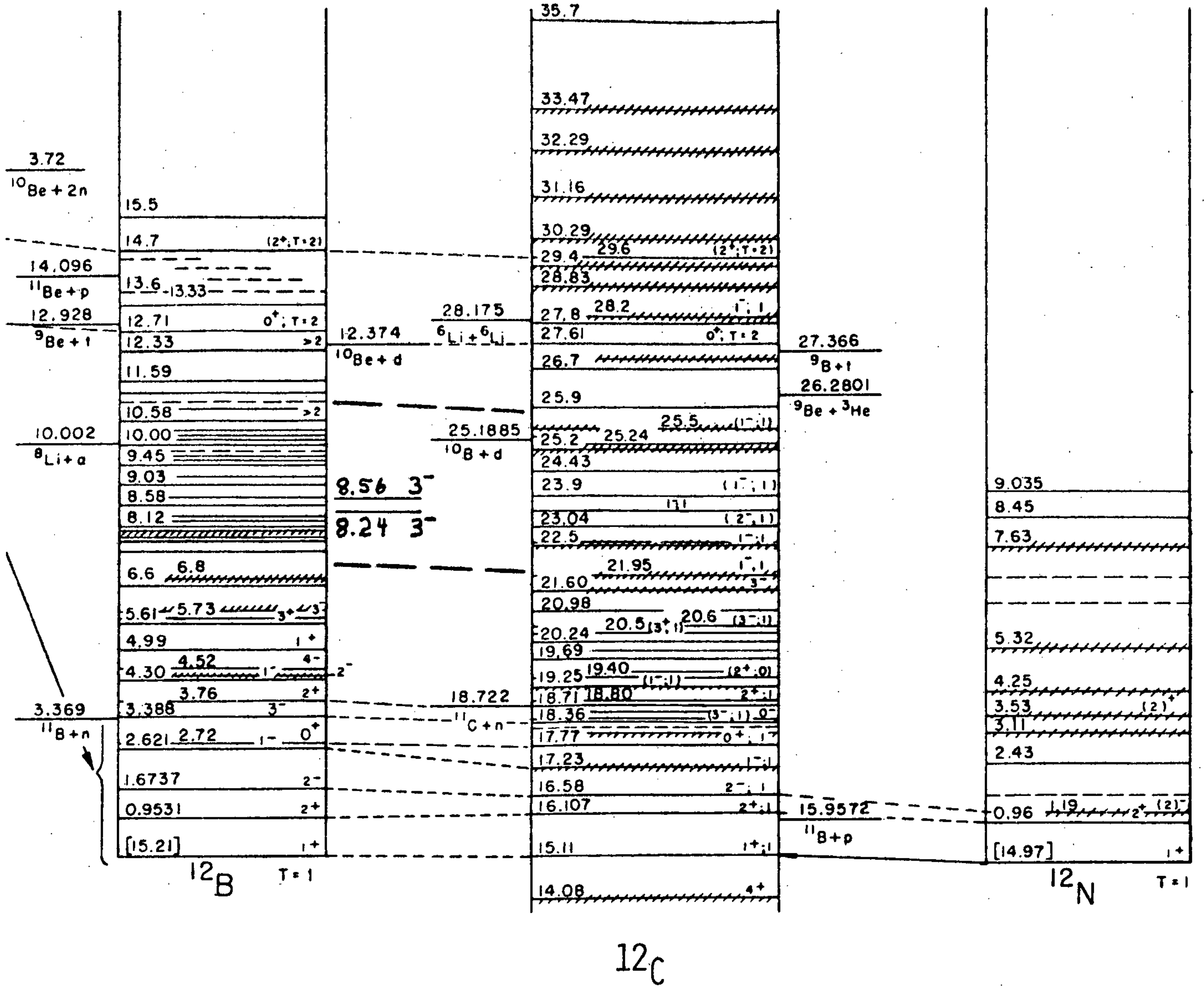

Figure 3.17 Partial energy level diagram of the A=12 system from reference Aj 75a.

study of $^{12}B$ should help to clarify the complex level structure of $^{12}C$. Much of the work in this region of $^{12}C$ (the so-called giant dipole resonance region) has been carried out via the $^{12}C(e,e')^{12}C$, $^{11}B(p,\gamma)^{12}C$, $^{12}C(\gamma,n)^{11}C$, $^{12}C(\gamma,p)^{11}B$ and $^{11}B(p,n)^{11}C$ reactions. Of approximately ten levels identified in $^{12}C$ in this energy region, four have been assigned $1^-$, T=1 states, three have been tentatively assigned $1^-$, T=1 states, one tentatively assigned $2^-$, T=1 and two have no assignment (Aj 75a). At this point there appears to exist no correspondence between the pure T=1 states in $^{12}B$ identified in Section 3.4.3 and the T=1 states identified so far in the corresponding region in $^{12}C$. However, it should be noted that most of the experiments to measure states in $^{12}C$ ($(p,\gamma_0)$, $(\gamma,p_0)$ and $(\gamma,n_0)$) in this region will "select" $1^-$, T=1 states due to selection rules (T change-self conjugate nucleus, parity change, and angular momentum change by one unit) and therefore states (such as the pair of $3^-$ states) of higher angular momentum will not be seen in these reactions.

Finally, recent measurement of the $^{12}C(^{3}He,t)^{12}N$ reaction at $E(^{3}He)=49.3$ MeV by Maguire, et al. have been reported (Ma 76). States confirmed or new states reported in $^{12}N$ in this measurement are at excitation energies of 2.42, 6.10, 7.13, 9.42 and 9.90 MeV. This work concludes, basically, that by comparison with the analog region in the mirror nucleus $^{12}B$, the structure of $^{12}N$ remains poorly known.

## 3.6 Comparison of Data with Shell Model Calculations

Most of the lower lying states in $^{12}B$ can be reasonably explained by simple shell model theory (La 70, Sh 63, Pa 56, Gi 64, Gu 68, Mo 71, and Bi 74). Considering the five protons and six neutrons in $^{11}B$, we expect to see simple particle-hole couplings between the p-3/2 proton hole of the target and a 1p-1/2, 1d-5/2, 2s-1/2, or 1d-3/2 incoming neutron which would manifest themselves as broad resonances in the excited structure of $^{12}B$. The splitting within the various multiplets formed by the couplings stated above is a result of the residual interaction between the proton hole and the last neutron. Calculations of the this type, using various residual interactions, are in agreement with experiment, in particular the $^{11}B(d,p)^{12}B$ reaction (Mo 71) for the first four levels of $^{12}B$ (Gu 68, Gi 64), i.e., the ground state and first excited state $(1^+,2^+)$ arising from the splitting of the $[1p_{3/2}^{-1}, 1p_{1/2}]$ particle-hole multiplet and the second and third excited states $(2^-,1^-)$ arising from the splitting of the $[1p_{3/2}^{-1}, 2s_{1/2}]$ particle-hole multiplet. In the states (unbound) observed from neutron elastic scattering experiments, we are mainly concerned with the structure arising from the coupling to the ground state of $^{11}B$ the 1d-5/2 and 1d-3/2 neutrons. The proximity of the 1d-5/2 and 2s-1/2 single particle states causes configuration mixing with some of the particle-hole states, as shown below.

Lane, *et al.* (La 70) have made shell model calculations which included configuration mixing of the $2^-$ states arising from the $[1p_{3/2}^{-1}, 2s_{1/2}]$ and $[1p_{3/2}^{-1}, 1d_{5/2}]$ particle-hole multiplets with the results shown in Figure 3.18. The arrows indicate the displacement of the $2^-$ levels as a result of configuration mixing. R-matrix analysis by Lane, et al. have identified the $3^-$, $2^-$, and $4^-$ states of the $[1p_{3/2}^{-1}, 1d_{5/2}]$ multiplet. From Figure 3.18 it can be seen that the $1^-$ member of this multiplet is predicted from the calculation to be at approximately 5.8 MeV excitation energy. This predicted state is within 200 keV of the broad resonance seen in the total cross section measurement of Auchampaugh, et al. shown in Figure 3.12 at 2.85 MeV, and provided the impetus for the measurements of Nelson, et al. in search of this state. From their R-matrix analysis they concluded that this broad state is $1^-$. It is clear from the present data and R-matrix analysis as well as those of Nelson, et al. that this broad state at 2.85 MeV neutron energy is of negative parity and angular momentum of either 1 or 2. As suggested by the present analysis and shown in Figure 3.4, this state is most probably a $2^-$ state, particularly when it is considered that the data of Nelson, et al. are at least 10% low in this region. If this is indeed the case then where is the $1^-$ broad resonance final member of the $[1p_{3/2}^{-1}, 1d_{5/2}]$ multiplet, or at least where is most of its strength? Figure 3.19 shows the comparison of the T=1 isobars in $^{12}$B and $^{12}$C along with the various particle-hole configurations calculated by Gillet and Vinh-

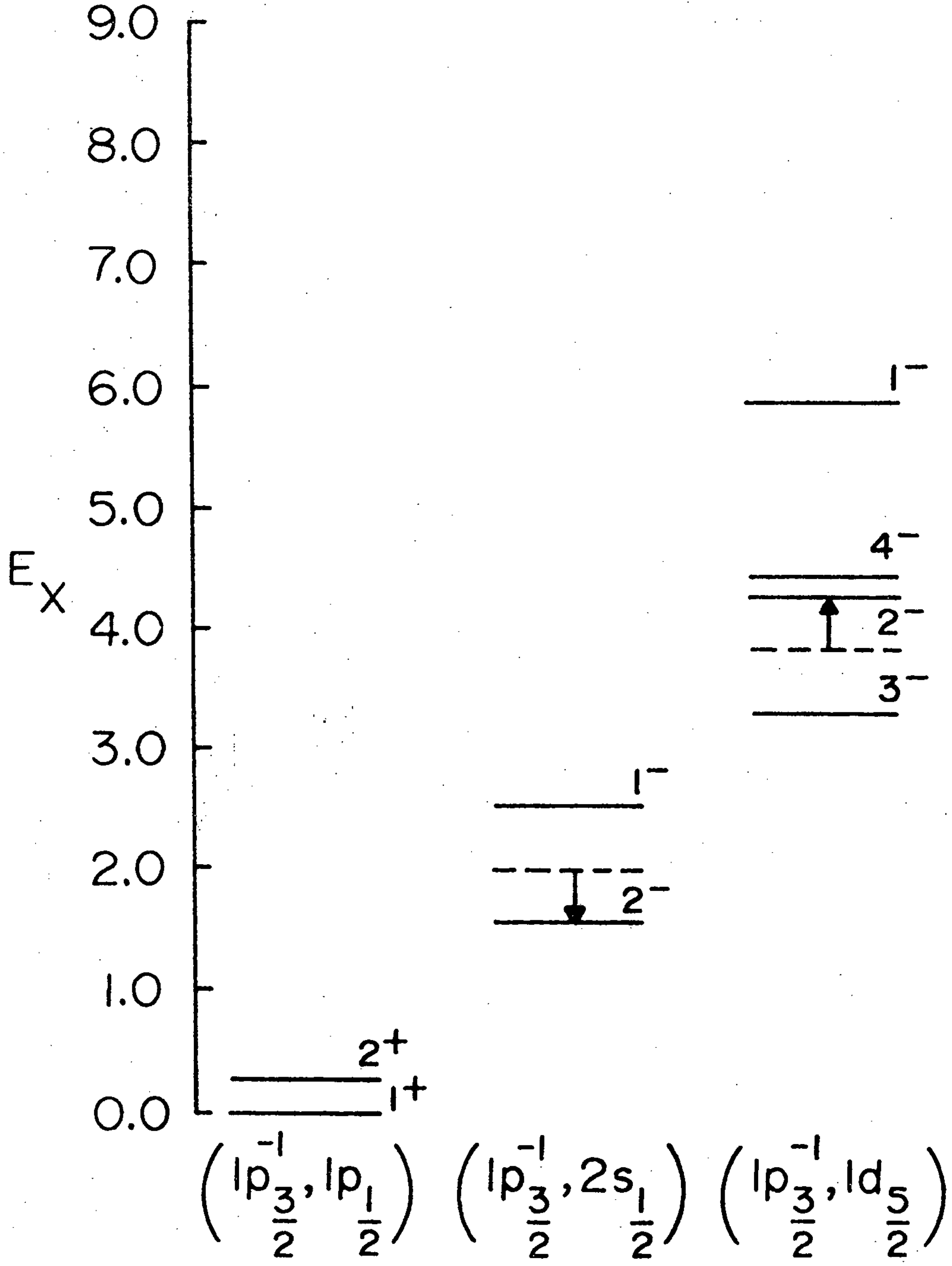

Figure 3.18 Predicted levels from shell model calculations on $^{12}$B from reference La 70.

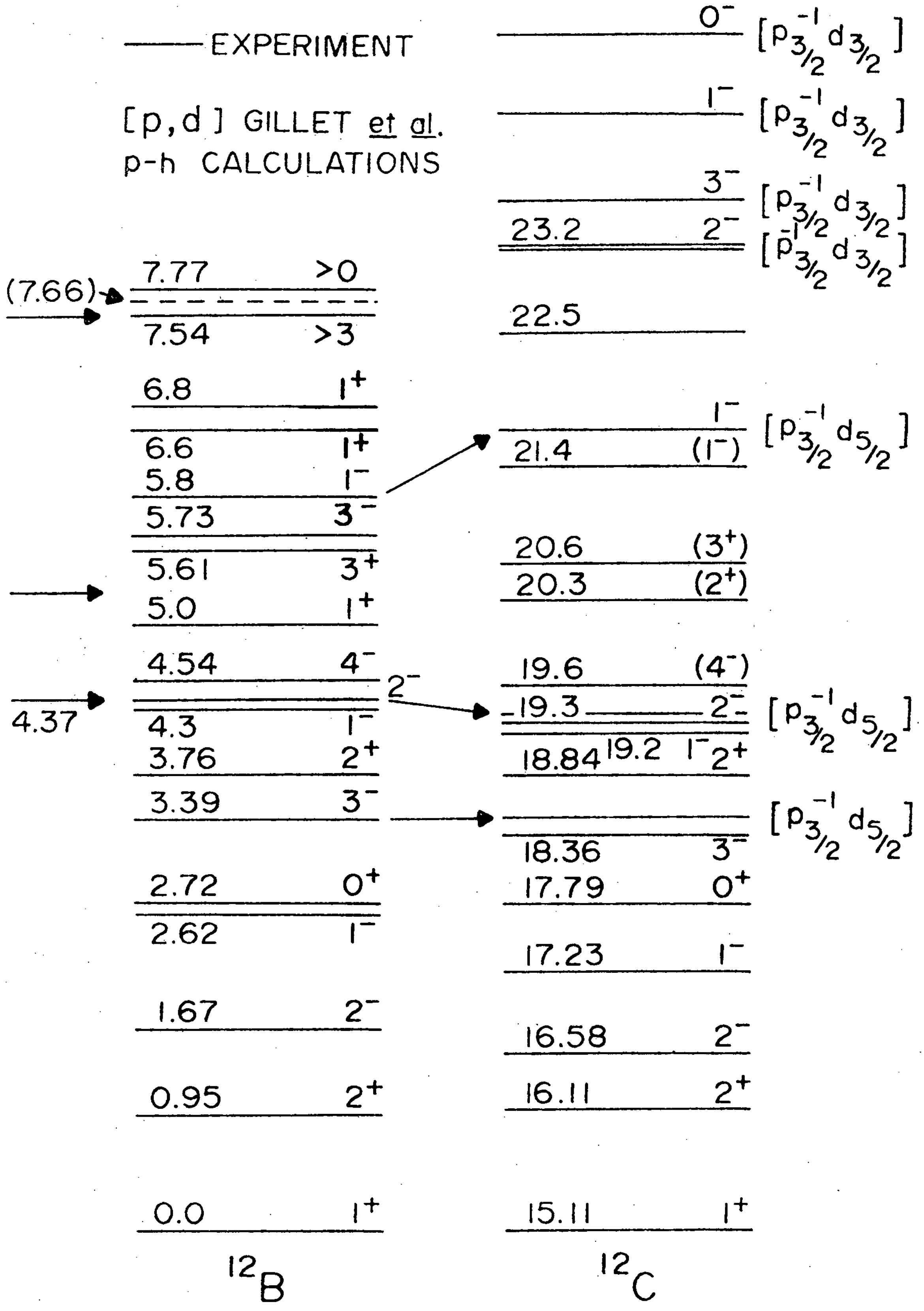

Figure 3.19 Comparison of the T=1 isobars in $^{12}B$ and $^{12}C$ taken from reference Ne 73.

Mau (Gi 64) which suggest the $1^-$ member of the $[1p_{3/2}^{-1}, 1d_{5/2}]$ multiplet lies somewhat higher than that predicted by Lane, et al. Birkholz and Heil (Bi 74) also predict the $1^-$ member of that multiplet to lie somewhat higher than predicted by Lane, et al. Calculated cross sections for elastic scattering of neutrons from $^{11}B$ as calculated by Birkholz and Heil as a function of neutron laboratory energy are shown in Figure 3.20. They state: "The $1^-$ member of the $(1d_{5/2}, {}^{11}B_{g.s.})$ multiplet does not appear in the spectrum ($E_x < 6$ MeV). It is shifted to higher energies and is spread over broad resonances in the region $E_x \approx 7$-$9$ MeV". A careful observation of the total cross section data of Auchampaugh, et al. in Figure 3.12 suggest that the broad resonance at 3.55 MeV neutron energy could be the missing $1^-$ state in question. This possibility is based on the fact that the data of Nelson, et al. appear to be incorrect in both shape and magnitude in this region and that great difficulty was experienced in the present R-matrix analysis in trying to fit the data from 3 to 4 MeV (as well as the data from 4.0 MeV to 4.5 MeV). A broad $1^-$ state in this region would have d-wave strength probably mixed in both d-3/2 and d-5/2 channels and by the sum rules (Bl 52) would be observed in the $B_2$ coefficients thereby perhaps improving the fit from 4.0 MeV to 4.5 MeV in the present data.

On the other side of the question one could equally well ask the origin of a broad $2^-$ state at 2.85 MeV neutron energy since the $2^-$ member of the $[1p_{3/2}^{-1}, 1d_{3/2}]$ multiplet is predicted 2 MeV or so higher. It is important to the development of the nuclear model that properties of states in this region be determined as accurately as possible experimentally. This should serve as strong motivation for a remeasurement of the differential elastic scattering cross section from 2 to 4 MeV neutron energy. From these results it may then be possible to test the model more fully and more critically.

Finally, there exists the question of the energy and ordering of the members of the $[1p_{3/2}^{-1}, 1d_{3/2}]$ multiplet. This ordering, as calculated by Gillet, *et al.*, is shown in Figure 3.19. It is interesting to note that the $3^-$ member of the $[1p_{3/2}^{-1}, 1d_{3/2}]$ multiplet falls within 100 keV of the interference dip caused by the two $3^-$ states in the actual data. Of course, this high in excitation energy one would not expect to observe the pure d-3/2 single particle resonance but instead considerable configuration mixing as evidenced by the equal d-3/2 and d-5/2 reduced width amplitudes used to obtain the best fit in the R-matrix analysis. It is encouraging to note the similarities between the actual data and the calculation of Birkholz, *et al.* in this region. It is clear from Figure 3.20 that the calculated partial cross section for channels with total angular momentum and parity of $3^-$ show the interference effect at approximately 6.25 MeV neutron energy that is seen in the data at approximately 5.5 MeV caused by the interference of two $3^-$ states. Figure 3.21 shows the Legendre

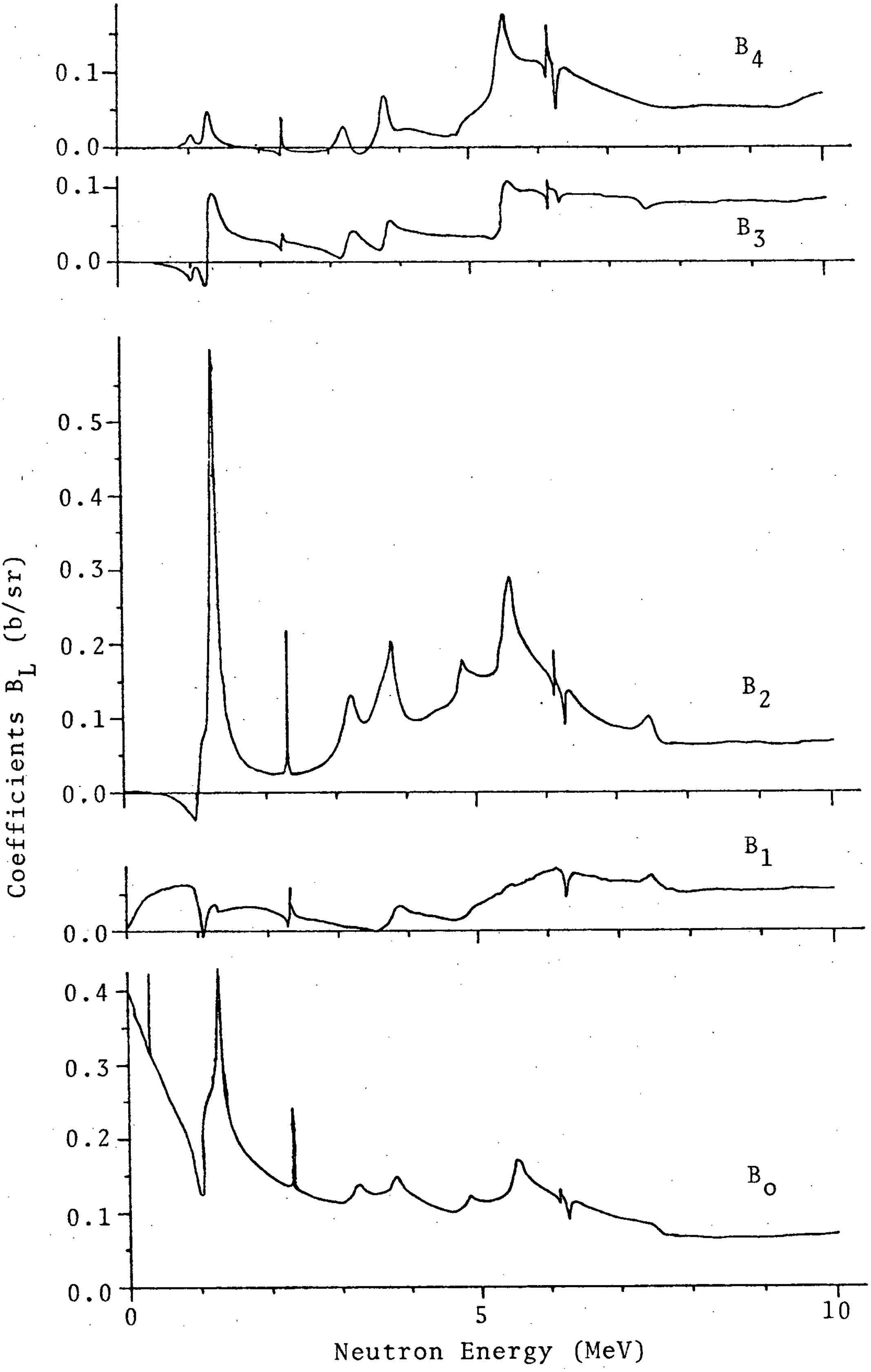

Figure 3.21 Legendre coefficients of the calculated cross sections for neutrons scattered from $^{11}B$ from Reference Bi 74.

expansion coefficients as calculated by Birkholz, et al. The relative agreement of those calculated coefficients, particularly in the $B_3$ and $B_4$ terms, with the present results shown in Figure 3.6 is good. Both structure and reaction theory calculations are very difficult for these light nuclei at excitation energies above the neutron separation energy, and are usually hampered by a lack of experimental measurements of $J^{\pi}$, $E_{\lambda}$, etc. of states for them to use as a guide in fixing values of some of the many parameters of the theory. That, of course, is one of the objectives of this work. It is hoped that the data and analysis in the present work will encourage further theoretical model calculations on this nucleus similar to those already completed by Birkholz and Heil.

# CHAPTER 4

# CONCLUSIONS

The differential elastic scattering cross sections for neutrons scattered from an isotopically enriched sample of $^{11}B$ have been measured for sixty incident neutron energies from 4.00 MeV to 8.00 MeV. These cross sections provide a significant contribution to the neutron data base needed on $^{11}B$ for fusion reactor designs employing boron compounds as shielding material. These cross sections have been measured by a neutron time-of-flight spectrometer system utilizing a computerized data reduction program developed for this experiment which was independent of the usual normalization to some known scattering cross section and which had a determined absolute accuracy of better than 5%. This accuracy was determined by error analysis, measurement of several well-known $^{12}C+n$ cross sections, and numerous remeasurements of both $^{11}B+n$ and known $^{12}C+n$ cross sections in the energy range of interest. While the mathematical error analysis yielded standard deviations of the data, remeasurements of the data and comparison of the $^{12}C+n$ data with other measurements together with the error analysis yielded the absolute errors assigned to the data in Appendix 7.

While considerable resonance structure in the compound nucleus $^{12}B$ was known to exist in the region of the present experiment from total neutron cross section measurements on $^{11}B$, the present measurements represent the first time that data have been obtained from which significant nuclear structure information for $^{12}$B could be derived at these energies. In order to verify nuclear states already assigned and to explore the possibility of new state assignments in $^{12}$B, an R-matrix analysis program was written and used to analyze all the known neutron elastic scattering data for neutron energies of 0.1 MeV to 8 MeV. Further, all known neutron differential elastic scattering data as well as all available total cross section (using an enriched $^{11}$B sample) and inelastic neutron scattering data on $^{11}$B+n was compared to determine, along with the R-matrix analysis, consistency of the data and possible new structure information.

Several conclusions have been drawn from this analysis. First, the neutron differential elastic scattering data of Lane, *et al*. from 0.1 MeV to 2.3 MeV neutron energy is in excellent agreement with recent total cross section measurements of Auchampaugh, *et al*., and further, the present R-matrix analysis using j-j coupling is entirely consistent with the older R-matrix analysis in L-S coupling of Lane, *et al*. The state assignments in this region are therefore considered to be verified and the data are considered to be an accurate representation of the neutron elastic differential scattering cross section in this region.

For the region from 2.0 MeV to 4.0 MeV neutron energy it is concluded that new measurements of the neutron elastic differential scattering cross sections, i.e., remeasurements of the data of Nelson, *et al*., are required. There are several facts to substantiate this conclusion. As discussed in Section 3.5.2, there is a 10% to 15% disagreement in magnitude between the total and integrated elastic cross section in this region. While the first inelastic channel is open here the difference between the total and integrated elastic cross section is an order of magnitude different from several measurements of the inelastic cross section in this region. In the region of overlap with the present measurements, those same data are low in magnitude by 10% to 15%. In the work of Ajzenberg-Selove, et al. (Aj 75) in which the states of $^{12}$B were studied via the $^{9}$Be($^{7}$Li,$\alpha$)$^{12}$B reaction they state: "In the region of overlap with other measurements, principally studies of $^{11}$B+n, the agreement is very good. All the states reported in $^{11}$B+n are observed here with the exception of $^{12}$B*(6.6,6.8). The latter is broad and could have easily been missed above the multiparticle background. It is not clear why $^{12}$B*(6.6) ($J^{\pi}=(1)^{+}$, $\Gamma_{C.M.}=140$ keV) is not populated. A careful search at $\theta_{LAB}=11^{\circ}$ to $41^{\circ}$ reveals no indication of it". It is in this region that significant difficulty existed in trying to fit the data of Nelson, et al. with R-matrix parameters in both that analysis and in the present analysis. In varying R-matrix parameters in the present analysis, it appears there may indeed be negative parity (d-wave) states in this region from 3.0 MeV to 4.0 MeV instead of the presently assigned positive parity (p-wave) states. Further, the $1^{-}$ state previously assigned at Ex=5.8 MeV has been shown in the present work to be fitted better with a $2^-$ assignment, and higher resolution cross section measurements show that this broad resonance is closer to Ex=5.98 MeV than to Ex=5.80 MeV as presently listed in the literature. It is concluded from the present analysis that this state is definitely either $2^-$ or $1^-$, but a definitive assignment to this state as well as the other questions raised herein must await a remeasurement of the neutron elastic differential cross section from 2.0 MeV to 4.0 MeV.

R-matrix analysis of the present data from 4.0 MeV to 8.0 MeV has yielded new definitive assignments of $3^-$ to two states in $^{12}B$ at excitation energies of 8.24 MeV (5.31 MeV neutron energy) and 8.56 MeV (5.66 MeV neutron energy), respectively. The $3^-$ assignments to these two levels explains the prominant dip long seen in the total cross section at 5.5 MeV neutron energy. The resonance observed at 8.73 MeV excitation (5.85 MeV neutron energy) has been tentatively assigned angular momentum and parity of $1^+$ and the resonance observed at 9.07 MeV excitation (6.22 MeV neutron energy) has been assigned a very tentative angular momentum and parity of $2^-$. The possibility exists that the resonance at 9.07 MeV excitation is a composite of two unresolved resonances. In the region from 7.55 MeV to 7.90 MeV excitation (4.55 to 4.95 MeV neutron energy) the resonance structure resolved by the present measurement consisted of states with angular momentum no greater than 2 and only negative parity. This is consistent with what is known in the isobaric analog region of $^{12}C$. A broad resonance centered at 9.8 MeV excitation (7.00 MeV neutron energy) and clearly observed in the even polynomial terms of the Legendre expansion coefficients of the differential cross section has not been observed in the total cross section measurements and little success was achieved in fitting this structure with R-matrix parameters. Whether or not this structure is a composite of several unresolved narrow resonances is not known at this time.

Subtraction of the present integrated elastic data from the total cross section data of Auchampaugh, et al. indicates that there exists resonance structure in the integrated nonelastic cross section (total integrated inelastic cross section below 7.25 MeV neutron energy) above 4.5 MeV neutron energy and that the inelastic cross section beyond this energy is roughly twice that measured from an earlier inelastic measurement at 4.85 MeV by Porter, et al. A comparison of the integrated nonelastic cross section at 7.52 MeV from the present work with that of Hopkins, et al. at 7.55 MeV showed somewhat better agreement with about a 25% difference between the two results. It is clear from the present work that roughly 20% of the total scattering cross section from 4.5 to 8.0 MeV neutron energy consists of inelastic scattering. Because of the significant discrepencies between previously measured inelastic cross sections and the present work and because the inelastic cross sections are important in the use of boron compounds for shielding purposes, new measurements of the inelastic neutron cross section for $^{11}B$ need to be made. While no inelastic channels were considered in the R-matrix analysis (because virtually no inelastic data exists on $^{11}B+n$ at these energies) it is not expected that the basic conclusions of the R-matrix fitting will be affected.

The relative agreement of very difficult shell model calculations on $^{12}B$ up to 10 MeV excitation energy with the neutron scattering data is encouraging. Further accurate neutron scattering data and accompanying R-matrix analysis would be most useful to encourage further model development and calculations of this type. To improve the neutron scattering data base for $^{11}B$ as well as to acquire new nuclear structure parameters for the compound nucleus $^{12}B$ from the corresponding analysis of those data, it is recommended that the first effort in the future be directed toward measurement of the neutron differential elastic scattering cross section from 2.0 MeV to 4.0 MeV neutron energy. From such a measurement, with subsequent comparison of the integrated elastic scattering cross section with available total cross section measurements, an indication of the magnitude of the integrated inelastic cross section from threshold to 4.0 MeV neutron energy could be obtained. This, with the present work, would serve as a guide to further measurement, recommended as the next priority, of the neutron differential inelastic scattering cross sections.

# REFERENCES

Aj 75 F. Ajzenberg-Selove, R. Middleton and J.D. Garrett, Phys. Rev. C 12, 1868 (1975).

Aj 75a F. Ajzenberg-Selove, Nucl. Phys. A248, 1 (1975).

Au 76 G.F. Auchampaugh, S. Plattard, R. Extermann, and C.E. Ragan III, Proc. of the Intl. Conf. on the Interactions of Neutrons with Nuclei, E.R.D.A. CONF-760715-P2, p. 1389; G.F. Auchampaugh, private communication (1976).

Be 69 P.R. Bevington, Data Reduction and Error Analysis for the Physical Sciences, (McGraw-Hill, New York, N.Y., 1969).

Bi 74 J. Burkholz and V. Heil, Nucl. Phys. A225, 429 (1974).

Bl 52 J.M. Blatt and L.C. Biedenharn, Rev. Mod. Phys. 24, 258 (1952).

Bl 52a J.M. Blatt and V.F. Weisskopf, Theoretical Nuclear Physics, (J. Wiley and Sons, Inc., New York, N.Y., 1952).

Ca 59 E.D. Cashwell and C.J. Everett, Monte Carlo Method for Random Walk Problems, (Pergamon Press, New York, 1959).

Ca 71 M. Cance, J. Cabe and M. Labat, Internal Report 07-71 DO.0068, Centre D'Etudes de Bruyeres-Le-Chatel, C.E.A., unpublished, (1971).

Ca 73 J.D. Carlson, Ohio Univ. Gas Target for the Production of Neutrons, unpublished, (1973).

Ca 73a J.D. Carlson, Nucl. Instr. and Meth. 113, 541 (1973).

Co 35 E.U. Condon and G.H. Shortley, Theory of Atomic Spectra, (Cambridge University Press, Cambridge, England, 1935).

Co 67 J.M. Cox and H.D. Knox, Macabre, Ohio Univ., unpublished, (1967).

Cz 64 J.B. Czirr, D.R. Nygren and C.D. Zafiratos, Nucl. Instr. and Meth. 31, 226 (1964).

Fo 61 D.B. Fossan, R.L. Walter, W.E. Wilson and H.H. Barchall, Phys. Rev. 123, 209 (1961).

Ga 72 W. Galati, J.D. Brandenberger and J.L. Weil, Phys. Rev. C 5, 1508 (1972).

Gi 64 V. Gillet and N. Vinh Mau, Nucl. Phys. 54, 321 (1964).

Gu 68 I. Guiasu and F. Stancu, Nuovo Cim. 58, 2 (1968).

Ho 69 J.C. Hopkins and D.M. Drake, Nucl. Sci. and Eng. 36, 275 (1969).

Im 62 W.L. Imhof, R.G. Johnson, F.G. Vaughn and M. Walt, Phys. Rev. 125, 1334 (1962).

La 58 A.M. Lane and R.G. Thomas, Rev. Mod. Phys. 30, 257 (1958).

La 70 R.O. Lane, C.E. Nelson, J.L. Adams, J.E. Monahan, A.J. Elwyn, F.P. Mooring and A. Langsdorf, Jr., Phys. Rev. C 2, 2097 (1970).

La 72 R.O. Lane, private communication from R.E. Coles (1972).

Li 61 D.A. Lind and R.B. Day, Annals of Phys. 12, 485 (1961).

Li 73 H. Liskien and A. Paulsen, Nuclear Data Tables 11, 569 (1973).

Li 75 D.A. Lind, R.F. Bentley, J.D. Carlson, S.D. Schery and C.D. Zafiratos, Nucl. Instr. and Meth. 130, 93 (1975).

Ma 70 T.G. Masterson, Nucl. Instr. and Meth. 88, 61 (1970).

Ma 76 C.F. Maguire, D.L. Hendrie, D.K. Scott, J. Mahoney and F. Ajzenberg-Selove, Phys. Rev. C 13, 933 (1976).

Mc 72 D.K. McDaniels, I. Bergquist, D. Drake and J.T. Martin, Nucl. Instr. and Meth. 99, 77 (1972).

Mc 72a D.K. McDaniels, M. Drosg, J.C. Hopkins, and J.D. Seagrave, Phys. Rev. C 6, 1593 (1972).

Mo 50 J.E. Monahan, Formal Theory of Scattering, Argonne National Laboratory, unpublished, (1950).

Mo 71 J.E. Monahan, H.T. Fortune, C.M. Vincent and R.E. Segel, Phys. Rev. C 3, 2192 (1971).

Mo 76 J.E. Monahan, private communication (1976).

Ne 73 C.E. Nelson, S.L. Hausladen and R.O. Lane, Nucl. Phys. *A217*, 546 (1973).

Pa 56 S.P. Pandya, Phys. Rev. *103*, 956 (1956).

Pe 60 J.E. Perry,Jr., E. Haddad, R.L. Henkel, G.A. Jarvis and R.J. Smith (unpublished), Reported by J.D. Seagrave, at the Conf. on Nuclear Forces and the Few-Nucleon Problem, London, 1959 (Pergamon Press, New York, 1960), data from G. Hale, private communication (1975).

Pe 69 F.G. Perey and W.E. Kinney, ORNL Report No. 4441, Oak Ridge National Laboratory, unpublished, (1969).

Po 70 D. Porter, R.E. Coles and K. Wyld, AWRE Report No. 045/70, U.K.A.E.A., A.W.R.E., Aldermaston, England, unpublished, (1970).

Ra 42 G. Racah, Phys. Rev. *61*, 186 (1942); *62*, 438 (1942).

Ro 57 M.E. Rose, *Elementary Theory of Angular Momentum*, (J. Wiley and Sons, Inc., New York, 1957).

Sh 63 A. deShalit and I. Talmi, *Nuclear Shell Theory*, (Academic Press, New York and London, 1963).

Sm 75 A.B. Smith, private communication (1975).

Tw 76 B.G. Twining, U.S. E.R.D.A. Nuclear Data Committee Meeting, unpublished, (May 1976).

Vo 59 E. Vogt, in *Nuclear Reactions*, edited by P.M. Endt and M. Demear (Interscience Publishers, Inc., New York, 1959), Vol. I.

Vo 62 E. Vogt, Rev. Mod. Phys. *34*, 723 (1962).

We 71 G.D. Westin and J.L. Adams, Phys. Rev. C *4*, 363 (1971).

Wi 63 H.B. Willard, L.C. Biedenharn, P. Huber and E. Baumgartner, in *Fast Neutron Physics Part II*, edited by J.B. Marion and J.L. Fowler (Interscience Publishers, Inc., New York, 1963).

# APPENDIX 1

# FINITE GEOMETRY EFFECTS

We consider here the finite geometry effects not discussed in Chapter 2. These effects derive from the finite-sized neutron source (gas cell) and the (relatively) large scattering sample. These effects cause an increase in the energy spread of the neutron time-of-flight pulse, an anisotropy of the incident neutron intensity on the face of the sample, and an increase in the angular spread about the scattering angle θ as shown in the following exaggerated diagram:

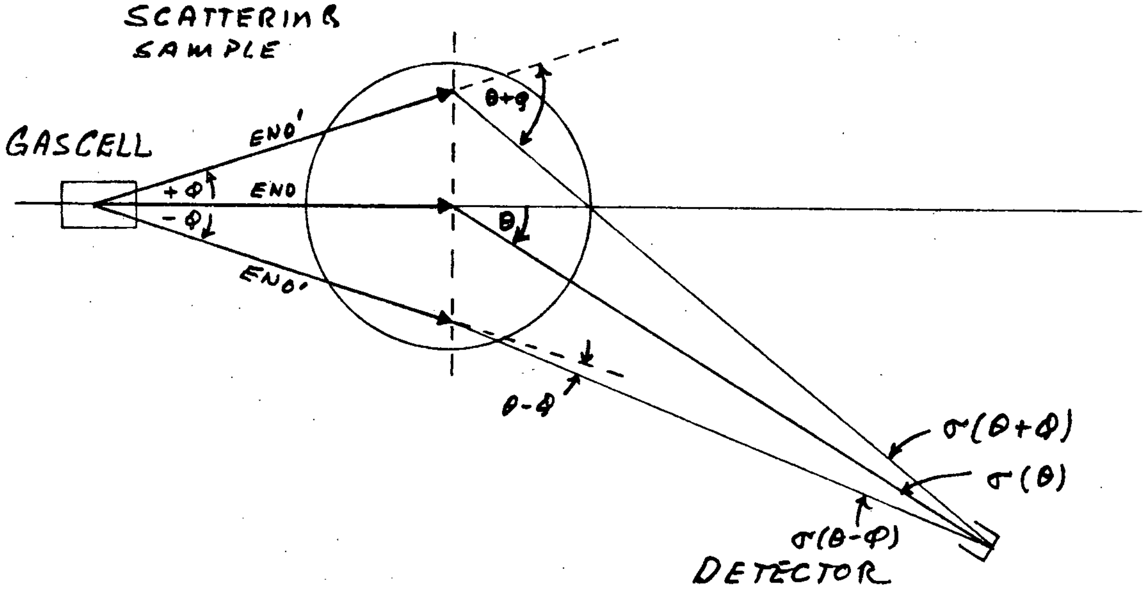

ENO is the zero degree neutron energy and ENO' is the neutron energy at angle ϕ. The average angular spread in this experimental set-up is approximately ±3.5°. This is based on the assumption that the full width at half maximum or average angular resolution is approximately half the maximum possible angular deviation obtained from the dimensions of the scattering sample, the source-to-sample distance, the detector size, and the sample-to-detector distance. While this is a relatively large spread, experimental factors dictated this geometry and for the cross sections measured in this experiment this spread in angle has little effect on the data as is discussed below.

From the kinematics of the T(p,n)$^3$He reaction the neutron energy may be calculated for $\phi=3.5^\circ$ and compared to the energy at $\phi=0^\circ$ to obtain the average energy spread caused by the finite geometry of the source and sample. The average spread in energy throughout the neutron energy range in this experiment was approximately ±9 keV. This is to be compared with the ±20 keV to ±30 keV absolute spread caused by the proton energy loss in the gas cell and therefore, does not significantly increase the width of the neutron pulses.

Using the Legendre expansion coefficients of the differential cross sections for the T(p,n)$^3$He reaction from reference Li 73, the cross sections for angles between 0° and 3.5° may be calculated. The change in the differential cross section for this reaction is very small (less than 1%) up to 4°. The neutron flux from the source is, of course, proportional to this cross section and therefore the flux change is also small to 4°. Therefore, the intensity in neutrons/cm$^2$ on the sample is essentially uniform and no correction for nonuniformity of the incident neutron intensity was made.

Finally, the effect of the ±3.5° average angular spread on the value of $\sigma(\theta)$ must be considered. The effect of this angular spread might be significant only where the differential cross section is rapidly varying and for the present data that occurs only for the first two or three angles at most (see Figure 2.19). Consider the following diagram where the angular resolution of the experimental set-up is $\theta \pm \Delta\theta$:

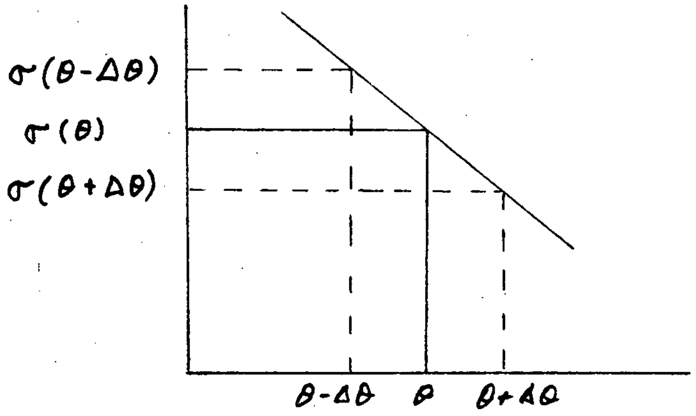

The following question arises: for a specified angle $\theta$ (with angular resolution $\pm\Delta\theta$) by how much does the measured cross section $\underset{MEAS}{\sigma(\theta\pm\Delta\theta)}$ differ from $\underset{TRUE}{\sigma(\theta)}$ ? It can be seen from the diagram above that if the cross section is linear in the interval $\theta-\Delta\theta$ to $\theta+\Delta\theta$ then the mean value measured for the cross section will in fact be the same as the true value at angle $\theta$. For the cross section data measured in this experiment, the linearity of the cross sections over ±5° for the first three angle measurements of all angular distributions varied no more than 1% from a straight line. This was verified for the data in Appendix 7 by using the Legendre expansion coefficients in Appendix 8 to expand the cross sections around the first three angles of each angular distribution for each degree up to ±5°, and then comparing the average of these cross sections with the mean cross section measured in the experiment. The results agreed in all cases to better than 1%. Therefore, no further corrections, other than those already discussed in Chapter 2, were made to the data of Appendix 7.

# APPENDIX 2

# CHARGE NORMALIZATION

As discussed in Chapter 2 on the data reduction scheme, the relative efficiency runs were charge normalized. The charge normalization was carried out by a very accurate and sophisticated beam-current-integrator (BCI) designed and constructed by R. L. Young, formerly of this laboratory. The accuracy of the current integration was completely insensitive to accelerator tuning and beam focusing. Consider the following diagram of the gas cell apparatus:

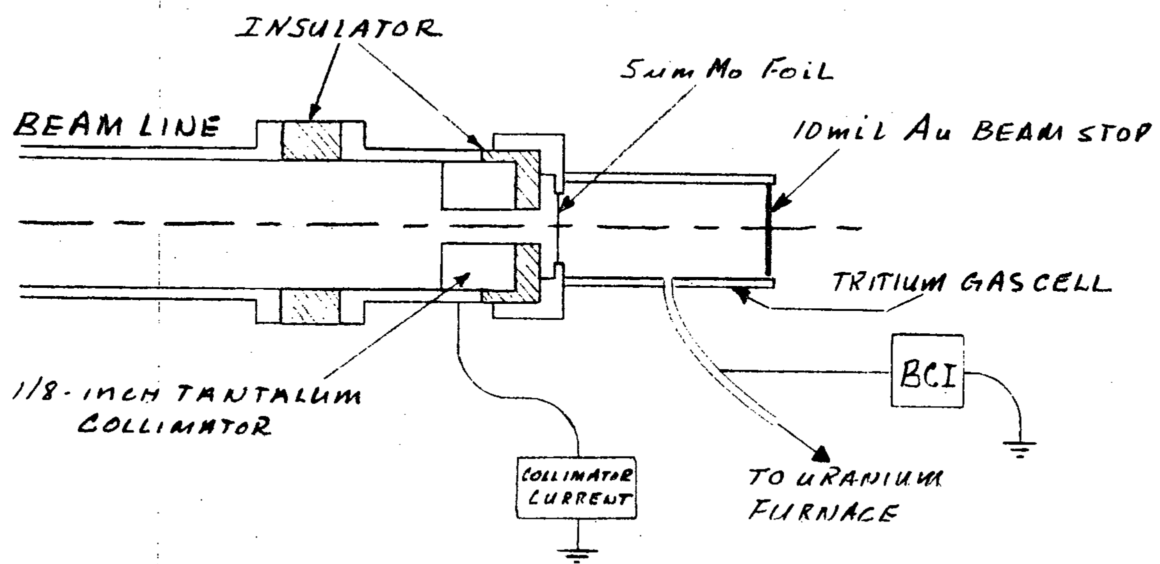

[NOT TO SCALE - ELECTRON SUPPRESSION RING FOR GAS CELL NOT SHOWN]

This diagram is intended to show schematically how the charge collection operated. The 1/8-inch collimator was such that all protons in the incident beam passing through the collimator were collected irrespective of the focusing conditions of the beam leg. As can be seen from Figure 2.4, the gas cell was cooled by a jet spray of air and water. Measures were taken to keep all apparatus except the actual gas cell dry. Leakage current between the gas cell and supporting apparatus was held to less than 0.1 nanoampere, with the jet spray working and a 300 volt potential on the electron suppression ring. Many tests were performed to measure the detector and monitor counts vs. accumulated charge for various modes of beam tuning, focusing and defocusing, and varying currents. In no mode of operation could the ratio of detector or monitor counts to accumulated charge be affected. Of course, considerable effort was expended during the relative efficiency measurements to make sure that the beam was in a well focused, stable mode. It is important to note that even though the beam-current-integrator is definitely accurate enough to do absolute charge normalization, it is only necessary for the data analysis scheme used in this experiment to be able to do relative charge normalization. That is, a leakage current or other difficulty which was consistent throughout the relative efficiency measurement would not affect the accuracy of the result.

For the relative efficiency measurements, the following table gives a random sampling of detector and monitor counts vs. an accumulated charge of 0.2 millicoulombs in each case. Each run was repeated at least three times and the on-line relative efficiency program then took a simple average of the detector (and monitor) counts for each energy (to be used in the on-line data reduction program).

DATA FROM JAN. 76 HIGH ENERGY RELATIVE EFFICIENCY MEASUREMENT

| Detector Neutron Energy | Counts | Monitor Neutron Energy | Counts |
|---|---|---|---|
| 4.335 MeV | 80906 | 4.040 MeV | 27583 |
| | 81103 | | 27592 |
| | 80238 | | 27903 |
| | 80276 | | 27875 |
| 5.407 MeV | 55794 | 5.047 MeV | 20405 |
| | 55553 | | 19989 |
| | 55685 | | 20135 |
| | 56160 | | 20336 |
| 6.323 MeV | 40900 | 5.907 MeV | 14990 |
| | 40923 | | 15169 |
| | 41009 | | 15100 |
| | 41326 | | 15040 |
| 7.388 MeV | 30707 | 6.907 MeV | 11097 |
| | 30512 | | 10914 |
| | 30590 | | 11041 |
| | 30625 | | 10845 |
| 7.994 MeV | 27506 | 7.457 MeV | 8571 |
| | 27324 | | 8694 |
| | 26947 | | 8737 |
| | 26888 | | 8613 |

The values in this table are consistent with all relative efficiency measurements and it is clear that the one percent error assigned to charge normalization in Section 2.5 is conservative.

# APPENDIX 3

# GAS CELL HEATING EFFECTS

The scheme for data reduction requires that the number of tritium nuclei per cm$^2$, $n_s$ of Section 2.2. remains constant during the relative efficiency measurement. The reader is referred to reference Mc 72 for an experiment performed on beam heating in gas targets at Los Alamos Scientific Laboratory. Basically, let us assume the initial gas pressure and temperature to be $P_o$ and $T_o$ respectively. We designate the gas cell volume by $V_T$ and that of the external reservoir $V_o$. Assuming an ideal gas we have:

$$\frac{P_o V_T}{T_o} + \frac{P_o V_o}{T_o} = k(N_T + N_o) \qquad (1)$$

where k is Boltzmann's constant and $N_T$ and $N_o$ are the number of molecules initially enclosed in the cell and external reservoir respectively. As the beam heats the gas in the cell the pressure will increase and we may write:

$$\frac{P V_T}{T} + \frac{P V_o}{T_o} = k(N_T + N_o) \qquad (2)$$

But

$$\frac{P V_T}{T} = k N_{T'} \qquad (3)$$

where $N_{T'}$ is the number of molecules in the cell at temperature T. Using (3) in (2) yields:

$$k N_{T'} + \frac{P V_o}{T_o} = k(N_T + N_o) \qquad (4)$$

Rewriting (1) gives:

$$\frac{P_o V_T}{T_o} = k\left(N_T + N_o\right) - \frac{P_o V_o}{T_o} \tag{5}$$

Rewriting (4) gives:

$$\frac{P V_o}{T_o} = k\left(N_T + N_o\right) - kN_{T'} \tag{6}$$

Subtracting (1) from (6) gives:

$$(P - P_o)\frac{V_o}{T_o} = \frac{P_o V_T}{T_o} - kN_{T'} \tag{7}$$

Multiplying (7) by $T_o/P_o\ V_T$ gives:

$$\left(\frac{P - P_o}{P_o}\right)\frac{V_o}{V_T} = 1 - \frac{kN_{T'}T_o}{P_o\ V_T} \tag{8}$$

But:

$$\frac{P_o V_T}{kT_o} = N_T$$

Therefore:

$$\frac{N_{T'}}{N_T} = 1 - \frac{V_o}{V_T}\frac{\Delta P}{P_o} \tag{9}$$

where

$$\Delta P = (P - P_o)$$

Equation (9) has been verified experimentally (Mc 72) and we see that if the change in pressure, $\Delta P$, is zero, then $N_{T'} = N_T$. It should be understood that this does not mean for beam-on and beam-off conditions but that the pressure must not be allowed to vary during beam-on conditions during the relative efficiency measurement. The pressure was monitored by a Wallace and Tiernan differential pressure gauge with a sensitivity of 0.06 psi. It was never observed to vary during the relative efficiency measurements mainly because the cooling spray mixture of air and water was very efficient at removing the heat from the gold beam stop.

In the error analysis, a 0.06 psi change was assumed even though the consistency of remeasurements of the differential cross section indicated that the pressure did not actually vary 0.06 psi during the relative efficiency measurements. Therefore, the three percent uncertainty assigned to this term in the error analysis section is very conservative.

# APPENDIX 4

## TRITIUM (p,n) ZERO DEGREE SHAPE

The data reduction scheme utilized in this experiment requires a knowledge of the shape of the T(p,n)$^3$He zero degree cross section. This requirement follows from the necessity to calculate the ratio

$$\sigma_{T(p,n)}(0°, EP')/\sigma_{T(p,n)}(0°, EP)$$

in Eq. (2-19). The data from several experiments (Pe 60, Mc 72a) and an evaluated data set (Li 73) were compared with the results plotted on the following page. The curves through the various data sets are drawn only to guide the eye. While there exists small normalization differences between the data sets, it can be seen that the overall shape agreement is quite good. The data set used for the actual calculation was from reference Li 73. The required ratio above calculated from any of the data sets gives the same results to one percent or less, justifying that value for the assigned uncertainty in Section 2.5.

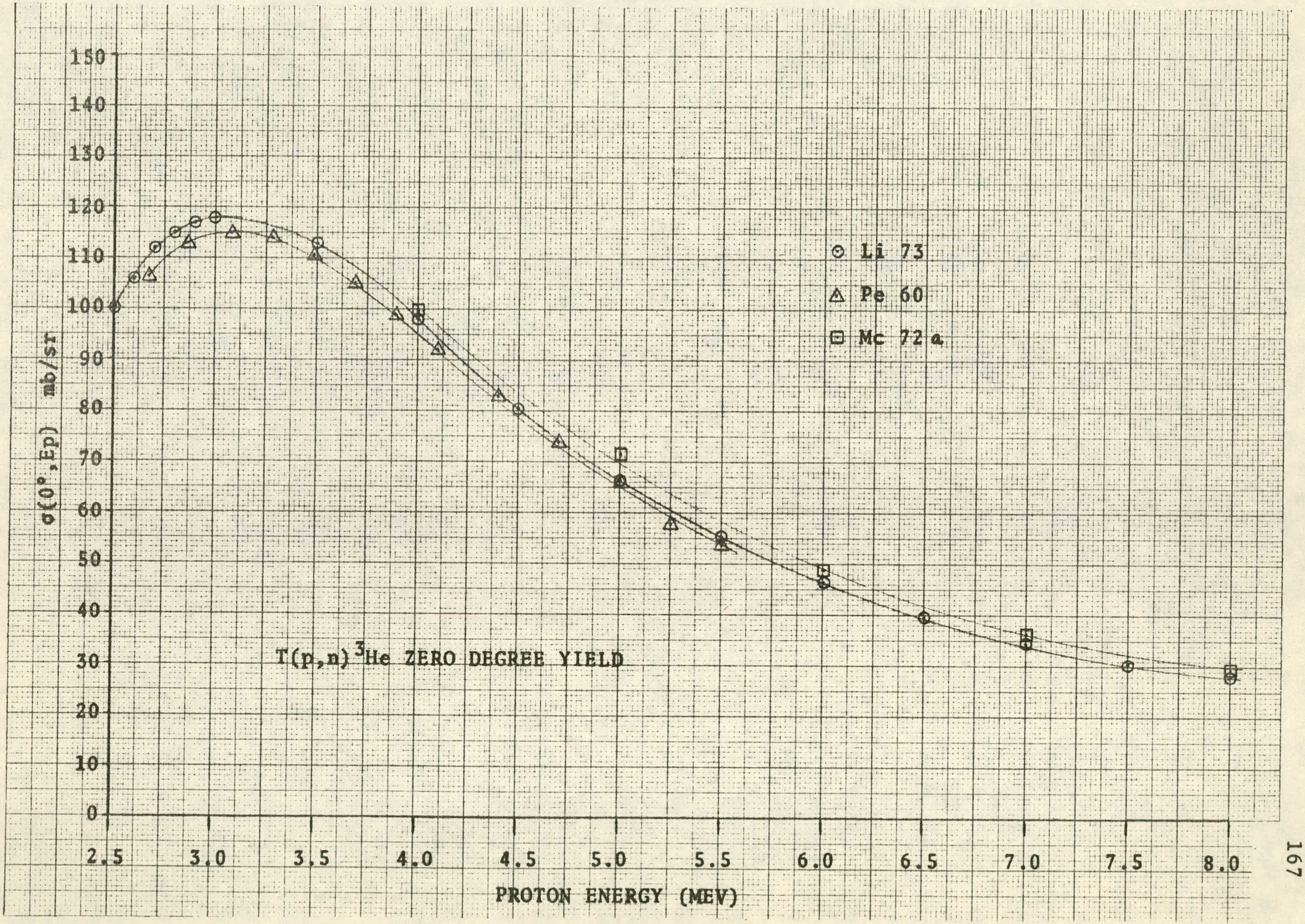

150
140
130
120
110
100
90
80
70
60
50
40
30
20
10
0
σ(0°,Ep) mb/sr
⊙ Li 73
△ Pe 60
⊡ Mc 72 a
T(p,n)$^3$He ZERO DEGREE YIELD
2.5
3.0
3.5
4.0
4.5
5.0
5.5
6.0
6.5
7.0
7.5
8.0
PROTON ENERGY (MEV)

# APPENDIX 5

## GENERAL SCATTERING FORMALISM (j-j coupling)

This development in j-j coupling will essentially parallel that of Section 3.1.2 and the reader is referred to Sections 3.1.1 and 3.1.2 for an explanation of the terms used in this Appendix. The most general form of the total wave function will consist, at sufficiently large distances, of the superposition of ingoing and outgoing spherical waves as follows:

$$\Psi^{m_s m_I}_{TOTAL} \simeq \frac{1}{r v^{1/2}} \sum_{J l j} \left( A^{JM}_{lj} e^{-i(kr - l\pi/2)} - B^{JM}_{lj} e^{+i(kr - l\pi/2)} \right) |JMjI\rangle \qquad (1)$$

where

$$B^{JM}_{l'j'} = \sum_{lj} S^{J}_{l'j',lj} A^{JM}_{lj} \qquad (2)$$

For purposes of this derivation we shall specify the projection spins $m_s$ and $m_I$ in the incident channel. Proper summing over these quantum numbers will be carried out later on. We may write for the incident plane wave:

$$\Psi^{m_s m_I}_{inc} = e^{ikz} |s m_s\rangle |I m_I\rangle \qquad (3)$$

We utilize the common procedure of expanding this plane wave into a series of partial waves, i.e.,

$$\Psi^{m_s m_I}_{inc} = (4\pi)^{1/2} \sum_{l=0}^{\infty} i^l (2l+1)^{1/2} j_l(kr) |l0\rangle |s m_s\rangle |I m_I\rangle \qquad (4)$$

Proceeding in a fashion similar to Section 3.1.2 we may write:

$$\Psi^{m_s m_I}_{inc} \simeq \frac{i(\pi)^{1/2}}{kr} \sum_{J l j} i^l (2l+1)^{1/2} (l s 0 m_s | j m_s)(j I m_s m_I | J M) \times \left( e^{-i(kr - l\pi/2)} - e^{+i(kr - l\pi/2)} \right) |JMjI\rangle \qquad (5)$$

If (1) and (5) are written with primed quantities $l'$ and $j'$, a comparison of the ingoing parts of (1) and (5) yields:

$$A^{JM}_{l'j'} = \frac{i(\pi v)^{1/2}}{k}(l' s o m_s | j' m_s)(j' I m_s m_I | JM)\, i^{l'}(2l'+1)^{1/2} \qquad (6)$$

and from (2) that:

$$B^{JM}_{l'j'} = \frac{i(\pi v)^{1/2}}{k}\sum_{l_j} S^{J}_{l'_{j'}; l_j}(l s o m_s | j m_s)(j I m_s m_I | JM)\, i^{l}(2l+1)^{1/2} \qquad (7)$$

Rewriting (1) with (6) and (7) yields:

$$\Psi^{m_s m_I}_{TOTAL} \simeq \frac{i(\pi)^{1/2}}{kr}\Big\{\sum_{J l' j'} i^{l'}(2l'+1)^{1/2}(l' s o m_s | j' m_s)(j' I m_s m_I | JM)\, e^{-i(kr - l'\pi/2)} \times |JM j' I\rangle$$

$$- \sum_{J l_j l'_{j'}} S^{J}_{l'_{j'}; l_j}\, i^{l}(2l+1)^{1/2}(l s o m_s | j m_s)(j I m_s m_I | JM)\, e^{+i(kr - l'\pi/2)} \times |JM j' I\rangle\Big\} \qquad (8)$$

Since the first part of (8) is identical with (5), adding and subtracting the following

$$\frac{i(\pi)^{1/2}}{kr}\sum_{J l' j'} i^{l'}(2l'+1)^{1/2}(l' s o m_s | j' m_s)(j' I m_s m_I | JM)\, e^{+i(kr - l'\pi/2)} \times |JM j' I\rangle$$

to (8) yields $\Psi^{m_s m_I}_{TOTAL} = \Psi^{m_s m_I}_{inc} + \Psi^{m_s m_I}_{scatt}$, or that

$$\Psi^{m_s m_I}_{SCATT} = \frac{i(\pi)^{1/2}}{kr}\Big\{\sum_{J l' j'} i^{l'}(2l'+1)^{1/2}(l' s o m_s | j' m_s)(j' I m_s m_I | JM)\, e^{+i(kr - l'\pi/2)} \times |JM j' I\rangle$$

$$- \sum_{J l_j l'_{j'}} S^{J}_{l'_{j'}; l_j}\, i^{l}(2l+1)^{1/2}(l s o m_s | j m_s)(j I m_s m_I | JM)\, e^{+i(kr - l'\pi/2)} \times |JM j' I\rangle\Big\} \qquad (9)$$

Recognizing that we can write

$$i^{l'}(2l'+1)^{1/2}(l' s o m_s | j' m_s)(j' I m_s m_I | JM) =$$

$$\sum_{l_j} i^{l}(2l+1)^{1/2}(l s o m_s | j m_s)(j I m_s m_I | JM)\, \delta_{l l'}\, \delta_{j j'}$$

we may write (9) (after factoring out common parts):

$$\psi_{SCATT}^{m_s m_s} = \frac{i(\pi)^{1/2}}{kr} \sum_{J\ell_j \ell'_{j'}} i^{\ell}(2\ell+1)^{1/2} (\ell s 0 m_s | j m_s)(j I m_s m_I | JM)$$

$$\times \left\{ \delta_{\ell\ell'} \delta_{jj'} - S^{J}_{\ell'_{j'}, \ell_j} \right\} e^{+i(kr - \ell'\pi/2)} \times |JMj'I\rangle \qquad (10)$$

Using the fact that $e^{-i\ell'\pi/2} = i^{-\ell'}$ and that the decomposition of $|JMj'I\rangle$ is

$$|JM_{j'}I\rangle = \sum_{m_s' m_I'} (\ell' s m_\ell' m_s' | j' m_j')(j' I m_j' m_I' | JM) |\ell m_\ell'\rangle |s m_s'\rangle |I m_I'\rangle$$

we may write for (10):

$$\psi_{SCATT}^{m_s m_I} = \frac{e^{ikr}}{r} \sum_{m_s' m_I'} f^{m_s m_s', m_I m_I'}(\theta, \phi) \, |s m_s'\rangle |I m_I'\rangle$$

where

$$f^{m_s m_s', m_I m_I'}(\theta, \phi) = \frac{i(\pi)^{1/2}}{k} \sum_{J\ell_j \ell'_{j'}} i^{\ell-\ell'}(2\ell+1)^{1/2} (\ell s 0 m_s | j m_s)(j I m_s m_I | JM)$$

$$\times (j' I m_j' m_I' | JM)(\ell' s m_\ell' m_s' | j' m_j')(\delta_{\ell\ell'} \delta_{jj'} - S^{J}_{\ell'_{j'}, \ell_j}) Y_{\ell'}^{m_\ell'}(\theta\phi) \qquad (11)$$

Eq. (11) represents the final expression for the scattering factor in j-j coupling. Finally, since our detector is not sensitive to spin projections we average over the incident projections and sum over the outgoing projections to get:

$$d\sigma = \frac{1}{(2s+1)(2I+1)} \sum_{m_s m_s' m_I m_I'} \left| f^{m_s m_s', m_I m_I'}(\theta, \phi) \right|^2 d\Omega \qquad (12)$$

For any two scattering amplitudes having all their spin projections reversed in sign, by Clebsch-Gordan coefficients and spherical harmonic properties, one can show that:

$$f^{-m_s, -m_s', -m_I, -m_I'}(\theta, \phi) = e^{-2i m_\ell' \phi} (-1)^{m_\ell'} f^{m_s m_s' m_I m_I'}(\theta, \phi)$$

where $m_\ell' = m_s + m_I - m_s' - m_I'$ and therefore, we can write:

$$\left| f^{-m_s, -m_s', -m_I, -m_I'}(\theta, \varphi) \right|^2 = \left| f^{m_s m_s' m_I m_I'}(\theta, \varphi) \right|^2$$

Utilizing these expressions reduces the number of terms in the sum (12) by a factor of two.

## APPENDIX 6

## DERIVATION OF R-MATRIX SURFACE TERMS

For a free particle wave function V = 0 (for neutrons) and we may write:

$$\hat{H}\Psi = E\Psi ,$$

where:

$$\hat{H} = -\frac{\hbar^2}{2M_c}\nabla_c^2 = -\frac{\hbar^2}{2M_c}\frac{1}{r_c^2}\frac{\partial}{\partial r_c}\left(r_c^2\frac{\partial}{\partial r_c}\right) - \frac{\hbar^2}{2M_c r_c}\hat{\Lambda} .$$

If we write:

$$\Psi = R_\ell(r)\,Y_\ell^m(\Omega) \;\&\; \hat{L}^2 Y_\ell^m(\Omega) = -\hbar^2\hat{\Lambda}\,Y_\ell^m(\Omega) = \ell(\ell+1)\hbar^2 Y_\ell^m(\Omega),$$

then:

$$-\frac{\hbar^2}{2M_c}\frac{1}{r^2}\frac{\partial}{\partial r}\left(r^2\frac{\partial R_\ell(r)}{\partial r}\right) + \frac{\ell(\ell+1)\hbar^2 R_\ell(r)}{2M_c r^2} = E R_\ell(r) \quad \underline{\underline{\text{OR}}}$$

$$\frac{1}{r^2}\frac{\partial}{\partial r}\left(r^2\frac{\partial R_\ell(r)}{\partial r}\right) - \frac{\ell(\ell+1)}{r^2}R_\ell(r) + k^2 R_\ell(r) = 0 ,$$

where:

$$k^2 = \frac{2mE}{\hbar^2} .$$

Then:

$$\left(\frac{d^2}{dr^2} + \frac{2}{r}\frac{d}{dr} + k^2 - \frac{\ell(\ell+1)}{r^2}\right)R_\ell(r) = 0 .$$

If we let $\rho = kr$ we have Bessel's equation:

$$\frac{d^2 R_\ell(\rho)}{d\rho^2} + \frac{2}{\rho}\frac{dR_\ell(\rho)}{d\rho} + \left(1 - \frac{\ell(\ell+1)}{\rho^2}\right)R_\ell(\rho) = 0,$$

the linearly independent solutions of which are (for $r \to \infty$):

$$j_\ell(\rho) \longrightarrow \frac{1}{\rho}\cos\left(\rho - \frac{\pi}{2}(\ell+1)\right)$$

$$n_\ell(\rho) \longrightarrow \frac{1}{\rho}\sin\left(\rho - \frac{\pi}{2}(\ell+1)\right)$$

or combinations thereof, i.e.,

$$h_\ell^{\pm}(\rho) = j_\ell(\rho) \pm i n_\ell(\rho) \rightarrow \frac{1}{\rho} e^{\pm i(\rho - \pi/2(\ell+1))}$$

We choose our $I_\ell(\rho)$ and $O_\ell(\rho)$ solutions as:

$$I_\ell(\rho) = -i\rho h^{-}(\rho) = -i\rho(j_\ell(\rho) - i n_\ell(\rho))$$

$$O_\ell(\rho) = i\rho h^{+}(\rho) = i\rho(j_\ell(\rho) + i n_\ell(\rho))$$

Regular and irregular solutions are chosen as follows:

$$F_\ell(\rho) = \rho j_\ell(\rho) \quad \underline{\text{and}} \quad G_\ell(\rho) = -\rho n_\ell(\rho)$$

Then it is obvious that:

$$I_\ell(\rho) = G_\ell - i F_\ell$$

$$O_\ell(\rho) = G_\ell + i F_\ell$$

$$L_c \equiv (\rho O'/O)_c = S_c + i P_c$$

$$= \rho \frac{G_\ell' + i F_\ell'}{G_\ell + i F_\ell}$$

$$= \rho\left(\frac{G_\ell' G_\ell + F_\ell' F_\ell}{A_\ell^2} + i\left(\frac{F_\ell' G_\ell - F_\ell G_\ell'}{A_\ell^2}\right)\right)$$

where:

$$G_\ell + i F_\ell = A_\ell e^{i\phi_\ell}$$

Then:

$$\mathcal{S}_c^+ = \left[\frac{\rho(G_\ell G_\ell' + F_\ell F_\ell')}{A_\ell^2}\right]_c$$

$$P_c^+ = \left[\rho/A_\ell^2\right] \quad \text{i.e.,} \quad F_\ell' G_\ell - F_\ell G_\ell' = 1$$

where (+) stands for positive energy solutions. Further,

$$\Omega_c = (I/O)_c^{1/2} = \left(\frac{G_\ell - iF_\ell}{G_\ell + iF_\ell}\right)^{1/2} = \left(\frac{A_\ell e^{-i\phi_\ell}}{A_\ell e^{+i\phi_\ell}}\right)^{1/2}$$
$$= e^{-i\phi_\ell}$$

It can be shown (Mo 50) that:

$$P_\ell = \rho/A_\ell^2 \ , \ \mathcal{S}_\ell = \frac{\rho}{2A_\ell^2}\frac{dA_\ell^2}{d\rho} \quad \underline{\text{and}}$$

$$A_\ell^2 \frac{d\phi_\ell}{d\rho} = 1 \ \underline{\underline{\text{or}}} \ \phi_\ell(\rho) = \int_0^\rho A_\ell^{-2}\, d\rho$$

where:

$$A_\ell^2(\rho) = \sum_{\alpha=0}^{\ell} \frac{(\ell+\alpha)!\,(2\alpha)!}{(\alpha!)^2(\ell-\alpha)!\,(2\rho)^{2\alpha}}$$

Then:

$$\phi_0(\rho) = \rho$$

$$\phi_1(\varphi) = \rho - \mathrm{TAN}^{-1}(\rho)$$

$$\phi_2(\rho) = \rho - \mathrm{TAN}^{-1}\left(\frac{3\rho}{3-\rho^2}\right)$$

$$P_0 = \rho \qquad \underline{\text{and}} \qquad \mathcal{S}_0 = 0$$

$$P_1 = \rho^3/\rho^2+1 \qquad \mathcal{S}_1 = -\frac{1}{\rho^2+1}$$

$$P_2 = \frac{\rho^5}{\rho^4+3\rho^2+9} \qquad \mathcal{S}_2 = -\frac{3\rho^2+18}{\rho^4+3\rho^2+9}$$

If we consider only orbital angular momentum values $\ell = 0, 1$, and 2 we have, for example, for the matrices $\mathbb{\Omega}$, $\mathbb{P}$, and $\mathbb{L}^{\circ}$, for $^{11}B + n$ and $J^{\pi} = 1^{-}$ the following:

$$\Omega_c = \begin{pmatrix} e^{-i\phi_0} & 0 & 0 \\ 0 & e^{-i\phi_2} & 0 \\ 0 & 0 & e^{-i\phi_2} \end{pmatrix}$$

$$P_c^{1/2} = \begin{pmatrix} P_0^{1/2} & 0 & 0 \\ 0 & P_2^{1/2} & 0 \\ 0 & 0 & P_2^{1/2} \end{pmatrix} \quad \underline{\text{AND}}$$

$$L_c^{\circ} = \begin{pmatrix} S_0 - b_0 + iP_0 & 0 & 0 \\ 0 & S_2 - b_2 + iP_2 & 0 \\ 0 & 0 & S_2 - b_2 + iP_2 \end{pmatrix}$$

# APPENDIX 7

# TABULAR DATA OF DIFFERENTIAL CROSS SECTIONS

## 11B + N
## CROSS SECTIONS AND ERRORS, C.M. (MB/SR)

| ENERGY LAB (MEV) | ANGLE, C.M. (DEG) | | | | | | | | |
|---|---|---|---|---|---|---|---|---|---|
| | 21.8 | 40.7 | 59.3 | 77.5 | 95.2 | 112.5 | 129.3 | 145.7 | 161.8 |
| 4.00 | 312.1 | 220.2 | 124.5 | 58.1 | 41.5 | 54.5 | 83.1 | 105.8 | 114.9 |
| | 13.7 | 9.7 | 5.8 | 2.7 | 1.8 | 2.5 | 3.8 | 4.7 | 5.5 |
| 4.08 | 265.1 | 175.3 | 95.3 | 51.4 | 40.7 | 52.8 | 79.4 | 101.7 | 116.5 |
| | 11.6 | 7.7 | 4.4 | 2.4 | 1.8 | 2.4 | 3.6 | 4.5 | 5.6 |
| 4.10 | 262.6 | 181.0 | 99.0 | 48.8 | 39.0 | 53.4 | 77.1 | 105.4 | 118.2 |
| | 11.2 | 7.8 | 4.4 | 2.2 | 1.8 | 2.3 | 3.5 | 4.7 | 5.7 |
| 4.21 | 256.8 | 176.0 | 97.3 | 46.1 | 36.4 | 53.1 | 87.9 | 121.8 | 139.1 |
| | 11.1 | 7.7 | 4.3 | 2.2 | 1.6 | 2.4 | 3.8 | 5.4 | 6.6 |
| 4.31 | 253.0 | 172.1 | 86.9 | 43.8 | 37.7 | 57.0 | 94.6 | 135.3 | 159.8 |
| | 10.8 | 7.5 | 3.9 | 2.0 | 1.7 | 2.5 | 4.1 | 6.0 | 7.5 |
| 4.41 | 256.5 | 175.4 | 89.3 | 44.1 | 36.3 | 57.0 | 96.3 | 141.3 | 169.7 |
| | 10.8 | 7.6 | 4.0 | 2.0 | 1.6 | 2.5 | 4.3 | 6.2 | 7.9 |
| 4.52 | 269.4 | 181.6 | 91.0 | 44.2 | 40.0 | 64.4 | 101.7 | 148.7 | 177.8 |
| | 11.3 | 7.8 | 4.1 | 2.1 | 1.7 | 2.8 | 4.6 | 6.6 | 8.3 |
| 4.57 | 306.1 | 191.0 | 99.2 | 52.7 | 40.0 | 58.1 | 101.7 | 147.6 | 186.1 |
| | 12.7 | 8.3 | 4.5 | 2.5 | 1.9 | 2.6 | 4.6 | 6.7 | 8.8 |
| 4.62 | 322.7 | 205.4 | 109.9 | 56.5 | 40.7 | 52.5 | 93.3 | 141.5 | 181.9 |
| | 13.2 | 8.9 | 4.9 | 2.6 | 1.8 | 2.4 | 4.3 | 6.4 | 8.5 |
| 4.64 | 345.4 | 216.0 | 109.9 | 55.7 | 39.6 | 52.4 | 90.8 | 138.2 | 166.4 |
| | 14.3 | 9.4 | 4.9 | 2.5 | 1.9 | 2.4 | 4.2 | 6.4 | 8.0 |
| 4.67 | 344.7 | 218.7 | 115.9 | 58.0 | 42.6 | 57.1 | 95.2 | 146.1 | 183.5 |
| | 14.2 | 9.4 | 5.1 | 2.7 | 2.0 | 2.6 | 4.3 | 6.7 | 8.7 |
| 4.72 | 376.9 | 218.1 | 113.7 | 55.3 | 42.9 | 59.9 | 92.2 | 145.4 | 182.1 |
| | 15.6 | 9.6 | 5.1 | 2.6 | 2.1 | 2.9 | 4.4 | 6.9 | 8.8 |
| 4.77 | 357.0 | 203.6 | 104.4 | 51.5 | 44.6 | 57.8 | 99.9 | 153.5 | 202.8 |
| | 14.9 | 8.8 | 4.8 | 2.4 | 2.1 | 2.8 | 4.8 | 7.2 | 9.7 |
| 4.82 | 371.3 | 209.3 | 99.4 | 50.6 | 41.5 | 55.1 | 91.8 | 149.8 | 206.2 |
| | 15.5 | 9.1 | 4.6 | 2.4 | 2.0 | 2.7 | 4.4 | 7.1 | 9.9 |
| 4.87 | 379.0 | 200.0 | 84.9 | 48.1 | 45.7 | 53.3 | 81.1 | 135.4 | 188.5 |
| | 16.0 | 8.6 | 4.0 | 2.3 | 2.3 | 2.7 | 3.9 | 6.5 | 9.0 |
| 4.93 | 361.8 | 196.8 | 83.9 | 47.9 | 50.4 | 56.3 | 76.5 | 117.1 | 168.6 |
| | 15.2 | 8.6 | 3.9 | 2.3 | 2.4 | 2.7 | 3.8 | 5.7 | 8.2 |

## 11B + N
## CROSS SECTIONS AND ERRORS, C.M. (MB/SR)

| ENERGY LAB (MEV) | ANGLE, C.M. (DEG) | | | | | | | | |
|---|---|---|---|---|---|---|---|---|---|
| | 21.8 | 40.7 | 59.3 | 77.5 | 95.2 | 112.5 | 129.3 | 145.7 | 161.8 |
| 4.98 | 364.5 | 182.5 | 76.4 | 51.5 | 56.1 | 62.9 | 81.3 | 122.5 | 173.9 |
| | 15.4 | 7.9 | 3.5 | 2.4 | 2.5 | 2.9 | 3.8 | 5.8 | 8.4 |
| 5.03 | 352.6 | 180.7 | 73.4 | 53.0 | 59.4 | 63.3 | 80.2 | 123.5 | 174.6 |
| | 14.9 | 7.8 | 3.3 | 2.5 | 2.7 | 3.0 | 3.7 | 5.9 | 8.5 |
| 5.08 | 354.0 | 186.0 | 72.4 | 52.3 | 63.2 | 69.6 | 81.7 | 130.1 | 183.7 |
| | 14.8 | 8.0 | 3.3 | 2.4 | 2.8 | 3.2 | 3.8 | 6.1 | 8.8 |
| 5.13 | 383.5 | 180.9 | 70.7 | 51.2 | 62.3 | 64.6 | 74.9 | 120.8 | 172.1 |
| | 16.4 | 8.0 | 3.3 | 2.4 | 2.8 | 3.1 | 3.7 | 5.8 | 8.4 |
| 5.18 | 398.0 | 182.9 | 68.4 | 51.8 | 63.4 | 63.1 | 75.0 | 118.9 | 175.5 |
| | 17.0 | 8.1 | 3.1 | 2.4 | 2.9 | 3.0 | 3.7 | 5.8 | 8.5 |
| 5.23 | 411.8 | 190.6 | 66.8 | 54.7 | 64.5 | 60.9 | 71.6 | 120.4 | 190.5 |
| | 17.4 | 8.5 | 3.1 | 2.5 | 3.0 | 2.9 | 3.6 | 6.0 | 9.3 |
| 5.28 | 421.8 | 184.7 | 64.9 | 55.2 | 73.4 | 70.7 | 77.2 | 128.8 | 200.2 |
| | 17.7 | 8.3 | 3.1 | 2.5 | 3.3 | 3.4 | 3.8 | 6.4 | 9.7 |
| 5.34 | 445.7 | 194.2 | 59.4 | 55.0 | 88.5 | 88.1 | 86.1 | 127.3 | 193.5 |
| | 18.6 | 8.7 | 2.9 | 2.5 | 3.9 | 4.1 | 4.3 | 6.2 | 9.4 |
| 5.39 | 417.3 | 177.5 | 53.2 | 51.1 | 93.4 | 99.6 | 87.6 | 106.8 | 141.0 |
| | 17.4 | 8.0 | 2.6 | 2.4 | 4.1 | 4.7 | 4.2 | 5.2 | 7.1 |
| 5.44 | 344.9 | 162.6 | 51.1 | 46.8 | 83.0 | 92.5 | 78.1 | 80.5 | 97.0 |
| | 14.6 | 7.1 | 2.5 | 2.1 | 3.6 | 4.3 | 3.7 | 4.0 | 5.1 |
| 5.49 | 287.9 | 140.1 | 54.3 | 42.0 | 64.7 | 79.5 | 76.5 | 72.1 | 75.1 |
| | 12.4 | 6.0 | 2.5 | 1.9 | 2.9 | 3.8 | 3.6 | 3.6 | 3.9 |
| 5.54 | 256.0 | 139.3 | 60.6 | 37.0 | 52.4 | 70.2 | 84.1 | 106.5 | 118.1 |
| | 11.0 | 6.2 | 2.7 | 1.7 | 2.4 | 3.2 | 4.0 | 5.1 | 5.9 |
| 5.59 | 320.4 | 157.2 | 62.0 | 41.5 | 61.5 | 78.6 | 93.2 | 136.4 | 178.2 |
| | 13.8 | 7.0 | 2.9 | 1.9 | 2.7 | 3.7 | 4.6 | 6.6 | 8.7 |
| 5.64 | 367.2 | 169.8 | 53.8 | 44.4 | 77.2 | 92.3 | 101.4 | 139.0 | 184.6 |
| | 15.6 | 7.5 | 2.5 | 2.1 | 3.3 | 4.3 | 4.9 | 6.7 | 9.0 |
| 5.69 | 370.3 | 177.6 | 56.8 | 46.9 | 77.2 | 95.1 | 100.3 | 127.5 | 161.4 |
| | 15.6 | 7.9 | 2.7 | 2.1 | 3.4 | 4.4 | 4.8 | 6.1 | 8.1 |
| 5.74 | 353.3 | 178.3 | 58.0 | 49.3 | 78.3 | 91.5 | 90.1 | 108.6 | 130.9 |
| | 14.7 | 8.0 | 2.7 | 2.3 | 3.5 | 4.2 | 4.4 | 5.3 | 6.7 |

## 11B + N
## CROSS SECTIONS AND ERRORS, C.M. (MB/SR)

| ENERGY LAB (MEV) | ANGLE, C.M. (DEG) | | | | | | | | |
|---|---|---|---|---|---|---|---|---|---|
| | 21.8 | 40.7 | 59.3 | 77.5 | 95.2 | 112.5 | 129.3 | 145.7 | 161.8 |
| 5.79 | 370.7 | 183.0 | 60.0 | 47.9 | 79.2 | 94.0 | 89.6 | 96.9 | 116.8 |
| | 15.5 | 8.1 | 2.8 | 2.2 | 3.5 | 4.3 | 4.4 | 4.9 | 6.1 |
| 5.85 | 387.0 | 194.4 | 61.8 | 45.8 | 75.6 | 94.2 | 93.6 | 93.7 | 103.2 |
| | 16.4 | 8.5 | 2.9 | 2.2 | 3.4 | 4.3 | 4.4 | 4.7 | 5.4 |
| 5.90 | 385.7 | 193.9 | 62.9 | 38.6 | 72.0 | 91.1 | 95.1 | 92.3 | 99.0 |
| | 16.5 | 8.4 | 3.0 | 1.9 | 3.2 | 4.2 | 4.5 | 4.7 | 5.2 |
| 5.95 | 369.7 | 184.6 | 61.5 | 36.2 | 65.6 | 85.2 | 90.4 | 92.5 | 103.1 |
| | 15.8 | 8.1 | 2.9 | 1.7 | 2.9 | 4.0 | 4.4 | 4.6 | 5.3 |
| 6.00 | 361.1 | 183.7 | 59.4 | 36.3 | 63.9 | 82.2 | 84.2 | 90.5 | 105.3 |
| | 15.4 | 8.1 | 2.8 | 1.7 | 2.9 | 3.8 | 4.1 | 4.5 | 5.5 |
| 6.05 | 333.6 | 169.7 | 57.6 | 34.4 | 63.6 | 83.4 | 79.2 | 91.7 | 104.9 |
| | 14.4 | 7.5 | 2.7 | 1.6 | 2.8 | 3.8 | 3.8 | 4.5 | 5.4 |
| 6.10 | 338.6 | 167.9 | 53.7 | 34.1 | 63.7 | 77.7 | 79.8 | 92.5 | 110.3 |
| | 14.7 | 7.3 | 2.5 | 1.6 | 2.8 | 3.6 | 3.8 | 4.5 | 5.6 |
| 6.15 | 367.4 | 174.4 | 57.8 | 36.2 | 65.3 | 79.1 | 82.6 | 90.0 | 106.5 |
| | 16.0 | 7.6 | 2.7 | 1.7 | 2.9 | 3.7 | 3.9 | 4.5 | 5.5 |
| 6.20 | 437.8 | 216.2 | 71.8 | 34.8 | 64.6 | 80.6 | 79.9 | 80.0 | 95.5 |
| | 18.9 | 9.6 | 3.4 | 1.7 | 3.0 | 3.7 | 3.9 | 4.2 | 4.9 |
| 6.25 | 460.0 | 230.6 | 76.6 | 34.0 | 54.9 | 77.7 | 77.0 | 76.8 | 83.9 |
| | 19.7 | 10.3 | 3.6 | 1.7 | 2.5 | 3.6 | 3.8 | 3.9 | 4.5 |
| 6.30 | 430.7 | 223.5 | 67.0 | 33.0 | 50.1 | 73.2 | 73.2 | 75.1 | 80.4 |
| | 18.4 | 10.0 | 3.2 | 1.7 | 2.4 | 3.5 | 3.6 | 3.7 | 4.2 |
| 6.36 | 436.8 | 213.9 | 65.1 | 29.0 | 48.9 | 68.9 | 67.3 | 72.4 | 78.5 |
| | 18.6 | 9.6 | 3.2 | 1.5 | 2.3 | 3.2 | 3.3 | 3.7 | 4.2 |
| 6.41 | 407.6 | 207.2 | 64.6 | 26.8 | 45.4 | 65.0 | 66.4 | 71.4 | 79.2 |
| | 17.6 | 9.3 | 3.1 | 1.3 | 2.2 | 3.1 | 3.2 | 3.6 | 4.2 |
| 6.46 | 412.2 | 190.3 | 61.2 | 30.2 | 44.3 | 63.7 | 66.0 | 73.5 | 77.2 |
| | 17.8 | 8.6 | 2.9 | 1.6 | 2.1 | 3.0 | 3.2 | 3.6 | 4.1 |
| 6.51 | 376.2 | 192.1 | 62.3 | 27.4 | 46.7 | 67.3 | 66.7 | 69.8 | 83.7 |
| | 16.2 | 8.5 | 2.9 | 1.3 | 2.0 | 2.9 | 3.0 | 3.4 | 4.2 |
| 6.58 | 379.6 | 186.6 | 58.4 | 25.7 | 46.3 | 63.2 | 63.4 | 70.6 | 83.8 |
| | 16.2 | 8.2 | 2.8 | 1.3 | 2.1 | 2.8 | 2.9 | 3.5 | 4.2 |

## 11B + N
## CROSS SECTIONS AND ERRORS, C.M. (MB/SR)

| ENERGY LAB (MEV) | ANGLE, C.M. (DEG) | | | | | | | | |
|---|---|---|---|---|---|---|---|---|---|
| | 21.8 | 40.7 | 59.3 | 77.5 | 95.2 | 112.5 | 129.3 | 145.7 | 161.8 |
| 6.66 | 398.8 | 186.6 | 54.9 | 22.4 | 46.8 | 60.7 | 60.2 | 69.5 | 83.8 |
| | 17.0 | 8.2 | 2.6 | 1.1 | 2.0 | 2.7 | 2.7 | 3.3 | 4.1 |
| 6.74 | 378.5 | 182.1 | 50.3 | 23.7 | 46.3 | 59.9 | 65.9 | 69.8 | 88.7 |
| | 16.2 | 8.0 | 2.4 | 1.1 | 2.1 | 2.7 | 3.0 | 3.3 | 4.3 |
| 6.81 | 394.5 | 183.1 | 47.9 | 25.0 | 43.1 | 52.7 | 55.4 | 71.1 | 90.0 |
| | 16.8 | 8.1 | 2.3 | 1.2 | 1.9 | 2.4 | 2.5 | 3.4 | 4.4 |
| 6.89 | 392.2 | 179.4 | 46.8 | 23.6 | 43.6 | 52.2 | 55.9 | 76.0 | 107.9 |
| | 16.9 | 7.9 | 2.2 | 1.1 | 1.9 | 2.4 | 2.5 | 3.5 | 5.2 |
| 6.94 | 404.5 | 187.1 | 45.9 | 21.7 | 45.3 | 52.9 | 54.4 | 79.3 | 117.7 |
| | 17.4 | 8.2 | 2.3 | 1.0 | 2.0 | 2.4 | 2.5 | 3.8 | 5.7 |
| 7.03 | 415.1 | 195.8 | 46.7 | 21.9 | 45.4 | 54.7 | 52.5 | 77.6 | 116.5 |
| | 17.8 | 8.6 | 2.2 | 1.1 | 2.0 | 2.4 | 2.4 | 3.7 | 5.6 |
| 7.10 | 404.2 | 198.3 | 47.9 | 21.2 | 44.3 | 51.4 | 46.5 | 70.9 | 103.8 |
| | 17.7 | 8.7 | 2.3 | 1.1 | 1.9 | 2.4 | 2.2 | 3.4 | 5.1 |
| 7.18 | 411.2 | 188.1 | 49.4 | 21.4 | 40.8 | 51.4 | 45.4 | 55.8 | 78.6 |
| | 18.0 | 8.5 | 2.5 | 1.2 | 1.9 | 2.4 | 2.2 | 2.8 | 3.9 |
| 7.29 | 396.3 | 185.4 | 50.1 | 22.7 | 41.1 | 53.1 | 46.4 | 45.7 | 62.0 |
| | 17.2 | 8.2 | 2.4 | 1.1 | 1.8 | 2.3 | 2.2 | 2.3 | 3.1 |
| 7.40 | 395.1 | 190.3 | 56.2 | 25.4 | 46.0 | 52.7 | 46.9 | 46.7 | 65.2 |
| | 17.1 | 8.4 | 2.7 | 1.3 | 2.1 | 2.3 | 2.1 | 2.2 | 3.3 |
| 7.52 | 411.3 | 190.3 | 51.6 | 30.2 | 50.6 | 53.4 | 39.8 | 44.5 | 58.8 |
| | 18.1 | 8.7 | 2.6 | 1.6 | 2.4 | 2.5 | 2.1 | 2.4 | 3.1 |
| 7.73 | 372.0 | 171.6 | 43.2 | 24.8 | 46.6 | 52.9 | 38.2 | 43.8 | 72.1 |
| | 16.4 | 7.6 | 2.1 | 1.3 | 2.2 | 2.4 | 1.8 | 2.3 | 3.6 |
| 8.03 | 421.8 | 195.6 | 42.7 | 19.5 | 48.0 | 52.8 | 35.4 | 25.9 | 34.3 |
| | 18.7 | 8.7 | 2.2 | 1.1 | 2.1 | 2.4 | 1.8 | 1.5 | 1.8 |

# APPENDIX 8

# LEGENDRE EXPANSION COEFFICIENTS

3

11B + N
LEGENDRE COEFFICIENTS AND ERRORS, C.M.
(MB/SR)

| ENERGY LAB (MEV) | B0 | B1 | B2 | B3 | B4 |
|---|---|---|---|---|---|
| 4.00 | 109.36 | 83.56 | 132.81 | 35.45 | -3.03 |
| | 1.85 | 4.17 | 4.94 | 4.96 | 4.98 |
| 4.08 | 95.20 | 58.02 | 114.15 | 31.42 | 6.11 |
| | 1.56 | 3.51 | 4.26 | 4.32 | 4.52 |
| 4.10 | 95.67 | 58.91 | 117.48 | 31.27 | 3.93 |
| | 1.54 | 3.47 | 4.17 | 4.17 | 4.47 |
| 4.21 | 97.19 | 47.50 | 125.00 | 24.67 | 1.51 |
| | 1.55 | 3.53 | 4.26 | 4.21 | 4.53 |
| 4.31 | 98.30 | 35.55 | 131.49 | 25.55 | 8.59 |
| | 1.54 | 3.53 | 4.29 | 4.14 | 4.64 |
| 4.41 | 100.26 | 34.62 | 136.98 | 22.47 | 8.14 |
| | 1.57 | 3.59 | 4.35 | 4.17 | 4.69 |
| 4.52 | 105.36 | 34.12 | 143.14 | 29.64 | 9.83 |
| | 1.64 | 3.75 | 4.56 | 4.40 | 4.95 |
| 4.57 | 110.89 | 46.30 | 154.30 | 24.58 | 16.79 |
| | 1.76 | 4.05 | 4.99 | 4.81 | 5.30 |
| 4.62 | 113.44 | 60.39 | 158.54 | 22.47 | 19.73 |
| | 1.81 | 4.16 | 5.11 | 4.90 | 5.27 |
| 4.64 | 114.47 | 71.00 | 162.83 | 32.16 | 19.18 |
| | 1.87 | 4.35 | 5.31 | 5.02 | 5.34 |
| 4.67 | 119.13 | 67.20 | 166.60 | 29.33 | 19.84 |
| | 1.91 | 4.40 | 5.41 | 5.20 | 5.55 |
| 4.72 | 120.68 | 73.38 | 175.31 | 41.50 | 27.40 |
| | 1.99 | 4.64 | 5.72 | 5.44 | 5.78 |
| 4.77 | 118.30 | 57.35 | 175.68 | 35.50 | 34.21 |
| | 1.93 | 4.50 | 5.59 | 5.24 | 5.83 |
| 4.82 | 117.39 | 62.87 | 182.97 | 38.44 | 41.75 |
| | 1.95 | 4.58 | 5.75 | 5.29 | 5.71 |
| 4.87 | 111.68 | 66.34 | 176.59 | 51.25 | 57.41 |
| | 1.88 | 4.42 | 5.62 | 5.21 | 5.54 |
| 4.93 | 108.31 | 69.72 | 162.03 | 58.55 | 55.85 |
| | 1.82 | 4.24 | 5.36 | 5.05 | 5.37 |
| 4.98 | 109.27 | 60.26 | 156.67 | 60.79 | 62.83 |
| | 1.79 | 4.14 | 5.34 | 5.09 | 5.34 |

### 11B + N
### LEGENDRE COEFFICIENTS AND ERRORS, C.M.
### (MB/SR)

| ENERGY LAB (MEV) | B0 | B1 | B2 | B3 | B4 |
|---|---|---|---|---|---|
| 5.03 | 108.70 | 57.02 | 152.78 | 59.81 | 66.82 |
| | 1.77 | 4.06 | 5.28 | 5.07 | 5.30 |
| 5.08 | 111.93 | 55.43 | 157.21 | 64.98 | 71.56 |
| | 1.80 | 4.11 | 5.32 | 5.12 | 5.39 |
| 5.13 | 109.98 | 64.16 | 159.41 | 70.94 | 78.04 |
| | 1.84 | 4.25 | 5.51 | 5.27 | 5.45 |
| 5.18 | 110.88 | 66.49 | 163.65 | 74.01 | 84.36 |
| | 1.87 | 4.32 | 5.63 | 5.32 | 5.48 |
| 5.23 | 113.42 | 69.60 | 172.91 | 73.65 | 96.81 |
| | 1.93 | 4.45 | 5.87 | 5.45 | 5.62 |
| 5.28 | 118.01 | 64.45 | 174.08 | 81.56 | 104.06 |
| | 1.98 | 4.51 | 5.95 | 5.64 | 5.83 |
| 5.34 | 125.56 | 68.37 | 176.17 | 110.11 | 113.95 |
| | 2.09 | 4.69 | 6.13 | 5.96 | 6.09 |
| 5.39 | 118.29 | 66.48 | 146.04 | 126.43 | 96.76 |
| | 1.98 | 4.31 | 5.51 | 5.66 | 5.58 |
| 5.44 | 102.53 | 63.00 | 113.78 | 115.35 | 71.78 |
| | 1.71 | 3.68 | 4.62 | 4.89 | 4.77 |
| 5.49 | 88.78 | 52.32 | 92.02 | 90.64 | 40.65 |
| | 1.47 | 3.19 | 3.90 | 4.23 | 4.20 |
| 5.54 | 89.12 | 33.99 | 107.67 | 61.59 | 27.90 |
| | 1.43 | 3.23 | 3.94 | 4.02 | 4.40 |
| 5.59 | 105.76 | 34.21 | 144.77 | 68.67 | 56.90 |
| | 1.72 | 3.93 | 4.97 | 4.85 | 5.30 |
| 5.64 | 115.77 | 39.90 | 156.18 | 96.34 | 79.15 |
| | 1.88 | 4.24 | 5.40 | 5.32 | 5.57 |
| 5.69 | 115.69 | 48.44 | 148.82 | 103.27 | 73.26 |
| | 1.89 | 4.24 | 5.33 | 5.35 | 5.56 |
| 5.74 | 110.47 | 56.53 | 132.54 | 104.18 | 68.74 |
| | 1.82 | 4.02 | 5.04 | 5.15 | 5.25 |
| 5.79 | 111.17 | 65.95 | 132.75 | 114.99 | 67.36 |
| | 1.85 | 4.10 | 5.08 | 5.24 | 5.27 |
| 5.85 | 112.33 | 73.49 | 136.73 | 123.88 | 60.57 |
| | 1.89 | 4.25 | 5.20 | 5.37 | 5.26 |

11B + N
LEGENDRE COEFFICIENTS AND ERRORS, C.M.
(MB/SR)

| ENERGY LAB (MEV) | B0 | B1 | B2 | B3 | B4 |
|---|---|---|---|---|---|
| 5.90 | 110.25 | 74.58 | 140.76 | 126.12 | 53.27 |
| | 1.88 | 4.25 | 5.10 | 5.27 | 5.24 |
| 5.95 | 105.42 | 69.90 | 138.85 | 115.69 | 50.46 |
| | 1.80 | 4.10 | 4.91 | 5.00 | 5.05 |
| 6.00 | 103.04 | 69.63 | 137.93 | 111.41 | 54.01 |
| | 1.76 | 4.02 | 4.87 | 4.92 | 4.94 |
| 6.05 | 98.66 | 61.66 | 129.44 | 104.34 | 50.93 |
| | 1.67 | 3.77 | 4.58 | 4.67 | 4.71 |
| 6.10 | 97.95 | 60.59 | 132.25 | 103.34 | 56.45 |
| | 1.65 | 3.77 | 4.61 | 4.65 | 4.68 |
| 6.15 | 101.82 | 68.42 | 136.89 | 110.09 | 57.74 |
| | 1.74 | 3.98 | 4.86 | 4.91 | 4.90 |
| 6.20 | 111.91 | 101.43 | 164.13 | 134.49 | 62.21 |
| | 2.01 | 4.66 | 5.56 | 5.52 | 5.31 |
| 6.25 | 112.18 | 112.68 | 170.54 | 135.58 | 54.03 |
| | 2.05 | 4.85 | 5.75 | 5.53 | 5.14 |
| 6.30 | 105.19 | 103.84 | 160.48 | 126.95 | 52.04 |
| | 1.94 | 4.58 | 5.46 | 5.28 | 4.81 |
| 6.36 | 102.30 | 105.36 | 162.46 | 128.20 | 55.74 |
| | 1.90 | 4.52 | 5.36 | 5.12 | 4.70 |
| 6.41 | 98.03 | 99.25 | 156.91 | 119.51 | 49.95 |
| | 1.83 | 4.33 | 5.10 | 4.84 | 4.54 |
| 6.46 | 95.26 | 92.37 | 147.45 | 111.47 | 47.97 |
| | 1.77 | 4.22 | 5.08 | 4.86 | 4.44 |
| 6.51 | 94.78 | 89.01 | 146.38 | 112.17 | 48.56 |
| | 1.68 | 3.99 | 4.76 | 4.50 | 4.25 |
| 6.58 | 92.67 | 88.00 | 147.09 | 111.74 | 52.58 |
| | 1.66 | 3.93 | 4.70 | 4.48 | 4.24 |
| 6.66 | 92.51 | 92.45 | 154.61 | 119.24 | 60.21 |
| | 1.67 | 3.96 | 4.72 | 4.43 | 4.13 |
| 6.74 | 90.49 | 83.26 | 147.24 | 112.50 | 57.64 |
| | 1.62 | 3.85 | 4.61 | 4.35 | 4.18 |
| 6.81 | 88.49 | 86.95 | 150.84 | 107.23 | 65.51 |
| | 1.62 | 3.87 | 4.73 | 4.36 | 4.00 |

11B + N

LEGENDRE COEFFICIENTS AND ERRORS, C.M.

(MB/SR)

| ENERGY LAB (MEV) | B0 | B1 | B2 | B3 | B4 |
|---|---|---|---|---|---|
| 6.89 | 89.47 | 83.14 | 157.79 | 104.75 | 71.92 |
| | 1.62 | 3.84 | 4.77 | 4.31 | 4.10 |
| 6.94 | 92.25 | 87.31 | 169.42 | 111.43 | 80.90 |
| | 1.68 | 3.97 | 4.93 | 4.41 | 4.27 |
| 7.03 | 94.06 | 93.02 | 173.99 | 116.69 | 84.01 |
| | 1.71 | 4.04 | 5.06 | 4.53 | 4.25 |
| 7.10 | 91.33 | 97.69 | 170.09 | 116.58 | 82.17 |
| | 1.70 | 4.02 | 4.99 | 4.48 | 4.09 |
| 7.18 | 87.15 | 101.19 | 156.47 | 117.70 | 70.11 |
| | 1.69 | 4.01 | 4.88 | 4.50 | 3.94 |
| 7.29 | 84.71 | 101.51 | 144.17 | 118.31 | 62.22 |
| | 1.61 | 3.83 | 4.58 | 4.26 | 3.67 |
| 7.40 | 87.88 | 104.87 | 145.96 | 118.18 | 64.33 |
| | 1.66 | 3.89 | 4.72 | 4.44 | 3.84 |
| 7.52 | 88.02 | 107.65 | 141.77 | 120.93 | 74.01 |
| | 1.73 | 4.07 | 4.99 | 4.80 | 3.98 |
| 7.73 | 81.75 | 94.85 | 137.76 | 113.79 | 76.77 |
| | 1.56 | 3.60 | 4.49 | 4.30 | 3.67 |
| 8.03 | 83.44 | 118.90 | 145.74 | 143.62 | 76.95 |
| | 1.68 | 3.90 | 4.64 | 4.50 | 3.38 |